High-Speed Imaging of Unstable and Stable Homogeneous Nucleation of Diethyl Ether Droplets at the Superheat Limit

F. Robert Ferris III

A thesis

submitted in partial fulfillment of the

requirements for the degree of

Master of Science in Mechanical Engineering

University of Washington

2019

Committee:

Jim Hermanson

Alberto Aliseda

John Kramlich

Program Authorized to Offer Degree:

Mechanical Engineering

University of Washington

Abstract

High-Speed Imaging of Unstable and Stable Homogeneous Nucleation of Diethyl Ether Droplets at the Superheat Limit

F. Robert Ferris III

Chair of Supervisory Committee:

Dr. Jim Hermanson

Aeronautics and Astronautics

Immersed diethyl ether droplets, sized 0.5 to 3.5 mm in diameter, undergoing homogeneous boiling at the limit of superheat, 147˚C, are examined experimentally. The boiling process and resulting vapor bubble behavior filmed at 100,000 frames per second is studied in conjunction with far-field pressure data. It is shown that at low pressures, 1 – 2 bar absolute, homogeneous nucleation manifests as unstable explosive boiling, where the evaporating bubble interface becomes unstable in a process believed to be similar to Darrieus-Landau instabilities, leading to an evaporative velocity and mass flux an order of magnitude greater than traditional boiling. In comparison, at elevated pressures, 3 – 5 bar absolute, homogeneous nucleation is stable, resulting in a smooth evaporative interface devoid of instabilities and a vaporization velocity and mass flux rate comparable to traditional nucleate boiling. Vapor bubble growth during unstable nucleation is found to be linear with constant interface velocity and mass flux rate. In addition, vapor bubble growth during stable nucleation vaporization shows a roughly

logarithmic shape with time, with an interface velocity and mass flux that decays rapidly at first and slowing overtime. The normalized droplet diameter combined with the resulting vapor bubble diameter is examined from the beginning of nucleation until the vapor bubble stops expanding. For unstable nucleation, the normalized diameter growth generally forms an S-shaped curve. For stable nucleation, the normalized diameter growth appears mostly linear. Increasing ambient pressure is shown to decrease growth rate, interface velocity, and mass flux rate. Increasing initial droplet diameter is shown to not have an impact on vapor bubble growth rate, interface velocity, or mass flux rate. However, when normalized by initial droplet diameter, smaller initial diameter droplets are found to grow to larger vapor bubble diameters than larger initial diameter droplets. After unstable explosive boiling is complete, the behavior of the resulting vapor bubble is studied as oscillations occur, a result of initial growth kinetic energy, and Rayleigh-Taylor interface instabilities form. Rayleigh-Taylor instabilities on the surface of the vapor bubble are quantified in a wavelength parameter, which is shown to first decrease in length with subsequent oscillations before increasing in length as oscillations are dampened by presumably some combination of thermal, viscous, and acoustic radiation effects. Pressure data is shown during vaporization and during subsequent vapor bubble oscillation. An increased ambient pressure is found to correlate to a decreased Rayleigh-Taylor instability wavelength, a decreased overpressure amplitude, and an increased oscillation frequency. An increase in initial droplet diameter has been shown to increase Rayleigh-Taylor instability wavelength, increase overpressure amplitude, and decrease vapor bubble oscillation frequency.

To my parents,

without your support none of this would have been possible

Acknowledgments

There are many people who provided assistance and support during this project. Chief among them, my principal investigator Professor Jim Hermanson who gave continuous advice, support, and motivation throughout this work. I benefited substantially from his experience in designing, building, and running an experiment from start to finish, as well as from his knowledge on planning and writing a thesis. I would also like to thank our collaborators at Southern Illinois University, Carbondale, Professor Asghar Esmaeeli and Mr. Arash Asaollahi for many teleconference meetings, advice, and presenting our results at DFD APS 2018. I would also like to give a special thanks to Mr. Zach Rotter, my undergraduate assistant, who provided a critical third (and fourth) hand when running the experiment to ensure no data was left uncollected, as well as for providing a second set of eyes to ensure my safety. I would also like to thank Professor Carl Knowlen for the equipment – especially the pressure transducer, DAQ, and light cannon – as well as for the unique experimental insight. Additionally I would like to thank Professor Knowlen's research assistant, Mr. James Koch for his assistance getting the DAQ up, running, and collecting data. I would also like to thank Mr. Eliot George, the Aeronautics & Astronautics' lead development engineer for his assistance in design questions and getting the PID temperature controller running. I would like to thank both Mr. Bob Scott, the physics department machinist, and Mr. Dzung Tran, the Aeronautics & Astronautics machinist, for doing the technical machining involved in this project, as well as odds and ends oftentimes on the house. I would also like to give a special thanks to Professor David Frost at McGill University for providing unique mentorship throughout this project. Additionally, I would like to thank Mr. Rohtash Mann and Ms. Thao Nguyen, two earlier undergraduate assistants for their help in designing and building this experiment. I would also like to thank the Mrs. Wanwisa Kisalang, the Mechanical Engineering Department's graduate academic adviser for answering all my administrative questions. Last but not least, I would like to thank my parents and grandmother for providing assistance and support throughout the course of this project. I could not have done it without you. Thank you all.

Table of Contents

List of Figures

List of Tables

List of Symbols

Symbol	Description
A_S	Surface Area
c	Speed of sound
C_p	Specific heat of gas at constant pressure
D	Diameter
D_o	Initial droplet diameter
D_g	Thermal diffusivity in gas
Ja	Jakob Number
K	Thermal conductivity in gas
L	Latent heat of vaporization
L_g	Thermal diffusion length in vapor
P_0	Ambient pressure
q	Mass flux rate
Q	Mass flow rate
R_e	Bubble equilibrium radius
t	Time
Δt	Change in time, time step
T	Temperature
v	Velocity
v_l	Kinematic viscosity of the host fluid
v_b	Total bubble interface velocity
$\overline{v}_b$	Bubble interface velocity
v_d	Total droplet interface velocity
v_e	Total evaporation velocity
$\overline{v}_e$	Averaged evaporation velocity
$\cancel{V}$	Volume

x	Position
α	Constant, defined as, R_e/L_g
δ	Total damping constant
δ_r	Acoustic radiation damping constant
δ_T	Thermal damping constant
δ_V	Viscous damping constant
ρ	Density
γ	Ratio of specific heats of vapor
ω	Bubble oscillation frequency
ω_r	Bubble resonance frequency
$()_A$	Method A
$()_B$	Method B
$()_i$	At i
$()_{i+1}$	At $i+1$
$\overline{()}_{i\to i+1}$	Average of value at i and at $i+1$
$()_l$	liquid
$()_{sat}$	Saturation temperature, boiling point
$()_{SL}$	Limit of superheat
$()_v$	vapor

1.0 Introduction

When boiling, also called vaporization, occurs the incipient vapor bubble starts growth at a nucleation site. The location of this nucleation site determines the type of boiling that is initiated. There are two main types of boiling, heterogeneous and homogeneous. In heterogeneous boiling, the more common of the two, boiling occurs at a nucleation site on a surface. A common example of this is water boiling in a pot, where the water boils into steam at nucleation points where the water contacts the surface of the heated pot. In homogeneous boiling a surface is not needed for nucleation, with a nucleation point for the incipient vapor bubble occurring in the bulk fluid away from the surface. Typically homogeneous boiling is rarely seen as conditions, such as fluid temperature, that would allow heterogeneous boiling to occur would result in a near-zero probability for homogeneous boiling to occur [1].

Superheating is a phenomenon where a liquid can be heated to past the liquid's boiling point without undergoing phase change. The liquid enters a metastate where boiling becomes probabilistic, that can be induced at any time by as little as a small disturbance [2]. As a result, to obtain high degrees of superheat, certain conditions must be maintained. The fluid to be superheated must be homogenous and devoid of imperfections, especially trapped gas bubbles. The fluid must also be contained in a way that minimizes nucleation sites, such as in a smooth, clean glass beaker or immersed in an immiscible fluid. Both of these conditions minimize heterogeneous nucleation points, with the goal of eliminating them. By eliminating heterogeneous nucleation sites, heterogeneous nucleation is repressed, allowing conditions favorable for homogeneous nucleation to develop. Additionally, the fluid must be heated to superheat slowly enough to ensure that the fluid is at uniform temperature. If a fluid is heated too rapidly, the outer edges of the fluid will heat faster than the bulk fluid, increasing the probability of heterogeneous nucleation and decreasing the probability of homogeneous nucleation. Lastly, the fluid must be quiescent. A metastate liquid can be brought to a phase change with a small disturbance. A superheated liquid can be brought to a boil with a stir or a shake. Following these conditions, high degrees of superheat can be achieved at temperatures high above the boiling point of the liquid. Under precise conditions, the maximum achievable temperature in the fluid can be reached, called the limit of superheat, or superheat limit, which is the limit of mechanical stability in the liquid [3]. When the limit of superheat is attained, homogeneous boiling in the fluid occurs spontaneously. If at atmospheric pressure, or near-atmospheric pressure, the fluid boils violently, reaching an evaporative velocity and mass flux rate an order of magnitude greater than standard boiling. At these pressures, the vaporization bubble interface becomes unstable to perturbations, causing a two-phase mass transfer, driving the evaporative velocity and mass flux to these high rates [2, 4, 5]. At elevated pressures, this instability is repressed, leading to stable homogeneous nucleation at evaporative velocity and mass flux rates comparable to ordinary boiling.

When a liquid is superheated, and unstable vaporization occurs, it does so violently, releasing large amounts of energy rapidly. This is termed explosive boiling, but also known by

various other names such as vapor explosion, steam explosion, boiler explosion, rapid phase transitions, cold explosion, physical explosion, fuel-coolant interaction (FCI), and Boiling Liquid Expanding Vapor Explosion. This phenomenon can occur accidentally if a volatile liquid is brought into contact with a hot stable liquid or a hot smooth surface, or if a volatile liquid under high pressure is depressurized rapidly. On a macroscale, this can and has proved dangerous and destructive. Explosive boiling can also occur in nuclear power plant failure, with an FCI explosion hypothesized the cause of much of the physical damage at Chernobyl [6]. In the interaction of magma with water, for example in July, 2018, molten rock falling into the ocean in Hawaii caused a steam explosion that inured over 20 on a nearby tour boat [7]. Rapid phase transition explosions can occur when liquefied natural gas (LNG), kept at temperatures of approximately -162˚C, escapes its pressure vessel and mixes with water, commonly 15 ˚C [8]. Dangerous explosive boiling on the macroscale can occur in a wide range of fields and workplaces. Better understanding explosive boiling can lead to better safety parameters in industries with high likelihood of explosive boiling occurring to minimize the risk of destruction or injury. Additionally, explosive boiling applications have become increasingly investigated on the microscale. Micro explosive boiling can be utilized for small scale actuation, such as in thermal inkjet printers [9, 10]. Additionally, microscale explosive boiling have been demonstrated to be used as microactuators for micro fluidic devices [11]. Better understanding explosive boiling can also lead to future developments on Micro-Electro-Mechanical Systems (MEMS).

A comprehensive theory of quantifying explosive boiling does not currently exist nor is there a definitive model that characterized explosive boiling completely. The classical theory was put forth by Blander & Katz and by Prosperetti & Plesset [12, 13]. Another model is the molecular cluster model by Kwak & Lee where the classical model was modified to include the surface energy needed for bubble formation which is calculated from the interaction energy of molecules [14, 15]. An additional model is the Thornton Research Centre (TRC) model, developed by Nguyen *et al.*, which based the evaporative mass flux on the vapor bubble interface velocity relative to the surrounding fluid, the inverse of previous modeling work [16]. Numerous experimental studies have been carried out in the past, building upon earlier studies to optimize the superheating experiment. The earliest studies that used high-speed photography such as Dergarabedian in 1960, Kosky in 1968, and Abdelmessih, Hooper, & Nangia in 1972 all had early success quantifying vapor bubble growth rates, finding that their results roughly corroborated the budding classical bubble theories put forth by their theory contemporaries [17, 18, 19]. Abdelmessih *et al.* impressively filmed bubble vaporization at 7,000 frames per second, though it is unclear how many frames they were able to capture at this rate or the trigger delay encountered. Shepherd & Sturtevant in 1982 were the first to observe the unstable vaporization interface, hypothesizing that it was caused by a process similar to the Darrieus-Landau instability [3, 20]. By this point the droplet column, or bubble column, experimental apparatus concept for repeatedly superheating droplets was fully formed. Frost examined the role of pressure on unstable boiling as well as further examined the unstable interface, which, was known by this point to be suppressed at elevated pressures, a claim further supported by his work [4, 21]. Later,

McCann *et al.* in 1988 captured explosive vaporization at 500,000 frames per second, but were limited to only 5 frames per trial [22]. However, they were able to qualify the classical model and TRC model with their experimental data and found rough verification, with the two models reflecting similar growth velocity curve shapes, but also growth velocities roughly twice of what they found, shown in Appx. 6. One consistent trend in past research involving high-speed imaging is the need to trigger the camera to start recording with a pressure transducer, as a result there is a consistent trigger delay in past research so the incipient vapor bubble is not imaged. Steps were taken to account for this delay, the most common being moving the pressure transducer extremely close to the explosive boiling site, sometimes as close as 2 mm. It is unclear if this affected the bubble vaporization dynamics at all, but this allowed a trigger delay of only 5 µs to 15 µs. Park, Kwak *et al.* in 1995 and in 2005 expanded on previous research by forming their own model and studying homogeneous test fluid mixtures, measuring the limit of superheat and vaporization behavior of these mixtures, and finding good agreement with the classical theory model and the molecular cluster model, assuming all fluid conditions are known [15, 23].

By the time the research reported here was conducted, droplet explosive boiling experiments had already been conducted for over half a century. Thanks to previous researchers, the rough design and features of the droplet column had already been through many iterations and many potential design pitfalls could be avoided to build a repeatable droplet superheating apparatus. Where the present work expands on this research is the use of state-of-the-art technology. Technology moves forward rapidly, and high-speed camera technology is not independent of that. The chief goal of the research presented here is to film homogeneous vaporization, both unstable and stable, in full, from before incipient nucleation to after oscillations are damped and buoyancy takes effect, in sufficient spatial and temporal resolution to allow analysis of the phenomenon in detail. The experimental set up and instrumentation used to capture unstable and stable homogeneous nucleation is reviewed in Chapter 2, including a general briefing of the droplet column and associated instrumentation, a fluid description of both the test and host fluids and why they were selected, the high-speed imaging hardware, and a detailed experimental procedure with related pitfalls and advice to ensure future repeatability and safety.

In chapter 3 the results are presented and discussed, including measurement methodologies, fundamental phenomenon, and high-speed imaging stills – unfortunately high-speed videos cannot be presented on printed paper. However, a video repository has been set up to allow viewing of a select number of videos as detailed in Appx. 7. Additionally, the role of ambient pressure and initial droplet diameter are examined in relation to diameter and volumetric growth rate, vapor bubble interface and evaporation velocities, vapor bubble mass flux and mass flow rates, unstable boiling vapor bubble Rayleigh-Taylor wavelengths and oscillation frequency, and pressure data as it pertains to oscillation frequency and overpressure amplitude. It is found that vapor bubble growth during unstable nucleation is linear with constant interface velocity and mass flux rate. It is also found that vapor bubble growth during stable nucleation vaporization appears roughly logarithmic with an interface velocity and mass flux that

exponentially decays. For unstable nucleation, the normalized diameter growth forms an S-shaped curve. For stable nucleation, the normalized diameter growth appears mostly linear. Increasing ambient pressure is shown to decrease growth rate, interface velocity, and mass flux rate. Increasing initial droplet diameter is shown to not have an impact on vapor bubble growth rate, interface velocity, or mass flux rate. However, it is found that when normalized by initial droplet diameter, smaller initial diameter droplets grow to larger vapor bubble diameters than larger initial diameter droplets. It is found that an increased ambient pressure correlates to a decreased Rayleigh-Taylor instability wavelength, a decreased overpressure amplitude, and an increased oscillation frequency. An increase in initial droplet diameter has been shown to increase Rayleigh-Taylor instability wavelength, increase overpressure amplitude, and decrease vapor bubble oscillation frequency.

The references section follows the conclusion. The Appendix follows the references where stable-to-unstable boiling is touched on briefly, with associated images and normalized diameter, interface velocity, and Rayleigh-Taylor wavelength figures. Additionally the Appendix contains some miscellaneous figures and extended versions of figures presented earlier, including a list form of the experimental procedure, touched on earlier.

2.0 Experimental Setup and Instrumentation

Measurement of explosive boiling requires bringing a droplet to its superheat limit, which in turn requires finely tuned instrumentation and custom experimental design. To successfully record high-speed video of an explosively boiling droplet, the experimental setup and instrumentation must be finely tuned to allow the droplet to be brought to its limit of superheat. Premature heterogeneous nucleation can occur in the immersed droplet at the interface between the test liquid droplet and the ambient host liquid if experimental testing conditions are not precise. Proper temperature gradients in the experimental apparatus, quiescent host liquid, precise pressure in the experimental apparatus, careful selection of test and host fluids, and accurate droplet injection sizes are all necessary to ensure explosive homogenous nucleation in the droplet within the narrow field of view and depth of field of a high-speed camera. The following sections are a description of the experimental setup and instrumentation used to ensure this explosive boiling experiment is repeatable and reproducible.

2.1 Droplet Column Apparatus

The droplet column is the centerpiece of the experimental setup. The droplet column is a modified version of the bubble column used by Frost [4] which is a modified version of the bubble column used by Shepherd & Sturtevant [3]. The fundamentals of the droplet column and bubble columns are the same, and the differences in their names is simply preferred nomenclature by this author. The redesigned droplet column departs from Frost's bubble column in several ways, the most relevant of which is relocating the high pressure nitrogen inlet port to provide improved safety.

The droplet column, shown in Fig. 2.1 and Fig. 2.2, consists of a columnar pressure vessel filled with a host liquid. Precise dimensions are provided in Fig. 2.2. At the base of this column, a droplet of test liquid is injected into the host liquid. This test liquid, immiscible and buoyant in the host liquid, slowly rises up though the host liquid in the droplet column. The droplet column is heated from the top and cooled from the bottom, establishing a linear temperature gradient throughout the height of the droplet column and host liquid. A cubic test section sits at the top of the droplet column with viewports on three faces for imaging and back lighting. The temperature inside this test section is monitored and sustained at the superheat limit of the test liquid. As the test liquid droplet rises, it is heated gradually by the temperature gradient of the host liquid the droplet is immersed in. Once the droplet reaches the test section and is within the field of view of the viewports, the temperature inside the droplet is very near the superheat limit of the test liquid and homogenous nucleation occurs, rapidly vaporizes the droplet in entirety. The homogenous nucleation, colloquially referred to as explosive boiling in this document, is captured and examined with high-speed video and fast-response pressure equipment.

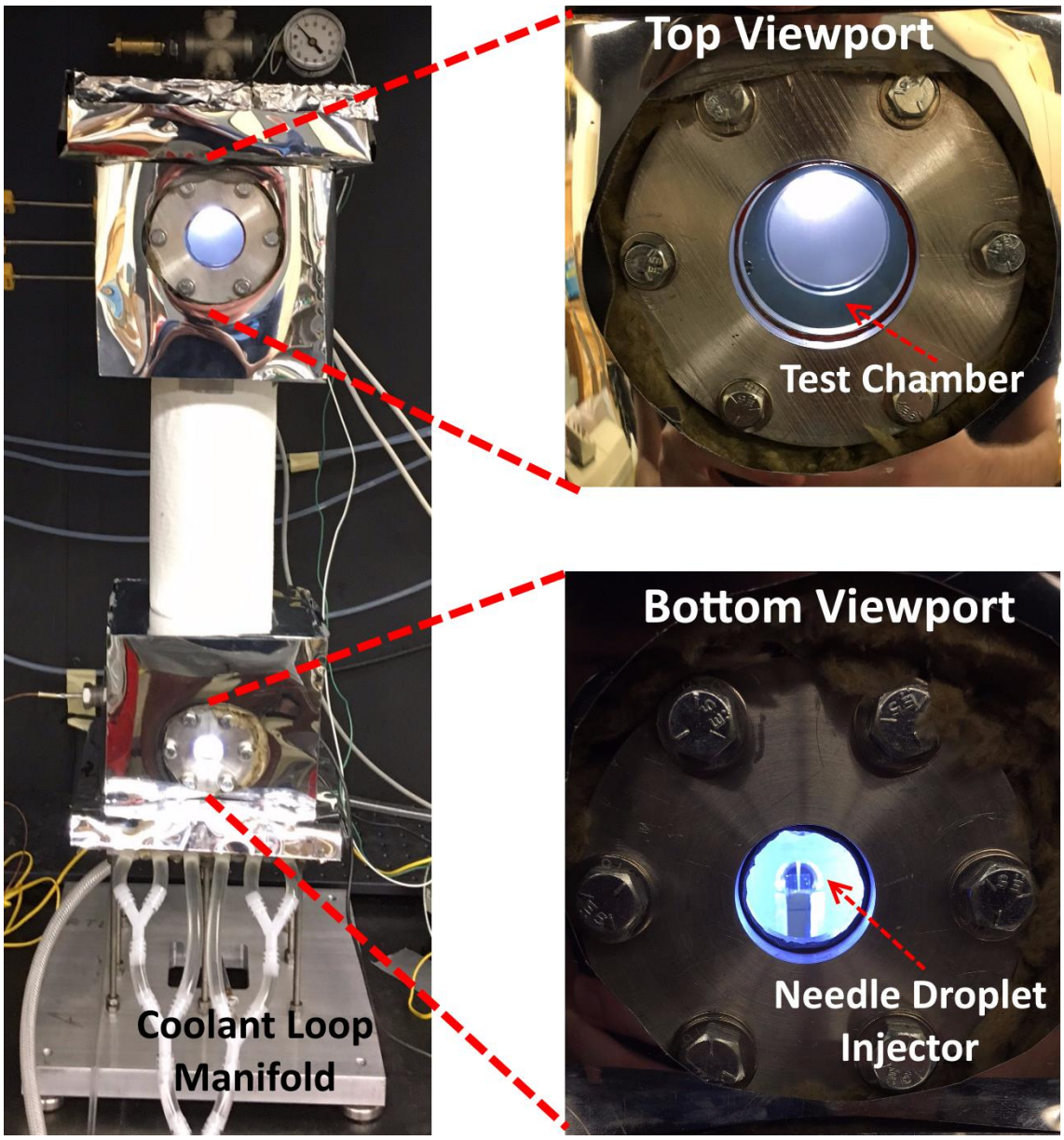

Fig. 2.1 – Droplet column with enlarged views of the top viewport showing the test chamber and backlighting and the bottom viewport showing the needle droplet injector. Coolant loop also visible. Aluminum droplet column is wrapped in insulation and Mylar.

The droplet column is made from aluminum 6061. This material was chosen because of its good machinability and weldability, relatively low cost and ease of attainability, while maintaining good mechanical properties, including a high thermal conductivity for rapid droplet column heat up. The flat sections of the droplet column were constructed from ½" thick aluminum plate while the middle cylindrical section from a single piece of aluminum tubing 2.375" in diameter with a wall thickness of 0.5". All segments except the top and bottom plate were then welded together. The upper test section is 5" x 5" x 5.5" (width x depth x height), providing sufficient space for a droplet to homogenously nucleate. The rise distance from droplet

injection point to the center of the test chamber is 17.25”, which corresponds to an average rise time of 30 seconds for sized 1-2 mm diameter droplets. This is sufficient time to provide gradual heating in the droplet to induce superheating resulting in explosive vaporization. A CNC mill was utilized to make the four viewport screw patterns and O-ring grooves to ensure proper alignment when installed in the droplet column. Traditional machining methods, such as drilling and tapping, were used to construct the screw holes on the welded flanges and top and bottom plates, O-ring grooves on the top and bottom of the droplet column, top plate piping port, bottom plate cooling ducts, droplet injector LED ports, HP nitrogen gas inlet port, drainage port, four thermocouple ports, and pressure transducer port. Top plate piping and all other piping coupled to various ports were made from a mixture of store bought brass and stainless steel piping, depending on what was most economical. All pressurized threads were sealed with high temperature pipe thread sealant tape and max pressure rating for all piping is 125 psi minimum at 200˚C. Installed in the top plate piping is an exhaust port, a pressure gauge rated to 100 psi, and an emergency pressure-relief valve set to 90 psi. The top and bottom plate were secured to the welded column with stainless steel screws. An O-ring groove, cut in the top and bottom flange of the welded section, was filled with a Viton O-ring. Viton was selected here due to a high operating temperature of 315˚C and high chemical resistance. Viton was purchased as cord, cut to length, the ends where scarred, and the cord was spliced together with Viton adhesive.

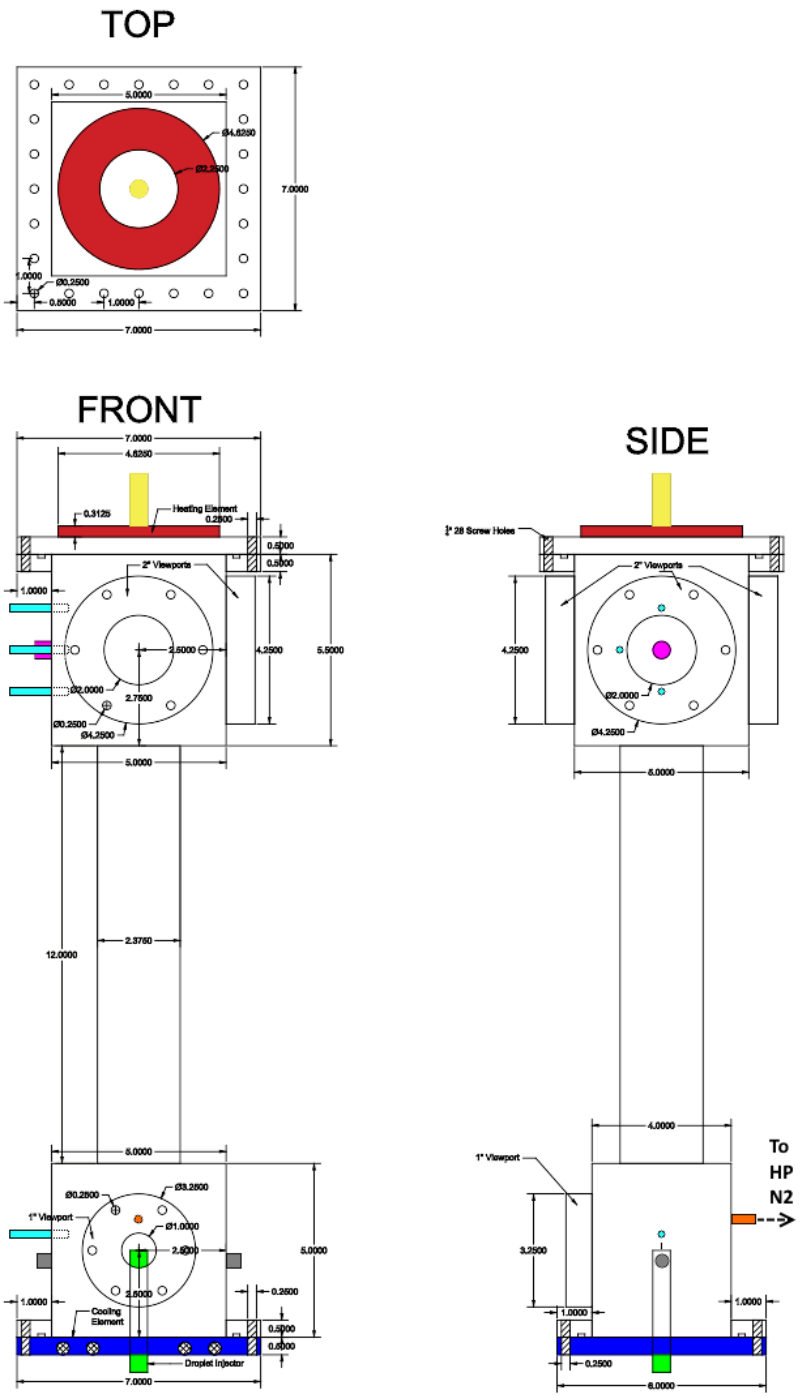

Fig. 2.2 – Technical drawing of the droplet column showing top, front, and side views. Yellow shows the location of the top plate piping with exhaust port, pressure gauge, and emergency pressure-relief valve attached but not displayed on this diagram. Red shows the location of the ring heating element. Turquoise shows the location of the thermocouples. Magenta shows the location of the pressure transducer. Orange shows the location of the high pressure nitrogen gas inlet. Green shows the location of the droplet injector. Blue shows the location of the cooling plate. Grey shows the location of the droplet injector LEDs. All measurements are in inches.

There are four viewports on the droplet column for observation during the experiment. Three are on the top test section to allow examination of explosive boiling events and one is at the base of the column next to the droplet injector to monitor precise injection of test liquid droplets. The viewports on the test section are arranged so that the front viewport is for viewing the explosive boiling event, the back viewport is for backlighting the explosive boiling for the high-speed camera, and the side viewport is to give flexibility if filming with two synched camera is desired or if filming with side lighting is desired. The viewing window of the viewports mounted on the test section are 2" in diameter whereas the viewing window of the viewport at the base is 1" in diameter. The viewport flanges are made from aluminum 6061 and manufactured using CNC milling to ensure a precise fit. Fused quartz glass is utilized for the viewport windows. The top viewports utilize 1/3" thick quartz glass, whereas the bottom viewport uses ¼" thick quartz glass. Quartz was selected here for a number of reasons. First, quartz has good mechanical properties for a glass, allowing higher testing pressures. Second, quartz has excellent thermal properties with a large maximum operating temperature of over 1000˚C, as well as a low coefficient of thermal expansion of 10^{-6}/˚C, giving it a high resilience to thermal shock. Third, quartz is extremely chemical resistant. Lastly, quartz has great optical transmission properties allowing for excellent viewing of the explosive boiling phenomenon. The viewport flanges sandwiched the quartz glass to the droplet column with the assistance of six equally space stainless steel screws. A Viton O-ring is nestled between the quartz glass and the droplet column in an O-ring groove to form a seal and to prevent the quartz glass from making contact with the aluminum to prevent shattering. Additionally, a Viton gasket sits between the quartz glass and the aluminum flange to prevent contact. The top viewports have the lowest pressure rating due to their size. Their maximum operating pressure when the droplet column is fully heated is 100 psi with a factor of safety of 2.5. For the purposes of this research, testing pressures do not exceed 75 psi, however, a 90 psi emergency pressure-relief valve is installed for added safety.

Deviating somewhat from Frost's bubble column, the high pressure nitrogen inlet port used to pressurize the droplet column for elevated pressure testing is located at the bottom of the column as opposed to the top. This is attached via high pressure tubing to a regulator on a nitrogen compressed gas cylinder rated at 2,000 psi. The reasons for placing the nitrogen inlet at the base are twofold. First, and most important, is operator safety. When the droplet column is heated, the top plate with heater reaches temperatures exceeding 200˚C. This temperature exceeds both the flash point of the test fluid, diethyl ether, but also the autoignition temperature at 160˚C. Additionally, there is a small volume of gas of 33.74 cm^3 above the host liquid column inside the top plate piping. Upon homogenous nucleation, the diethyl ether gas mixes with the preexisting gas in the top plate piping at raised temperature. The flammability limit of diethyl ether is 1.9-48.0% [24]. Taking an average diameter of injected droplet to be 1.5 mm, the flammability limit is reached in just 2 droplets. If the preexisting gas in the top plate piping is air, a safety conflict arises due to the presence of oxygen. By moving the high pressure nitrogen gas inlet to the base of the droplet column, the top plate piping can be purged of all air prior to testing by bubbling up nitrogen gas though the host liquid. By the top piping being devoid of oxygen, the

flammability limit can be safely surpassed, which is important because testing only 2 droplets per testing cycle is too slow to be a viable testing schedule. In practice closer to 100 droplets were injected without issue before shutting the experiment down and venting. This roughly equates to 0.5 mL, or one syringe full. The top exhaust port is left open during the purging process to allow the preexisting gas to escape, then closed upon completion. The droplet column is located under a lab exhaust hood that is kept on during and after testing to remove all harmful gases. The second reason the nitrogen inlet is located at the bottom is to clear obstacles suspended in the host fluid from the droplet pathway. After a break in testing, the droplet injector must be cleaned and flushed out. Water is used for this, and having a lower density than the host liquid, glycerol, it floats to the surface where it boils off during the heating process prior to testing and is vented. Nitrogen gas bubbling up through the host liquid ensures all the water and any possible impurities are pushed up and out of the droplet's path, as well as purging the top plate piping of any water vapor or air it may contain. A drainage port is also located just above the nitrogen inlet, facilitating draining the droplet column of host liquid if cleaning, repairs, or modifications are necessary.

A fast-response piezoelectric pressure transducer is used to collect the pressure trace from the homogenous nucleation and the subsequent bubble oscillations. The PCB Model 112A21 piezoelectric pressure transducer is flush-mounted on the left wall of the top test section 50% of the way up the wall and in the center plane, making it directly in line with the target explosion location for droplets. This is done to ensure that the plane of the pressure transducer diaphragm is perpendicular to the vector of the vaporizing droplet pressure waves in order to maximize the registered pressure trace, minimizing noise. The 112A21 has a measurement range of 100 psi, a sensitivity of 50 mV/psi (±10 mV/psi), a resolution of 0.002 psi, a rise time of ≤2.0 μs, and a low frequency response (-5%) of 0.5 Hz. The pressure transducer is connected to a high-speed data acquisition unit via a signal amplifier and BNC cable. The data acquisition unit is controlled from a laptop computer using LabVIEW. The sampling rate is set to 1.25 MHz and the sampling duration set to 3 seconds. A common rise time to first peak is on the order of 600 μs. A sample rate of 1.25 MHz gives 750 data points in this time span for good temporal resolution. The face of the flush mounted pressure transducer is located 50.8 mm from the target explosion location. The speed of sound for the host liquid, glycerol, at 147˚C is 2227.4 m/s. At this speed, the pressure wave takes 22.8 μs to reach the pressure transducer. The pressure trace captured by the flush mounted pressure transducer captures the far-field pressure of the exploding droplet and subsequent oscillations by the resulting test vapor bubble. This creates a roughly sinusoidal pressure trace that dampens out with time after between 8 and 20 oscillations depending on the initial droplet diameter and ambient pressure.

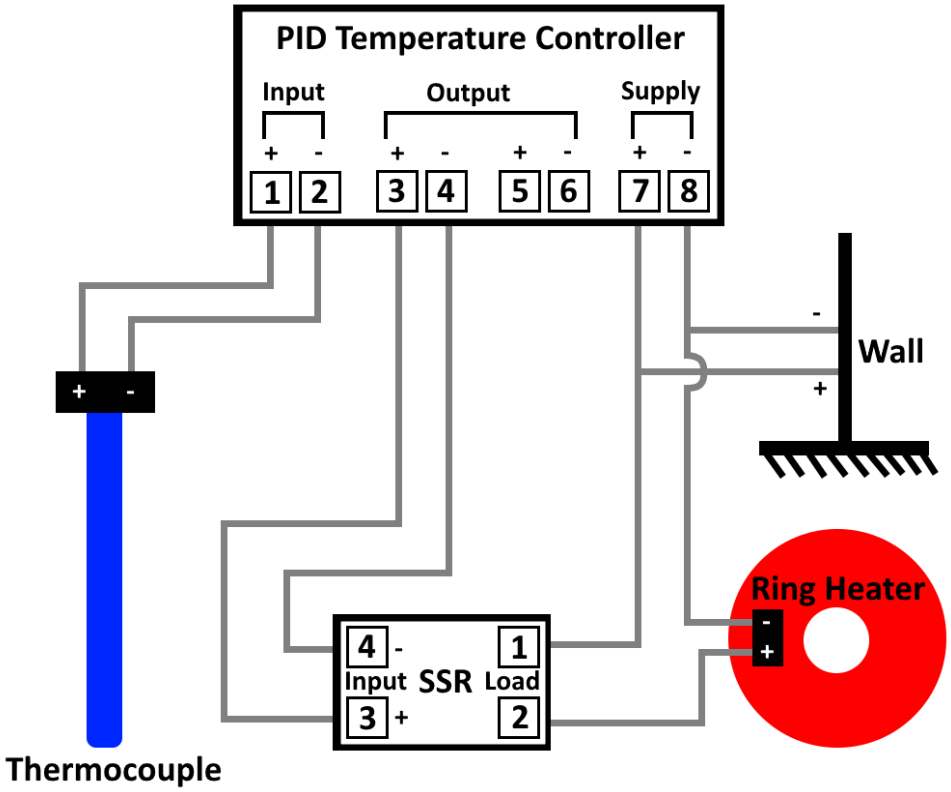

Fig. 2.3 – PID temperature controller wiring schematic showing input top thermocouple, the ring heating element, and the solid state relay (SSR).

The droplet column contains four Type K thermocouples to ensure a linear temperature gradient is established and to ensure the droplet reaches the test fluid's limit of superheat in the center of the test section. The majority of the droplet column is insulated with mineral wool and Mylar to make the column as close to adiabatic as possible on the sides, promoting a linear temperature gradient in the vertical direction and no temperature gradient in the horizontal direction. One thermocouple is located at the base of the droplet column 1" from the droplet injector tip giving an accurate temperature at which the droplet is formed. For most testing this is 22˚C. Three thermocouples are located in the top test section in the left wall. Two are located along the midline of the wall, 25% and 75% of the way up the wall, and the third is located just off the midline 50% of the way up the wall. This third transducer is offset by 1" due to the presence of the wall mounted pressure transducer. There is less than a 1˚C temperature offset due to the horizontal shift of this center thermocouple as the viewport are not covered in insulation, causing a slight horizontal temperature gradient in the test chamber. This offset is taken into account when calculating all vertical temperature gradients. All four thermocouples are mounted through the wall utilizing Swagelok tube fittings. The three thermocouples in the test section are mounted so as to penetrate 1.5" into the bulk host liquid to avoid being influenced by the droplet column wall temperature. From these three upper thermocouples, a

local temperature gradient inside the test section host liquid can be found. Utilizing the lower thermocouple in conjunction with these, an average temperature gradient can be found throughout the height of the column. The local vertical temperature gradient inside the test section when the center thermocouple reads 147˚C is 7.4˚C/inch and the average temperature gradient throughout the height of the column is 6.9˚C/inch. This lower temperature gradient for the overall height is expected due to the wall not being perfectly adiabatic.

The top thermocouple is utilized as the input for a Chromalox PID temperature controller which is connected to a Chromalox 550 W ring heating element on the top of the droplet column via a solid state relay (SSR). The wiring schematic is shown in Fig. 2.3. The middle thermocouple is located at the ideal height in the test section for explosive boiling to occur as this is in the center of the field of view of high-speed camera. However the top thermocouple is used instead of the middle thermocouple due to the faster response time it provides by being closer to the heating element. A layer of silver thermal paste is applied between the ring heating element and the top plate to enhance heat transfer into the droplet column. A layer of double-thick aluminum foil is secured above the heating element to minimize heat loss to the ambient room air. The ring heater is able to bring the host liquid at the center of the test chamber to the limit of superheat of the test liquid, 147˚C, in 1.5 hours. The temperature within the column typically cycles ±5˚C in 45 minute periods, creating a 5 minute testing window twice a cycle. Internal temperatures are also measured using the middle thermocouple attached to a thermocouple digital display to ensure the center of the test section is near the limit of superheat of the test fluid.

At the bottom of the rig, the base plate has six horizontal ducts bored through it to allow the passage of coolant, in this case, water. A Cole-Parmer chiller pump is attached to these ducts via a six-way manifold and PVC clear tubing, forming a cooling loop seen in Fig. 2.1. The chiller is set to 22˚C which efficiently keeps the bottom plate at this set temperature as well. If the chiller is not used, the droplet injector mounted in the base plate heats up and the test liquid heterogeneously boils when injected. The chiller helps to create a linear, stable vertical temperature gradient within the host liquid by providing a fixed temperature base.

The droplet injector is installed in the center of the baseplate protruding upwards into the bottom of the droplet column, shown in Fig. 2.1 and Fig., E.2. The injector consists of a 27 gauge stainless steel needle, with inner diameter of 0.21 mm, silver soldered into the center of a pipe plug which is connected to a 0.5 mL glass syringe. Prior to testing, the glass syringe is loaded with test fluid and droplets ranging from 1 to 2 mm in diameter are injected from this reservoir. A ¼” stainless steel sheath tube is mounted in a concentric manner around the needle, but ending at a slightly lower point to reveal the tip of the needle. The tube is open to host liquid and a reinforced high pressure PVC tube is attached to the base of the tube, filling with host fluid. If a droplet is injected and does not detach from the tip of the needle due to surface tension, squeezing this PVC tube thrusts a small jet of host fluid up through the sheath tube to detach the droplet. This was found to be unnecessary for droplets with diameters greater than 1 mm as they detach naturally under buoyancy. A small, mm-scale ruler is attached to the top of the sheath

tube so that a droplet can be injected at the proper size. Droplets are injected at room temperature of 22˚C. The baseplate the droplets are injected through is kept at room temperature using the cooling loop. Two through-wall flush mounted 5 W LEDs are mounted at the base of the droplet column, one on each side of the droplet injector, to illuminate the injection process.

2.2 Fluid Description

Two fluids are utilized in the droplet column, the host liquid and the test liquid. The test liquid makes up the droplet which is injected into the host medium. The host liquid fills the droplet column, providing a heat transfer medium to the droplet and providing a buoyant medium so the droplet will gradually rise. The fluids chosen are considered from previous droplet column research [4]. The following four criteria must be followed when selecting a test liquid and a host liquid to ensure explosive boiling. First, the host and test liquids must be immiscible. Second, the test liquid must have a lower density than the host liquid. Third, the host liquid must have a higher boiling point than the superheat limit of the test liquid. Fourth, the host liquid must have a surface tension large enough to ensure homogeneous, not heterogeneous, nucleation takes place with the test fluid droplet. Satisfying these criteria are diethyl ether for the test fluid and glycerol for the host fluid. Compared to other applicable test fluids, like butane or propane, diethyl ether exists as a liquid at room temperature and pressure, whereas butane and propane exist as gases at these conditions. This allows more straightforward implementation of diethyl ether than butane or propane. Relevant properties of the test and host fluid are displayed in Table. 2.1. These fluids are also readily available and economically priced. 5.5 L of glycerol are used to fill the droplet column. 500 mL of diethyl ether was purchased. Over the course of 9 months of testing, the glycerol inside the droplet column was exchanged three times. During this testing period approximately 250 mL of diethyl ether was consumed.

Test Liquid	Diethyl ether
Boiling point [˚C]	34.6
Superheat Limit [˚C]	147
Dynamic Viscosity [cP] @ 20˚C @100˚C	 0.23 0.12
Surface Tension [mN/m] @ boiling point	15.3
Specific Heat [J/g-K] @ boiling point	2.24
Density [g/cm^3], @ boiling point	0.709

Host Liquid	Glycerol
Boiling Point [˚C]	290
Dynamic Viscosity [cP], @ 20˚C @ 100˚C @ 150˚C	 1490 37 2.7
Surface Tension [mN/m] @ 20˚C @ 90˚C @ 150˚C	 63.4 58.6 51.9
Heat Capacity [J/mol-K] @ 25˚C	221.9
Density [g/cm^3], @ 20˚C	1.26

Table. 2.1 – Relevant chemical properties of the test fluid, diethyl ether, and the host fluid, glycerol. [13, 25, 26, 27]

2.3 High-Speed Imaging Hardware

A Phantom v1211 high-speed camera, shown in figure Fig. 2.4, mounted on a tripod is utilized to capture all high-speed video. A Nikon AF-S VR Micro-Nikkor 105mm f/2.8G IF-ED lens is used in conjunction with the high-speed camera to zoom in on the exploding droplet giving a field of view of 32 mm x 32 mm and a depth of focus of 15 mm. Homogenous nucleation time scales from previous research suggested a need to have a video frame rate in the 100,000 frames per second (fps) range. However, resolution decreases with increasing frame rate, creating an optimization problem between a fast enough frame rate to study the explosive boiling phenomenon with sufficient temporal resolution and high enough spatial resolution to study the physical phenomenon optically. The resolution changes discretely in large steps, whereas the frame rate changes on a much finer scale approaching a spectrum, therefore the resolution is the driving variable and the frame rate is maxed out for that resolution. Two resolution and frame rate pairs were tested: 256 x 256 pixels at 100,000 fps and 128 x 128 pixels at 240,000 fps. In preliminary experiments the 128 x 128 pixels had insufficient spatial resolution to properly examine the physical characteristics of homogenous nucleation, despite the temporal resolution being excellent. Therefore, the 256 x 256 pixel and 100,000 fps pair, with exposure time of 10 µs, is utilized for all video collection reported in this document, providing both adequate spatial and temporal resolution for analyzing the explosive boiling event.

Fig. 2.4 – Phantom v1211 high-speed camera mounted on tripod with droplet column test chamber visible in background. The macro lens is not mounted on the camera in this picture.

A high frame rate also decreases the exposure time, reducing the amount of light that can activate the camera sensor for each frame. A powerful backlight source improves image quality by increasing the amount of light available for each frame. A 165 W Intellytech Light Cannon is employed, providing sufficient, high-intensity illumination. The light is passed through a frosted white glass diffuser before passing through the back viewport. A top down view of this set up is shown in Fig. 2.5. The diffuser gives a uniform background to the camera image allowing better imaging of the droplet. Past research [3, 4, 21] suggest utilizing opal glass inside the test section to effectively turn the backlight into a Lambertian light source, a source that diffuses light equally in all angles. Opal glass was tested but, imaging was slightly worse than the frosted white glass due to the opal glass being more opaque. During the duration of testing, a single camera was used, imaging through the front viewport. The high-speed camera was controlled with a laptop running Phantom Camera PCC 3.1. Prior to every group of trials, a physical length scale of 2 mm is filmed inside the test chamber at the target nucleation point. This is uploaded into PCC during image processing to ensure an accurate length scale for all measurements during analysis. Typically this length scale is 0.125 mm/pixel, though can vary depending on how far the tripod and camera are set up from the droplet column.

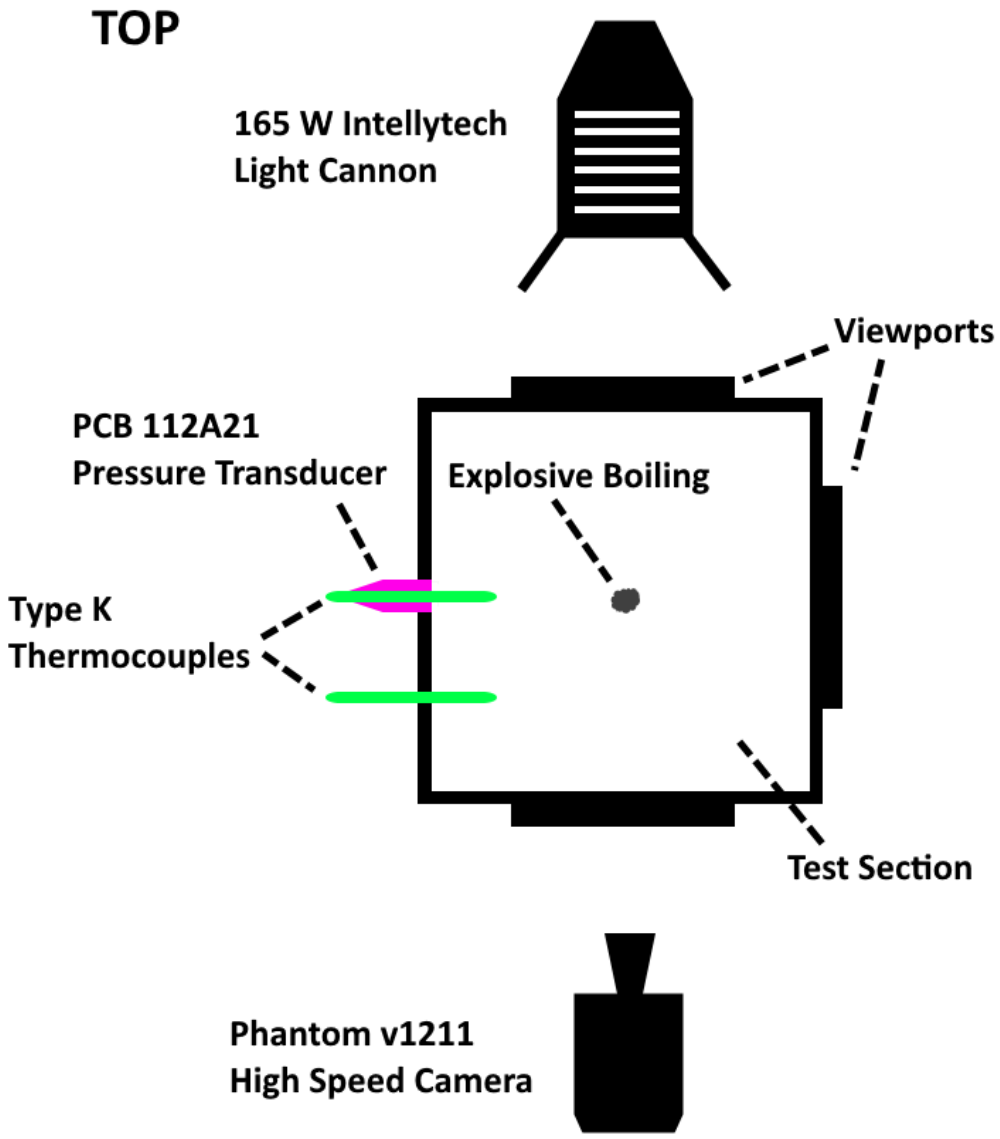

Fig. 2.5 – Top down view of the optical experimental set up showing the high-speed camera and light cannon in relation to the explosive boiling event within the test section. Thermocouples and pressure transducer also shown.

2.4 Experimental Procedure

The following is a concise experimental procedure followed for all explosive boiling experimental testing with relevant comments. An extended list form of this procedure can be found in Appx. 10.

The high-speed camera is first ensured to be in focus on the desired point in the test section for vaporization to occur. Next, length scale measurements are taken for use in image

processing later. The droplet injector is then flushed and loaded with the test fluid. Next, the droplet column is sealed and heated from the top, cooled from the bottom. Once nearly heated, the droplet column is then purged with nitrogen gas. The rig is then brought up to desired testing temperature and pressure. Test fluid droplets are injected via the droplet injector at the base of the droplet column. Once the droplets reach the test section, they vaporize, either stably or unstably, depending on the droplet column pressure. This boiling event is captured with both the high-speed camera and the pressure transducer for later image processing and data analysis. Upon completion of testing, the top heater is shut off and the droplet column is allowed to cool before it is vented.

3.0 Results and Discussion

3.1 Explosive Boiling Imaging

There are two boiling regimes which are dependent on the ambient pressure of the host fluid. However, the superheat limit temperature, or the temperature at which nucleation must occur in a superheated fluid, does not change based on the pressure range of this experiment, 1 to 5 bar absolute. The superheat limit for diethyl ether was measured to be approximately 147˚C for this range of pressure. This is consistent with previous research that examines the superheat limit change with varying ambient pressure [3, 4, 23].

The first boiling regime observed is explosive boiling, or unstable homogeneous nucleation. A diagram of unstable boiling is shown in Fig. 3.1 and a progression of the explosive boiling event is Fig. 3.4. The second of the boiling regimes observed is stable homogeneous nucleation. A diagram of stable boiling is shown in Fig. 3.2 and a progression of the stable boiling event is Fig. 3.7. The pressure at which the transition from the unstable regime to the stable regime occurs has not been closely examined in this experiment, but is found from observation to be around 3 bar absolute. Additionally, there is a third regime mostly found around 3 bar, but can occur less frequently as low as 2 bar and as high as 4 bar, where the nucleation starts out stable then a second unstable nucleation point occurs vaporizing the remainder of the liquid droplet explosively. This stable-to-unstable nucleation is examined in more detail in Appendix 5.1.

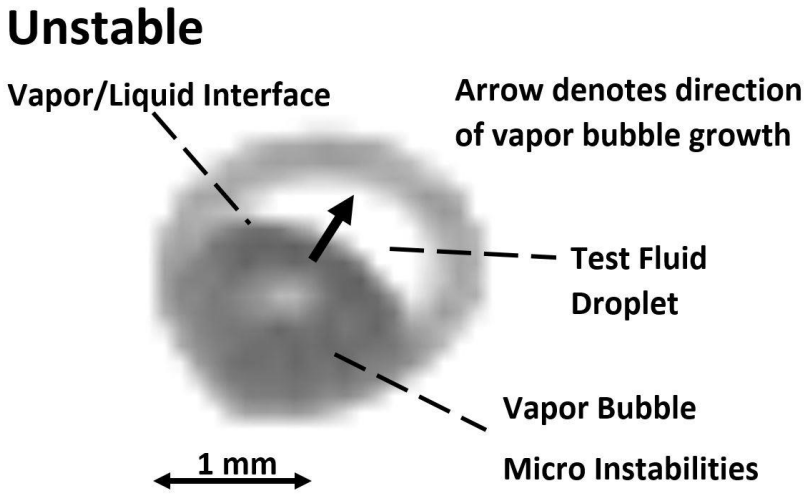

Fig. 3.1 – Unstable homogeneous boiling diagram.

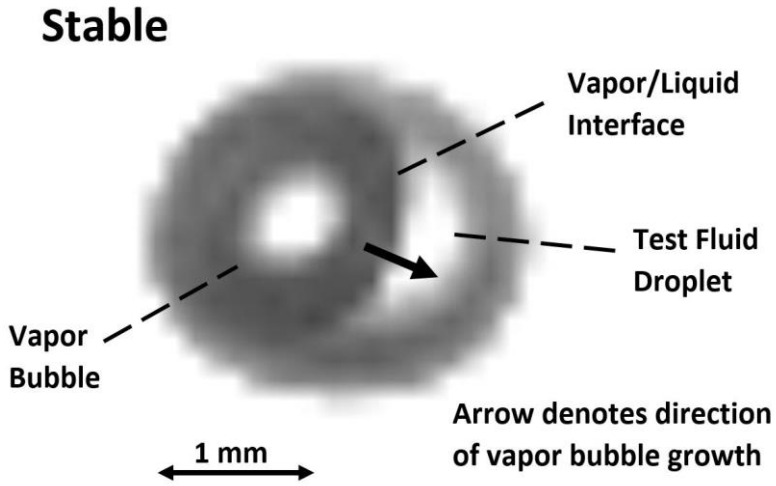

Fig. 3.2 – Stable homogeneous boiling diagram.

There are three main differences observed between unstable and stable boiling. The first is that unstable boiling occurs at a much more rapid mass flux rate than stable boiling. This can be observed in comparing the amount of time for the droplet to be completely consumed by the vapor bubble in Fig. 3.4 to Fig. 3.7. Taking the last image displayed as completely consumed, unstable boiling takes 180 μs in Fig. 3.4, whereas stable boiling takes 10 ms in Fig. 3.7. Stable boiling is over an order of magnitude slower than unstable boiling. While these droplets' initial diameters are not identical, the minor variation in initial droplet diameter does not impact this conclusion. Unstable boiling occurring at a much more rapid mass flux rate than stable boiling is further supported later on in this chapter when interface velocities, mass flux, and mass flow rates are examined.

The second difference is what causes this increase mass flux rate, the expanding vapor bubble surface roughness. As detailed by Shepherd & Sturtevant [4] and Frost [3], at lower ambient pressures the presence of a lower density vapor pushing against a higher density fluid at the vaporization interface create micro surface instabilities on the expanding vapor bubble. The process evidently is a Darrieus-Landau-like instability. The Darrieus-Landau instability is a naturally occurring flame instability that occurs when a premixed fuel is used. As fuel is burned and crosses the flame interface it heats up, leading to thermal expansion. This leads to the flame interface being unstable to perturbations of any size [3, 4, 5, 20]. A similar phenomenon occurs at the vapor/liquid interface of the expanding vapor bubble during explosive vaporization, shown in Fig. 3.3. As the interface propagates across the droplet during vaporization, high density liquid is being evaporated to lower density vapor. This causes an expansion on the trailing face of the interface which leads to the interface being unstable to perturbations, and these micro surface instabilities form. It is believed that these surface instabilities cause the boiling to become unstable resulting in a larger interface velocity and a larger mass flux vaporization rate [3, 4]. The presence of these micro surface instabilities suggest the presence of explosive boiling occurring and can be observed in Fig. 3.4 but is not apparent in Fig. 3.7. In Fig. 3.4 a liquid diethyl ether

droplet as a vapor bubble grows inside of it is shown, eventually consuming it in its entirety as a result of explosive boiling. The vapor bubble interface contain micro instabilities that refract the backlight passing though, leading to increased opacity, which is displayed in the images as darkness. However, in stable boiling, shown in Fig. 3.7, due to a higher ambient pressure the presence of surface instabilities is suppressed, resulting in a smooth vapor bubble surface, allowing backlight to pass through except where it is refracted at the spherical bubble edges. It is believed these micro surface instabilities are suppressed at higher pressures, first, because the expansion of the vapor on the trailing face of the interface is less at higher pressure, and second, because the higher ambient pressure acts as a damper to bubble surface perturbations [3, 4].

The third difference between unstable and stable boiling is the presence of vapor bubble oscillations after unstable boiling, but not after stable boiling. After the liquid droplet is consumed by the vapor bubble, the bubble interface is carried past the bubble's equilibrium point with the ambient host fluid's pressure presumably by momentum from the high interface velocity due to explosive boiling. The bubble over expands at which point its growth slows to a stop as the bubble's internal pressure decreases. The bubble then begins to contract, again moving past the equilibrium point, where it then slows to a stop as internal bubble pressure rises. The bubble then begins to expand again, starting a new oscillation cycle, shown in Fig. 3.5 and Fig. 3.6. Fig. 3.6 is purposely overexposed to better show the bubble interface instability detail. Over a number of oscillations the peak-to-peak amplitude of the bubble diameter slowly decreases as the bubble diameter regresses to the equilibrium point as energy is lost due to thermal, viscous, and acoustic radiation damping [3, 28]. Additionally, right after the bubble contracts for the first time and start to expand during the second oscillation cycle, there is a heavy onset of Rayleigh-Taylor instabilities as a result of a lower density fluid pushing a higher density fluid. The average wavelength, or mean diameter, of these instabilities as well as bubble oscillation metrics are discussed in detail later in this chapter. For stable boiling no oscillations occur as the bubble interface velocity is not large enough to allow the interface to expand past the equilibrium point. Additionally in the stable case, there is no onset of Rayleigh-Taylor instabilities as the interface velocity and accelerations are not rapid enough [3].

At an ambient pressure of approximately 2.5 to 3 bar, stable boiling is seen, resulting in markedly different behavior than for the case of unstable boiling just discussed. Around this transition pressure, a combination boiling regime appears, stable-to-unstable boiling. This consists of stable homogeneous nucleation point occurring, vaporizing part of the liquid droplet, and, after an indeterminate amount of time later, a new unstable boiling nucleation point occurring, rapidly vaporizing the remaining liquid droplet and resulting in typical post-unstable boiling vapor bubble oscillations. Stable-to-unstable boiling has been observed to occur at 2 bar, 3 bar, and 4 bar, with a highest occurrence rate at 3 bar. At 1 bar and at 5 bar it has not been observed to occur, with only unstable and stable boiling occurring at those pressures, respectively. Stable-to-unstable boiling is discussed in more detail in Appx. 6.1.

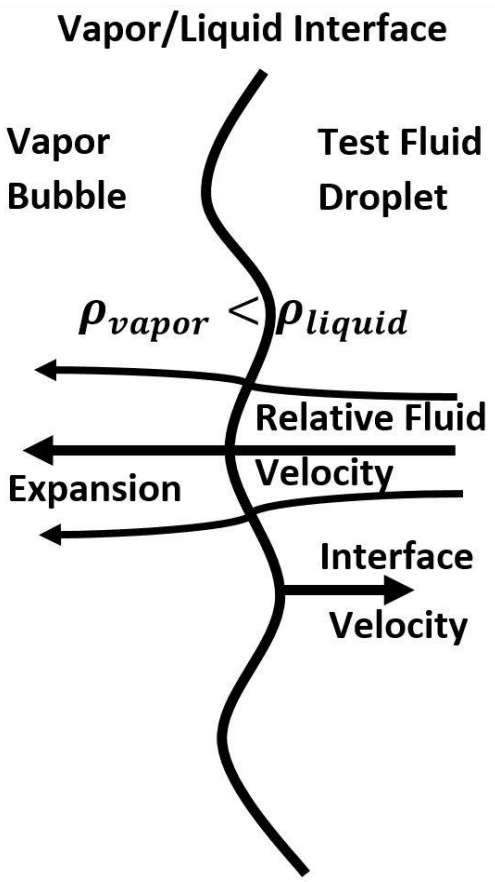

Fig. 3.3 – Darrieus-Landau-like micro instabilities diagram. As the vapor bubble grows the evaporative interface propagates across the liquid droplet. As the fluid vaporizes, its density drops moving across the interface causing the interface to be unstable any perturbations, creating micro surface instabilities and leading to an order of magnitude greater mass flux and evaporative interface velocity rate than stable boiling. [3, 4, 20]

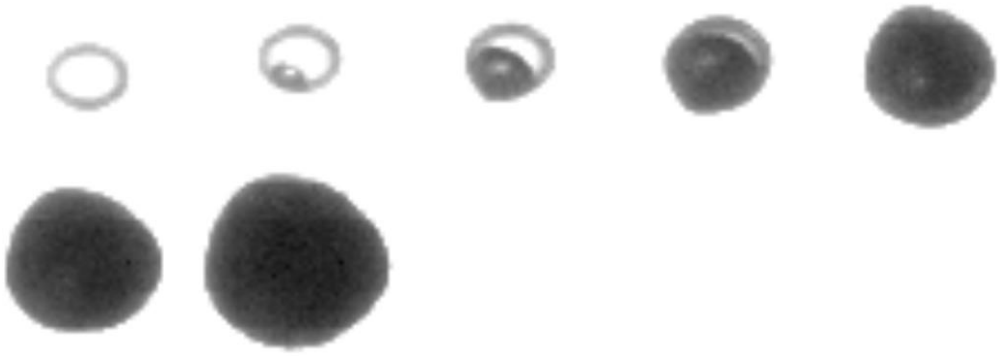

Fig. 3.4 – Unstable explosive boiling in a diethyl ether droplet of diameter, D_0 = 2.12 mm, immersed in glycerol at 1 bar pressure. Time between each image, Δt = 30 µs.

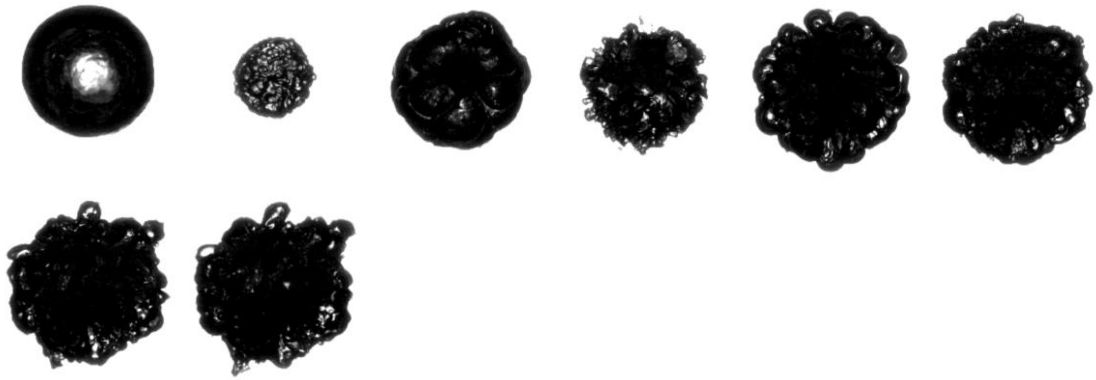

Fig. 3.5 – Vapor bubble oscillations after unstable explosive boiling process is complete. Same droplet as shown in Fig. 3.4, D_0 = 2.12 mm, immersed in glycerol at 1 bar pressure. Time between each image, $\Delta t \approx 1.2$ ms.

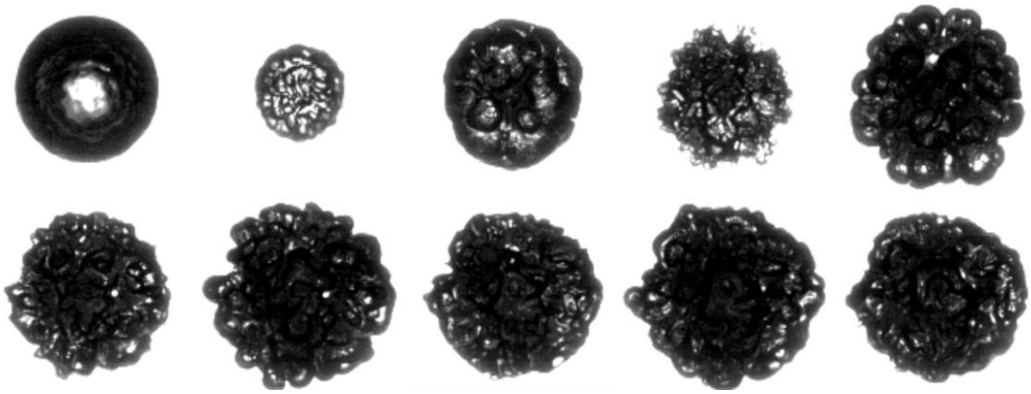

Fig. 3.6 – Vapor bubble oscillations after unstable explosive boiling process is complete. Initial diameter, D_0 = 1.18 mm, immersed in glycerol at 1 bar pressure. Time between each image, $\Delta t \approx$ 0.9 ms.

Fig. 3.7 – Stable homogenous boiling in a diethyl ether droplet of diameter, D_0 = 1.88 mm, immersed in glycerol at 5 bar pressure. Time between each image, Δt = 1 ms.

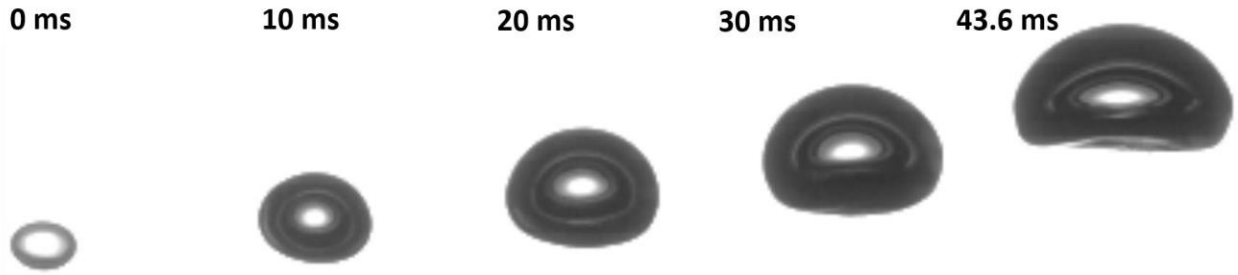

Fig. 3.8 – Bubble dynamics after stable homogenous boiling of a diethyl ether droplet of diameter, D_0 = 2.73 mm, immersed in glycerol at 3 bar pressure. Image 1 shows the initial diethyl ether liquid droplet. Images 2 through 5 show the resulting bubble dynamics.

3.2 Droplet Growth

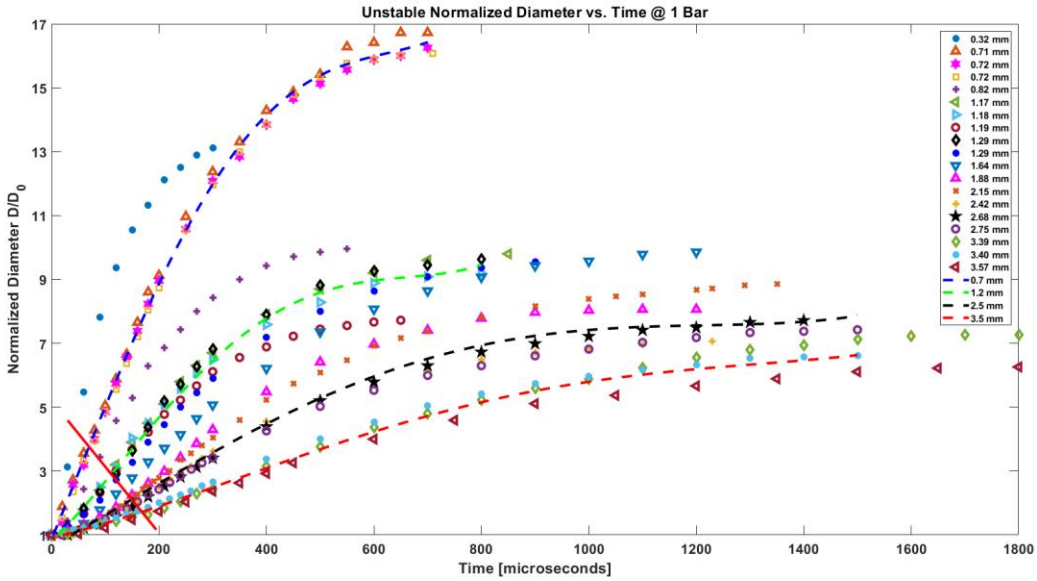

Fig. 3.9 – Normalized droplet and subsequent bubble diameter vs. time at 1 bar pressure for unstable explosive boiling. Empirical curve fits for droplets with initial diameter $D_0 \approx$ 0.7 mm, 1.2 mm, 2.5 mm, and 3.5 mm are shown. Solid red line depicts the approximate end of vaporization.

Normalized droplet and subsequent bubble diameter during unstable explosive boiling and ensuing vapor bubble expansion are shown in Fig. 3.9 and Fig. 3.11. For this normalized diameter metric, at the initial nucleation time, t = 0 µs, as the bubble just start to grow, the droplet diameter was measured. All diameter measurements are taken horizontal – or in other words, normal to the vertical axis of the droplet column – unless otherwise noted, in order to minimize the effect of buoyancy. As the vapor bubble grows inside the droplet, as illustrated in Fig. 3.1, it pushes the droplet, expanding it as the liquid droplet is converted into bubble vapor. Eventually the droplet grows to the extent that it breaks through the droplet interface with the

ambient host fluid. At this point the diameter measured here is simply the maximum horizontal diameter extent of the combined liquid droplet and vapor bubble, as shown in Fig. 3.10. Diameter measurements are accurate to ±0.05 mm. Upon complete evaporation of the liquid droplet, and complete replacement by the vapor bubble, the vapor bubble is simply measured to attain the diameter. This provides a seamless transition in diameter measurements from liquid droplet to vapor bubble. The measurement is completed upon the vapor bubble reaching its maximum diameter, right before starting to contract. In stable cases, the measurements are taken until buoyant forces began to play a significant role, as shown in Fig. 3.8.

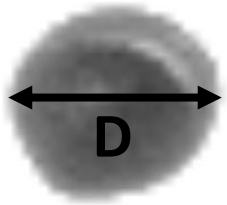

Fig. 3.10 – Liquid droplet/vapor bubble diameter, D, measurement methodology.

The diameter presented here is normalized by the initial horizontal diameter of the liquid droplet to better show the droplet and vapor bubble growth in relation to their respective initial droplet diameters. Generally, the normalized diameter vs. time curve for unstable explosive boiling follows a roughly S-shape curve, starting at $D/D_0 = 1$. At smaller initial droplet diameters, there is little to no ramp up region so do not resemble this S-shape curve as accurately, the normalized diameter reaches linear growth nearly instantly. This is believed to be because, for smaller initial diameter droplets, the incipient vapor bubble becomes large in relation to the liquid droplet more rapidly and therefore the liquid droplet's growth reflects the vapor bubbles growth sooner than in larger initial droplet diameter cases. The bubble growth appears to reach a maximum growth rate quickly, then slowly decelerates until the maximum diameter is reached. Smaller-diameter droplets attain a larger normalized diameter than their larger sized droplet counterparts. Smaller sized droplets also grow faster during the explosive boiling process and ensuing vapor bubble expansion, attaining a larger maximum growth rate than their larger diameter counterparts. The maximum growth rate is typically reached within microseconds of nucleation. Smaller droplets reach max diameter in a shorter duration than their larger counterparts. These trends hold true for elevated pressures as well. The solid red line depicts the approximate end of vaporization. The duration of vaporization, until the liquid droplet is fully evaporated is short compared to the full length from initial nucleation to maximum extent of bubble growth. Larger initial diameter droplets take longer to vaporize than smaller initial diameter droplets since, as will be discussed later, there is no correlation between initial droplet

diameter size and larger droplets take longer for a fixed evaporative velocity interface to propagate across.

D_0 was measured using the visually-determined horizontal diameter of the initial droplet, prior to nucleation. D was measured in the same fashion. After homogenous nucleation within the droplet, the vapor bubble grows, consuming the droplet. Once the vapor bubble consumes the droplet, the droplet continues to grow due to the bubble's high internal pressure and momentum from the explosive boiling event. D is taken as the diameter of the droplet until the droplet has been consumed by explosive boiling, at which point D is taken as the diameter of the vapor bubble. The droplet and vapor bubble are nearly spherical in shape. The volume of the droplet and subsequent vapor bubble, $\forall$, is simply, $\forall = \frac{4}{3}\pi\left(\frac{D}{2}\right)^3$. The pure vapor bubble diameter from nucleation inside the droplet until vaporization is complete for selected unstable trials at both 1 bar and 2 bar can be seen in Fig. 3.15.

As the ambient pressure is increased, the growth in normalized diameter decreases. From 1 bar to 2 bar, the normalized diameter decreases by 40% or more for similarly sized droplets, shown in Fig. 3.21, Fig. 3.22, and Fig. 3.23. The amount of decrease increases with smaller diameter droplets. Additionally at elevated ambient pressures, the duration to reach max diameter is significantly shorter. The maximum droplet and bubble growth rate is also smaller at higher pressures.

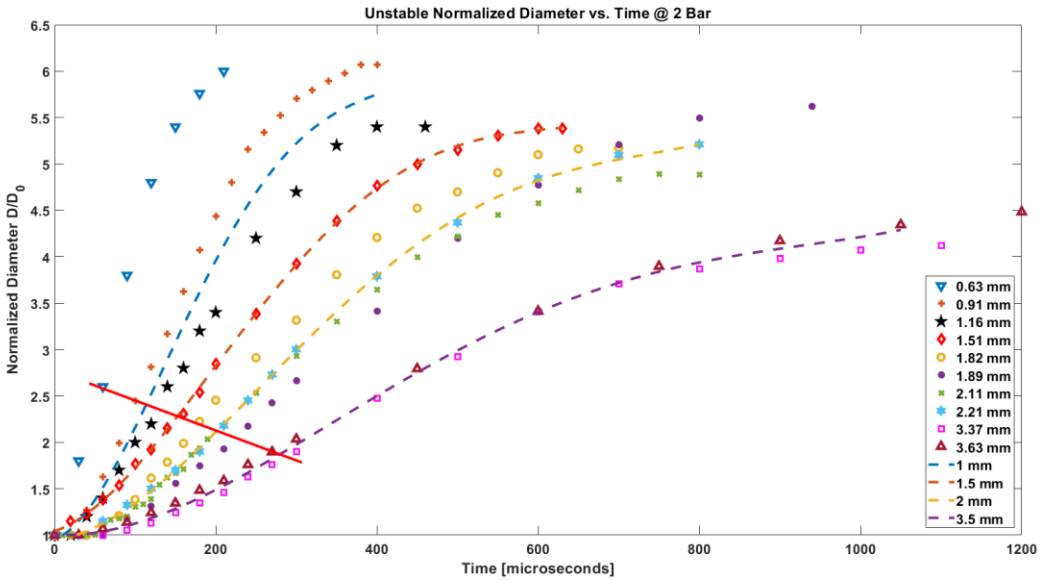

Fig. 3.11 – Normalized droplet and subsequent bubble diameter vs. time at 2 bar pressure for unstable explosive boiling. Empirical curve fits for droplets with initial diameters of $D_0 \approx$ 1 mm, 1.5 mm, 2 mm, and 3.5 mm are shown.

Unstable explosive boiling bubble diameter during vaporization for selected trials at 1 bar and 2 bar pressures is shown in Fig. 3.13. This does not take into account liquid droplet diameter,

only vapor bubble diameter. However, in Fig. 3.14 the diameters have been normalized by their respective initial droplet diameters during vaporization to provide comparison with the previously shown normalized droplet figures. These figures only show the bubble diameter during active vaporization, and cease when the droplet is fully evaporated. The diameters measured in these figures were measured in a similar way to the diameters measured before, by taking the horizontal diameter of the droplet. As noted, only the vapor bubble diameter was measured, not the vapor bubble plus the liquid droplet, as shown in Fig. 3.12. Measurement error in these trials is similar to the measurement error in the previous normalized trials, with vapor bubble diameters accurate down to 0.05 mm. These figures suggest that the vapor bubble grows linearly at a constant rate. There does not appear to be any correlation between vapor bubble growth rate and initial droplet diameter in the non-normalized bubble diameters. Additionally, there is no ramp up region of initial growth, as seen by the liquid droplet/vapor bubble diameter growth shown before. This might be expected, given that the vapor bubble diameter grows linearly, but when the bubble is small in comparison to the droplet, the bubble does not have much influence over the droplet's diameter. This influence slowly ramps up until the droplet diameter growth reflects the bubble diameter growth, and the droplet/bubble hybrid diameter reaches a linear growth region right before the solid red line, as seen in Fig. 3.9 and Fig. 3.11. An inverse correlation between diameter growth rate and pressure can be found here. As pressure is increased, from 1 bar to 2 bar, diameter growth rate drops. This suggest that at higher ambient pressures, the bubble evaporative velocity decreases.

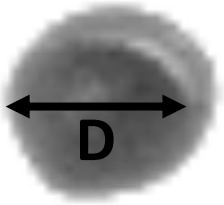

Fig. 3.12 – Vapor bubble diameter, D, measurement methodology.

There is some variability in the vaporization duration, as the vaporization duration does not correlate strongly with initial droplet diameter for this set of data. The solid red line in previous plots suggests that there is a positive correlation between initial droplet diameter and vaporization duration. This is supported by Fig. 3.13 as it shows there is no correlation between vapor bubble growth rate and initial droplet diameter, therefore a larger initial diameter droplet would take longer to be consumed by the vapor bubble. This variation can be explained by the location of the homogeneous nucleation point. Since the droplet is small and heated slowly, the temperature is nearly isotropic throughout, giving a nearly equal chance of a homogenous nucleation point occurring at any point inside the droplet, in theory. In practice, and from

observation, the nucleation point typically appears to occur in the outer 50% of the bubble volume. However, sometimes the nucleation point can occur towards the center of the image of the droplet. This location can be near the apparent center of the droplet or toward the near or far edge of the droplet. It is not possible to distinguish between these two cases due to only having a 2-dimentional view of the droplet. When the former occurs the bubble appears visually to consume the droplet much more rapidly than if the nucleation point occurs closer to the outside edge of the droplet. This occurs because, when the nucleation point is near the edge, the vapor bubble front facing the center of the bubble has essentially the whole diameter of the droplet it must traverse during vaporization, but if the nucleation point occurs close to the center of the liquid droplet, then the vapor bubble interface only has half the diameter of the droplet it must traverse, since it can expand along both directions of that vector, not just one. When the latter occurs, the vaporization front propagates into or out of the imaging plane, which is not measurable from the camera's point of view. Instead what is measured is how the vaporization front propagates outwards towards both droplet edges, and leads to an artificially decreased vaporization time. As a result of this, bubbles that nucleate close to the image center of the droplet have much more rapid vaporization durations than near-edge nucleation points. This leads to the increased variability in vaporization duration displayed in these figures. Lastly, it is important to keep in mind here that measurements are line-of-sight imaging, so it is not possible to determine if the nucleation actually occurs at the center of the droplet.

The bubble volume during unstable vaporization for selected trials at 1 bar and 2 bar pressure is shown in Fig. 3.15. The bubble volume here is approximated as the volume of a sphere, as denoted earlier. This approximation is better at smaller initial droplet diameter sizes than larger sizes as these larger droplets are flatted more moving up through the host fluid giving a less spherical volume for the vapor bubble to expand into. Similarly to the diameter measurements, there is no correlation between initial droplet diameter and vapor bubble volume growth. There is a negative correlation between ambient pressure and vapor bubble growth, with an increase in ambient pressure leading to a slower bubble volume growth rate.

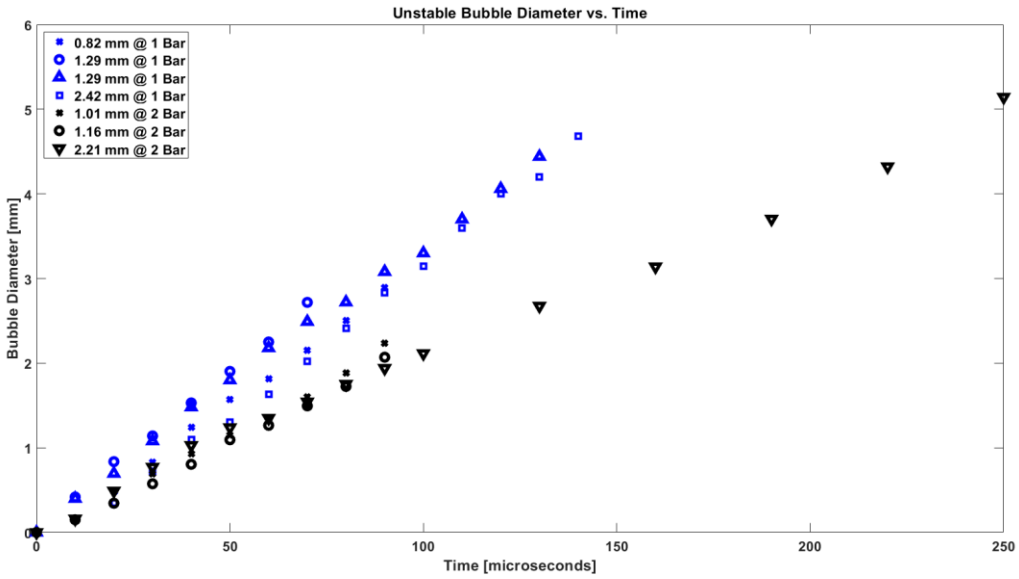

Fig. 3.13 – Bubble diameter during vaporization vs. time for selected trials at 1 and 2 bar pressure for unstable explosive boiling.

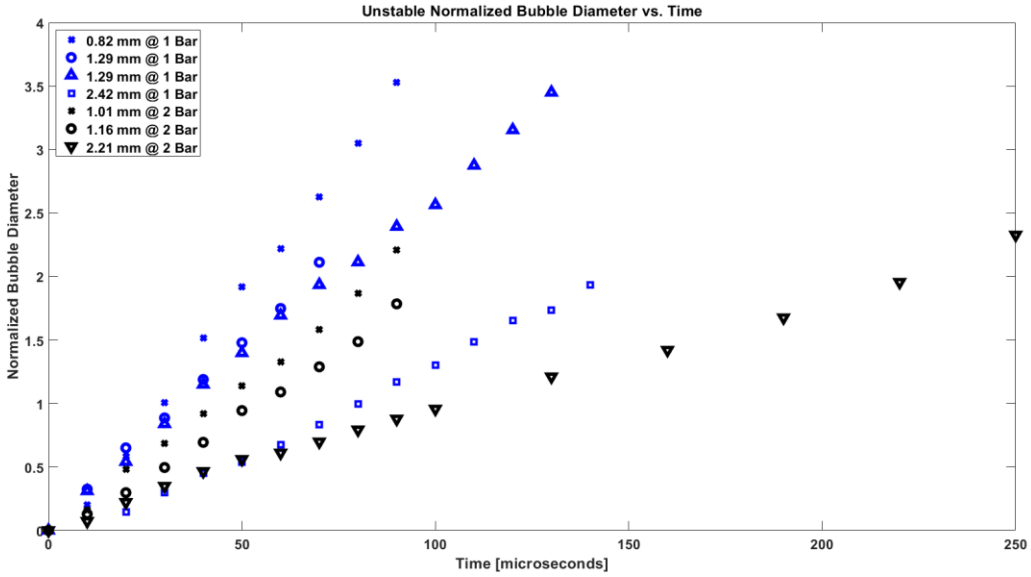

Fig. 3.14 – Normalized bubble diameter during vaporization vs. time for selected trials at 1 and 2 bar pressure for unstable explosive boiling.

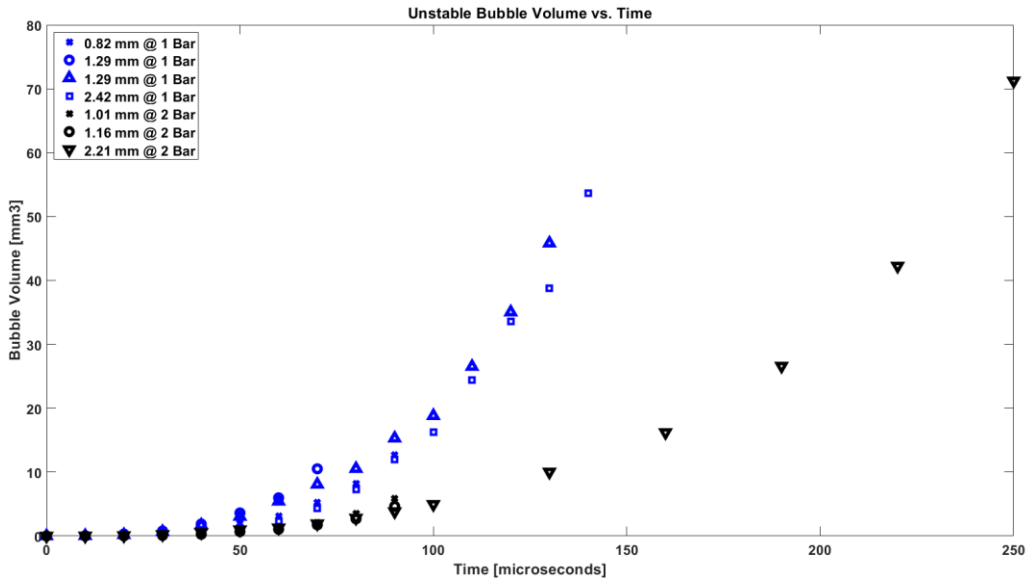

Fig. 3.15 - Bubble volume during vaporization vs. time for selected trials at 1 and 2 bar pressure for unstable explosive boiling.

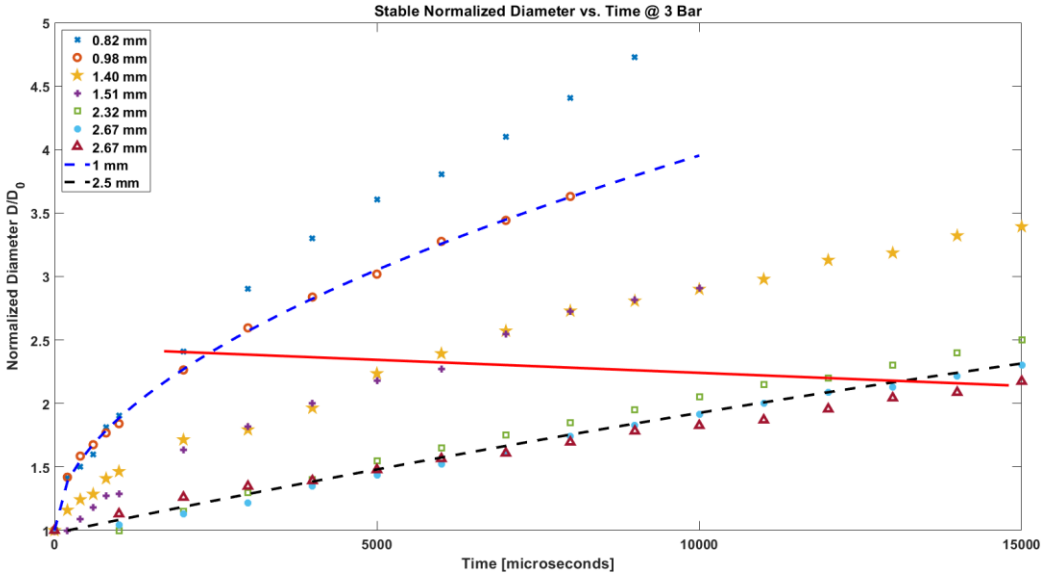

Fig. 3.16 – Normalized droplet and subsequent bubble diameter vs. time at 3 bar pressure absolute for stable boiling. Empirical curve fits for droplets with initial diameters of $D_0 \approx 1$ mm and 2.5 mm are shown.

The normalized bubble diameter, including the liquid droplet diameter during the initial vaporization phase for stable homogenous boiling, is shown in Fig. 3.16 and Fig. 3.17 for ambient pressures of 3 bar and 5 bar absolute, respectively. Commonly, the overall normalized diameter

growth curve for stable boiling appears mostly linear with time, with notable exceptions being the smaller initial diameter droplets at 3 bar. For these smaller diameter droplets, as time progresses a slight flattening out of the curve leads to a mildly decreasing growth rate, eventually approaching linear. Similarly to the smaller droplet diameter unstable cases for 1 bar and 2 bar, these smaller droplet diameter stable cases for 3 bar grow rapidly initially before leveling off due to the impact the incipient vapor bubble has on the comparatively small liquid droplet. The 5 bar small initial droplet diameter trials do not quite have this quick growth period for two reasons. First, the 5 bar trials, at 1.29 mm and 1.40 mm, the initial droplet diameters are not as small as the 0.82 mm and 0.98 mm 3 bar trials and therefore display less aggressive initial growth behavior and are more comparable to the 1.40 mm or 1.51 mm 3 bar trials. Second, as pressure increases there is a general flattening of the growth curve, with non-linear behavior mostly smoothed out, which is on display in these 5 bar trials, especially in the smaller initial droplet diameter curves. From experimental observation, the bubble continues to grow past the time frame of Fig. 3.16 and Fig. 3.17 as buoyant effects become relevant, flattening the bubble out as it rises until it is out of the field of view of the observing high-speed camera, shown in Fig. 3.8. Similar bubble-growth trends with varying ambient pressure and initial droplet diameter as seen for the unstable explosive boiling trials are seen in these stable boiling trials. In particular, small diameter droplets grow to larger normalized diameter than large diameter droplets. Small diameter droplets also grow at a faster growth rate than large diameter droplets. Furthermore, small diameter droplets grow for a shorter duration than large diameter droplets, emphasized by less linear growth and more flattening out of the curve fits as time progresses for small diameter droplets. Also similarly to the unstable trials, as ambient pressure is increased, the normalized diameter and normalized diameter growth rate decrease substantially.

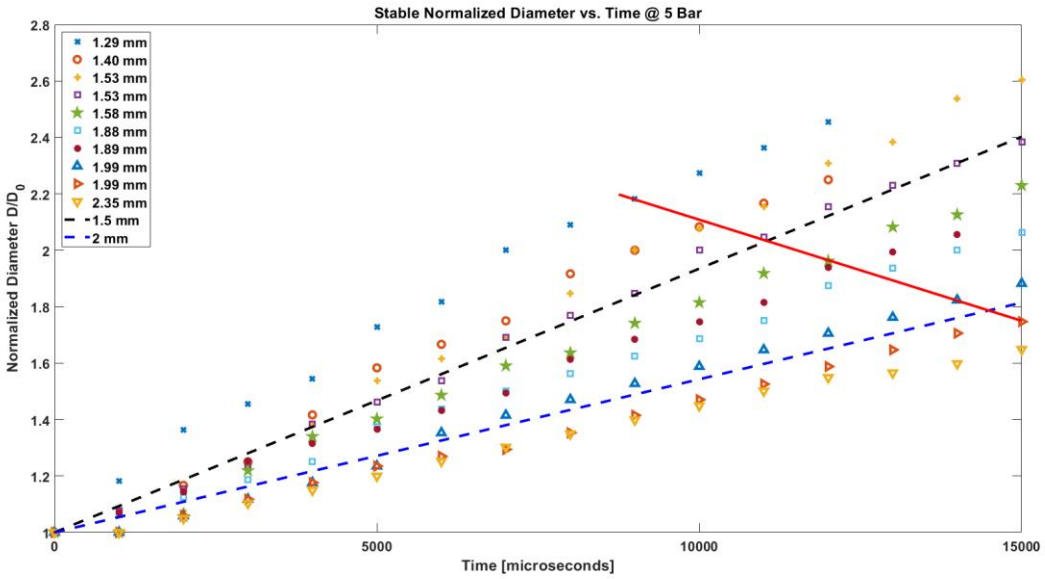

Fig. 3.17 – Normalized droplet and subsequent bubble diameter vs. time at 5 bar pressure absolute for stable boiling. Empirical curve fits for droplets with initial diameter $D_0 \approx 1.5$ mm and 2 mm are shown.

Stable homogeneous boiling bubble diameter during vaporization for selected trials at 3 bar and 5 bar pressure absolute are shown in Fig. 3.18 and Fog. 8.2. Similarly to Fig. 3.13 and Fig. 3.14, these do not take into account liquid droplet diameter, only vapor bubble diameter. Additionally, only the 1.02 mm and 1.41 mm at 3 bar show the whole vaporization, the rest only show up to a chosen cut-off time of 4 ms. This time was chosen to emphasis the incipient vapor bubble growth and early bubble growth behavior. All diameter measurements were taken similarly as before with bubble diameter measured in the horizontal direction as to minimize buoyancy influence. With a shorter time step between measurements in Fig. 3.18 and Fig. 3.19 on the order of 100 µs as opposed to 1 ms for Fig. 3.16 and Fig. 3.17, as well as only measuring the vapor bubble not the vapor bubble plus liquid droplet, the early vapor bubble behavior can be better understood. The bubble diameters exhibit an early rapid growth before leveling off into what appears to be linear growth. In contrast with the unstable trials in Fig. 3.13 and Fig. 3.14, which appear linear, the stable vapor bubble growth over the whole curve is non-linear. However, if only the time rage of the unstable trials is examined, nucleation to less than or equal to 250 µs, for the stable trials, while the data density is not high over that range, it can be approximately interpolated to be a linear growth rate as well. It is thought that due to the order of magnitude greater time range of the stable trials, damping effects play a greater role and, when combined with the slower stable boiling evaporative fluxes, contribute to the curved, non-linear shape. Higher ambient pressure results in a flattening of the quick, initial rise which is consistent with what is previously observed. When not normalizing the vapor bubble diameter by the initial droplet diameter, the growth rates appear to not be correlated to initial droplet size. However, when grouping the droplets by pressure, there does appear to be a correlation

between ambient pressure and growth rate. This reinforces what has been previously seen in the unstable cases, that there is a consistent, or rather, roughly fixed, growth rate for all vapor bubbles for various initial droplet sizes at a certain ambient pressure, but increasing the ambient pressure decreases the growth rate.

The bubble volume during stable vaporization for selected trials at 3 bar and 5 bar pressure is shown in Fig. 3.20. The same spherical and small initial droplet diameter approximations for Fig. 3.15 apply to this figure as well. Similar to the unstable cases, for the stable trials, there does not appear to be a strong correlation between initial droplet diameter and bubble volumetric growth rate. However, like the unstable trials, there is a correlation between the ambient pressure and bubble volumetric growth rate, with an increase in pressure correlating to a drop in volume, similar to the bubble diameter correlation with ambient pressure.

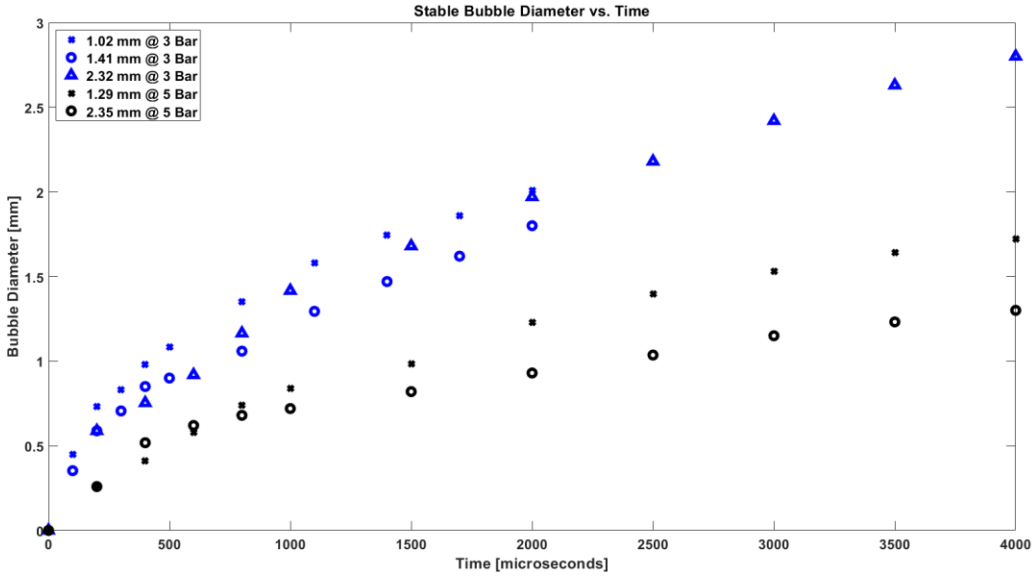

Fig. 3.18 – Bubble diameter during vaporization vs. time for selected trials at 3 and 5 bar pressure for stable boiling.

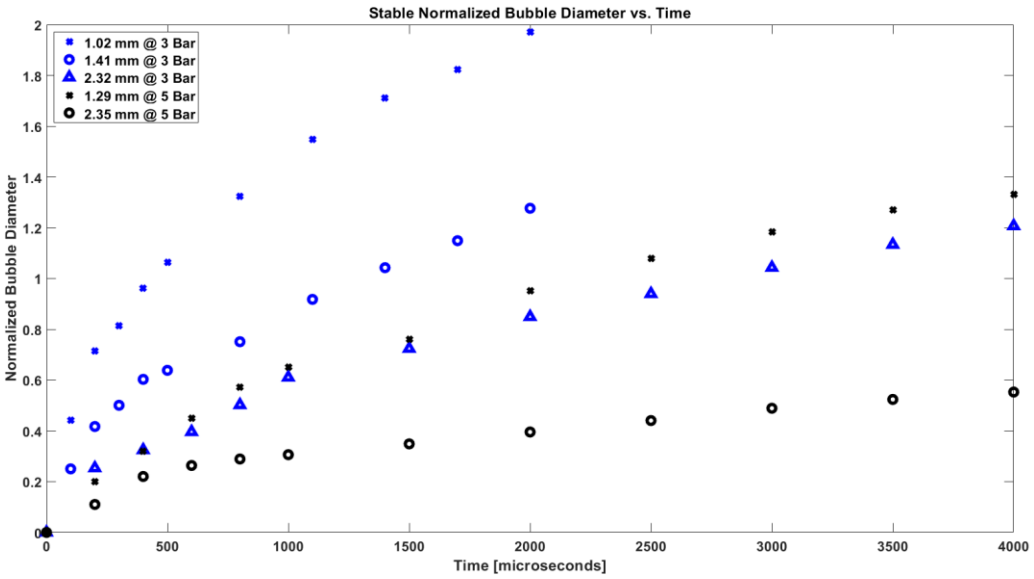

Fig. 3.19 – Normalized bubble diameter during vaporization vs. time for selected trials at 3 and 5 bar pressure for stable boiling.

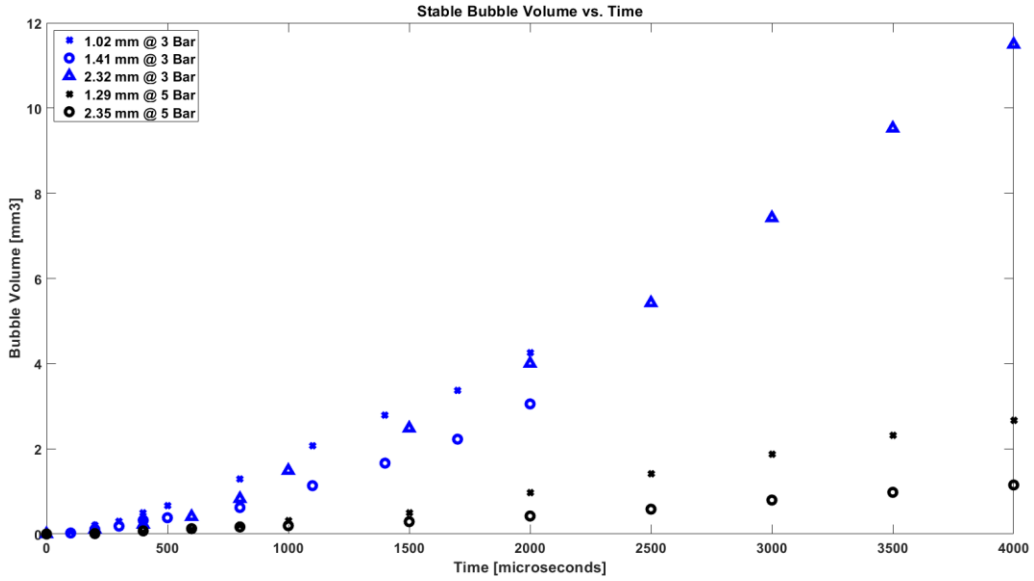

Fig. 3.20 - Bubble volume during vaporization vs. time for selected trials at 3 and 5 bar pressure for stable boiling.

The correlation between normalized diameter and ambient pressure can be further examined across both unstable and stable boiling regimes in Figs. 3.21 – 3.24. Fig. 3.21 gives a good perspective on the actual difference between unstable and stable boiling for both normalized diameter growth rate and normalized diameter maximum growth. An attempt was made to take into account initial droplet diameter by providing two sets of data for pressure 1 bar to 5 bar. The two sets are for approximately D_0 = 1.26 mm and D_0 = 2.32 mm so that pressure

may be looked at independently. It is apparent from this figure how much more rapidly and larger unstable boiling, 1 bar and 2 bar, grows the vapor bubble when compared to stable boiling, 3 bar and 5 bar. In addition, within either boiling regime, whether unstable or stable, the role increased ambient pressure can be examined, reinforcing what has been stated previously that increasing the ambient pressure decreases both the normalized diameter growth rate as well as the maximum normalized diameter growth. In addition, Fig. 3.21 illustrates the time duration difference for unstable and stable boiling from incipient nucleation to maximum bubble growth, showing how much more rapidly unstable boiling vaporizes the liquid droplet than stable boiling. Fig. 3.22 is the same as Fig. 3.21 but plotted on log-log axes for better data readability. This plot better shows the shape of the curves in comparison to each other while still showing the significant differences between unstable and stable vaporization, such as the growth rate and the vaporization duration. Fig. 3.23 and 9.2 break Fig. 3.21 down into unstable and stable parts for improved readability as well. Fig. 3.23 shows only the unstable boiling data, whereas Fig. 3.24 shows only the stable boiling data. These illustrate the role ambient pressure plays when initial droplet diameter is controlled for, showing how increasing the pressure decreases the growth rate substantially.

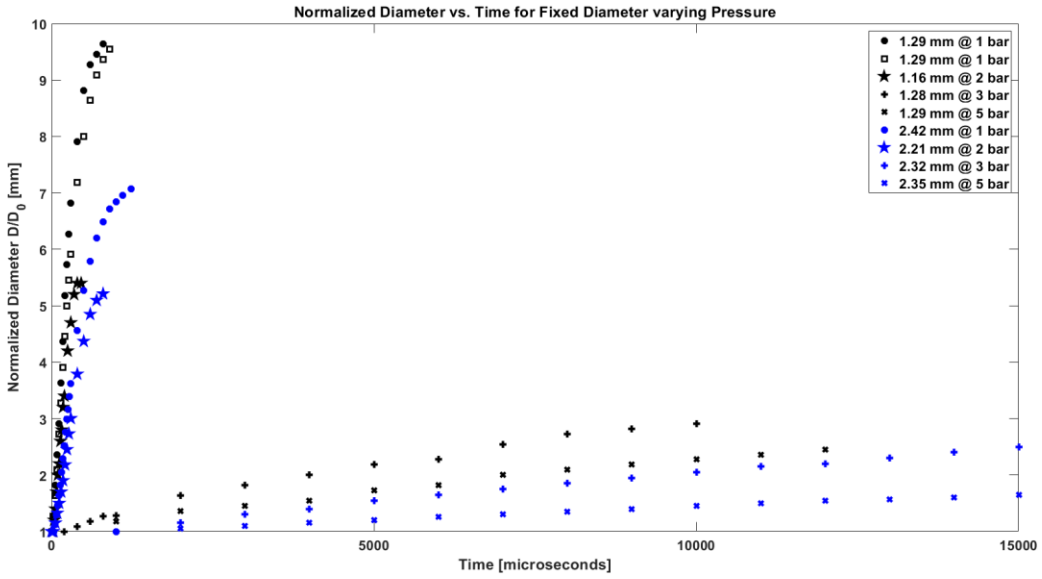

Fig. 3.21 – Normalized droplet and subsequent bubble diameter vs. time for approximately D_0 = 1.26 mm and D_0 = 2.32 mm initial droplet size at 1, 2, 3, and 5 bar pressures.

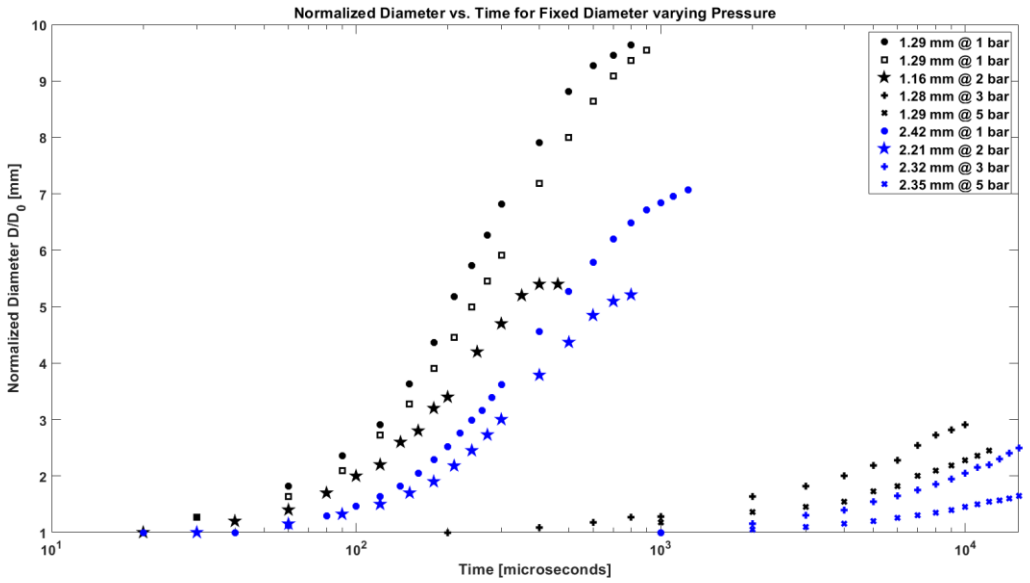

Fig. 3.22 – Normalized droplet and subsequent bubble diameter vs. time for D_0 = 1.26 mm and D_0 = 2.32 mm initial droplet size at 1, 2, 3, and 5 bar pressures. Log time axis to better show data.

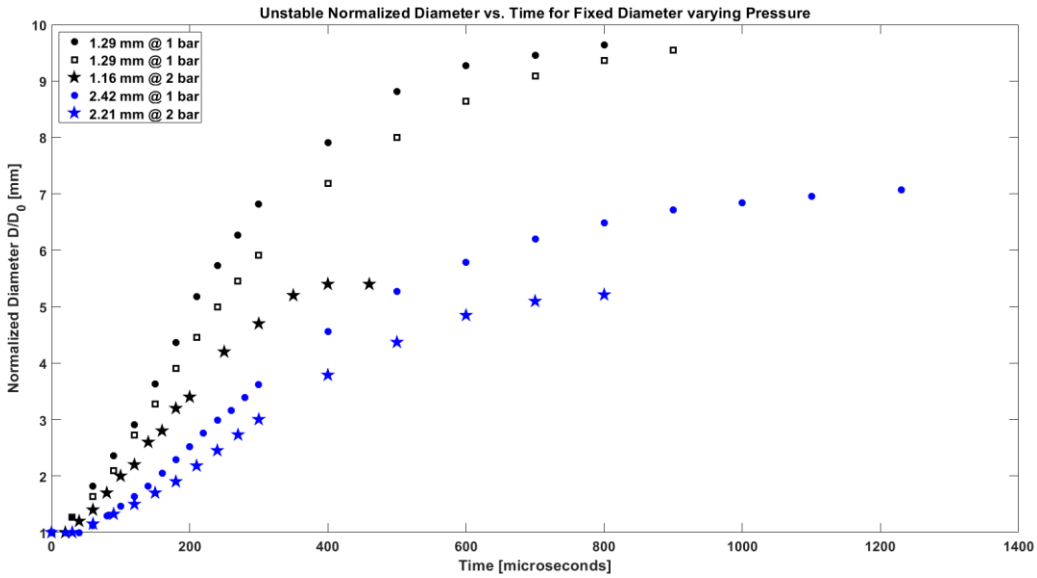

Fig. 3.23 – Unstable normalized droplet and subsequent bubble diameter vs. time for D_0 = 1.29 mm and D_0 = 2.32 mm initial droplet size at 1 and 2bar pressures.

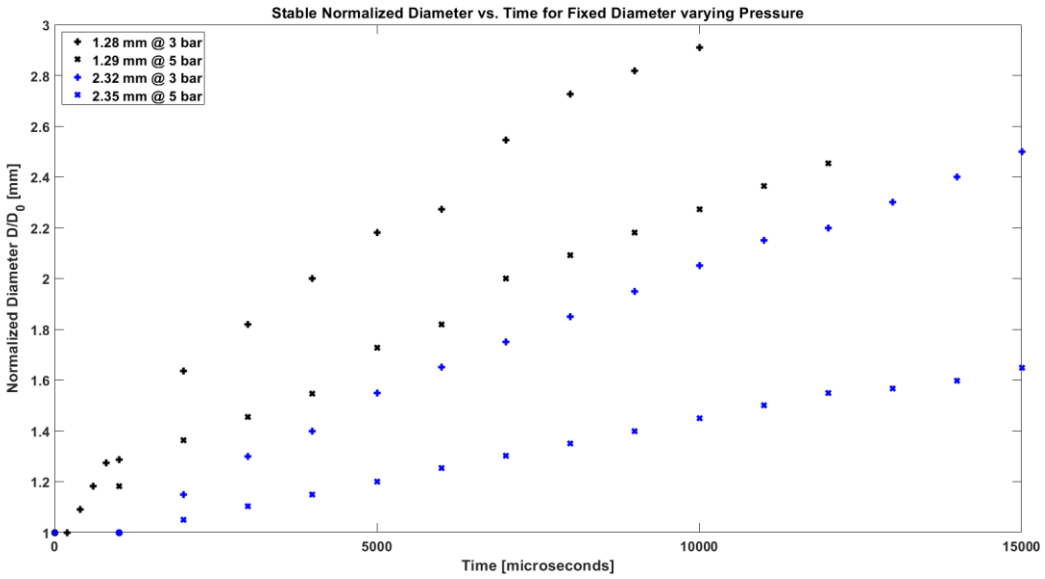

Fig. 3.24 – Stable normalized droplet and subsequent bubble diameter vs. time for D_0 = 1.28 mm and D_0 = 2.33 mm initial droplet size at 3 and 5 bar pressures.

3.3 Bubble Interface Velocity

During the explosive boiling process within a droplet, an interface forms between the yet-to-be vaporized droplet liquid and the growing evaporated vapor bubble. This liquid-vapor interface, essentially the vapor bubble surface, propagates through the liquid droplet, vaporizing the liquid as it travels. The measured velocity of this liquid-vapor interface vs. time is shown in Fig. 3.25 and Fig. 3.30 for unstable boiling at 1 bar and 2 bar pressures, respectively. This data consists of roughly three phases, the first is a rapid initial rise in velocity from zero to a velocity maxima, occurring on the order of tens of microseconds. The second phase is a rapid drop to a roughly steady state period in the interface velocity for the duration of the droplet vaporization as the evaporative liquid-vapor interface propagates across the droplet, lasting 100 µs to 200 µs in duration. The third phase occurs only once vaporization is complete when the liquid droplet has been fully evaporated and consists of a long, roughly-linear decrease in velocity to zero, coinciding with the bubble attaining maximum diameter. This third phase lasts anywhere between a few hundred microseconds to 1.5 ms, correlating heavily with initial droplet diameter with larger droplets taking longer.

Interface velocity is measured by first finding the nucleation point and centering this as the origin then measuring the distance from the origin to the interface, *D*, at regular time steps as shown in Fig. 3.29. The bubble interface velocity, $\overline{v}_b$, is then calculated over time duration, $\Delta t = t_{i+1} - t_i$, using, $\overline{v}_b = \frac{1}{t_{i+1}-t_i}\int_{t_i}^{t_{i+1}} v(t)\,dt = \frac{x_{i+1}-x_i}{t_{i+1}-t_i}$, where x_{i+1}, is the position at time, t_{i+1}, and x_i, is the position at time, t_i. As a result of differentiating experimental results, the error

is increased. The unstable interface velocity is accurate to ±5 m/s and the stable interface velocity is accurate to ±0.15 m/s. As stated previously, the vast majority of nucleation points occur close to the edge of the liquid droplet. The velocities measured here are all measured in the direction from the nucleation point across the droplet, away from the near droplet edge. If the nucleation point occurs near the top or the bottom of the droplet so that the measurement direction is in a vertical direction, corrections are made to account for the vertical movement of the droplet due to buoyancy. This only occurred in especially large diameter droplets. The part of the bubble interface measured is always the side moving across the droplet, never the side moving toward the near edge of the droplet. This part of the bubble interface reflects the maximum interface velocity of the bubble, as it has room to propagate freely. The opposite side of the bubble interface, the part of the interface that expands towards the near droplet edge quickly reaches that edge, breaking through, and subsequently slowing down as no more active vaporization is occurring to drive it, only being propelled further by vapor expansion inside the bubble.

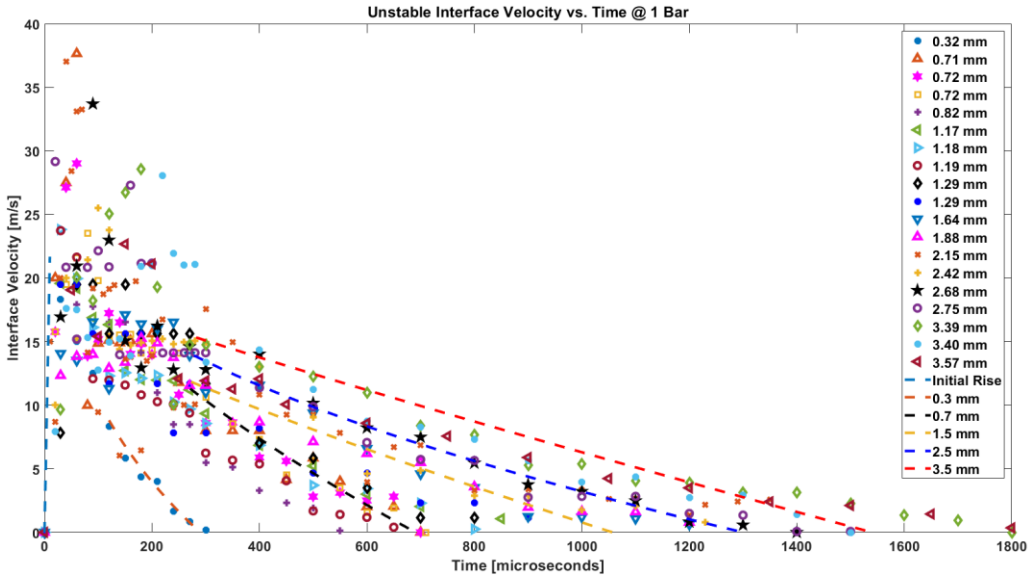

Fig. 3.25 – Interface velocity vs. time at 1 bar pressure for unstable explosive boiling. Empirical curve fits for droplets with initial diameter $D_0 \approx$ 0.3 mm, 0.7 mm, 1.5 mm, 2.5 mm, and 3.5 mm are shown.

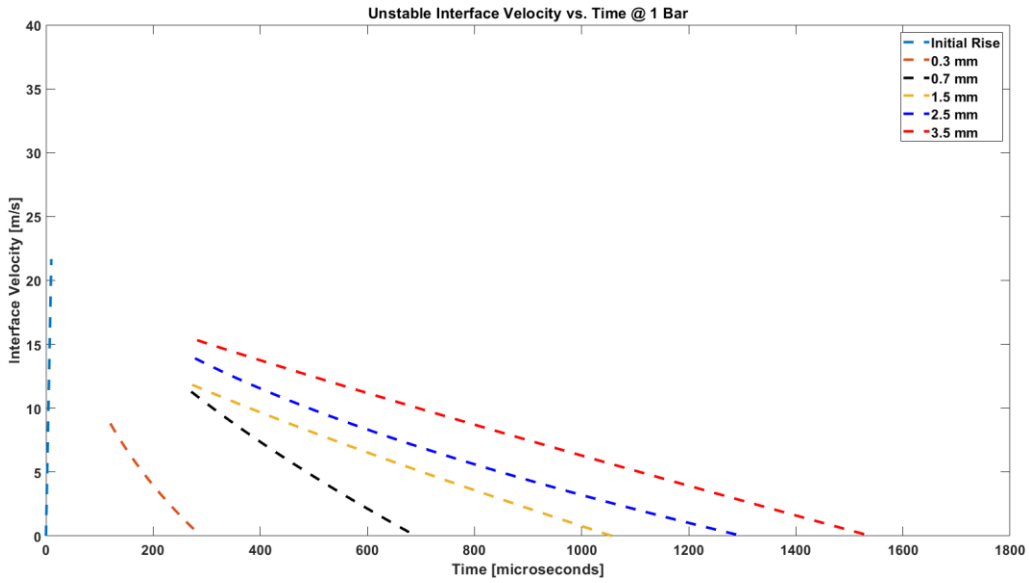

Fig. 3.26 – Empirical curve fits for interface velocity vs. time at 1 bar pressure for unstable explosive boiling. Initial diameter $D_0 \approx$ 0.3 mm, 0.7 mm, 1.5 mm, 2.5 mm, and 3.5 mm are shown.

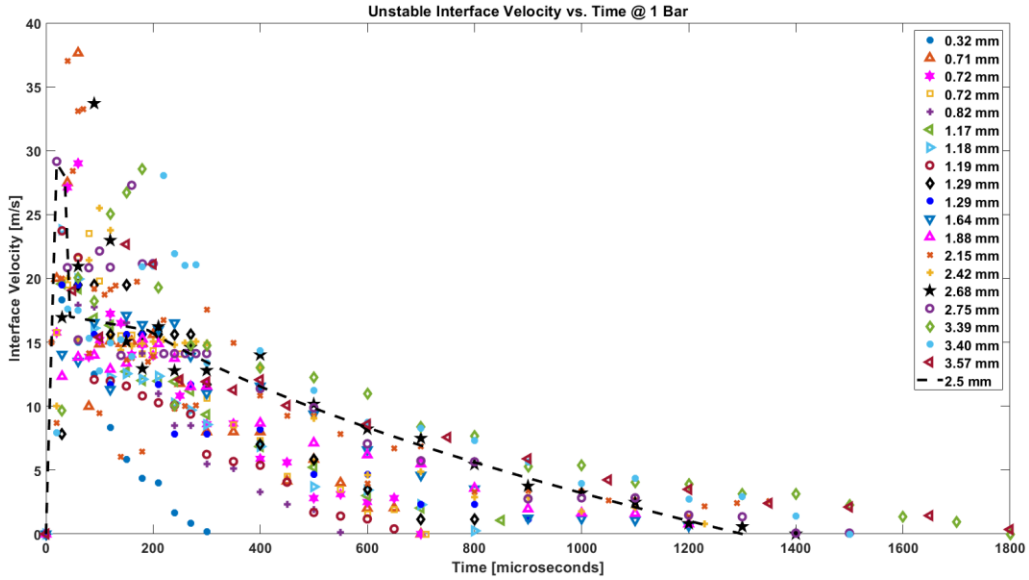

Fig. 3.27 – Interface velocity vs. time at 1 bar pressure for unstable explosive boiling. Curve for a rough estimation of the explosive boiling velocity behavior plotted for $D_0 \approx$ 2.5 mm. Behavior consists of a rapid initial rise to peak velocity, then a rapid descent to a relatively constant velocity period for the duration of the vaporization of the droplet. Upon complete evaporation of the droplet, the vapor bubble interface velocity then slows to zero.

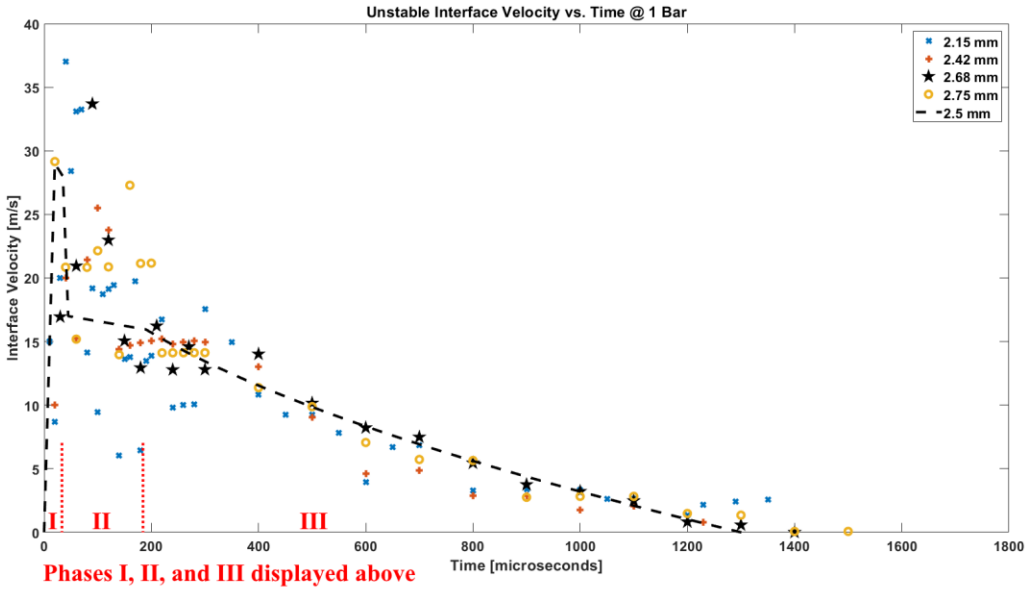

Fig. 3.28 – Interface velocity vs. time at 1 bar pressure for unstable explosive boiling. Curve for a rough estimation of the explosive boiling velocity behavior plotted for $D_0 \approx 2.5$ mm. Only relevant trials to 2.5 mm are shown. Phases I, II, and III range are displayed.

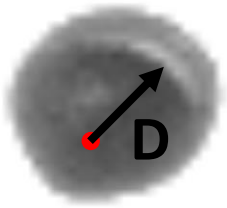

Fig. 3.29 – Vapor bubble diameter, D, measurement methodology. D is differentiated verses time to determine the interface velocity. The red dot is the nucleation point, the fixed origin distance measurements are taken from.

An attempt is made to minimize the time duration on a case-by-case basis since, by minimizing the time duration, average velocity approaches instantaneous velocity. This approach is iterated throughout the explosive boiling process to calculate the liquid-vapor interface velocity with small enough time durations to estimate instantaneous velocity. During explosive boiling, time durations of 20 µs, 30 µs, and 50 µs are utilized, with the longer time durations used for larger initial diameter droplets. After the vaporization process is complete, when the liquid droplet is consumed, and the vapor bubble is still expanding within the host liquid, larger time durations of 50 µs, 100 µs, and 150 µs are used as the interface speed slows, with larger time durations again being used with larger initial diameter droplets. The shorter time durations of 20

μs, 30 μs, and 50 μs are near the minimum useable time duration, as due to the limited video spatial resolution, any shorter time durations will result in no discernible measurable movement.

Best-fit curves are plotted for a variety of initial droplet diameters in Fig. 3.25 and Fig. 3.30 as well as plotted without the raw data for better readability in Fig. 3.26 and Fig. 3.31, respectively. These best fit curves consist of the first aforementioned phase, an initial rise which is believed to be similar for all initial droplet diameters for a fixed ambient pressure, and the third phase, a near-linear slowing down curve where the interface velocity drops to zero overtime after droplet vaporization is complete. The second phase has been purposely omitted from these best fits since no definite correlation can be found between initial droplet diameter and vapor bubble interface velocity. This is apparent because the difference between 0.5 mm and 3.5 mm for the initial droplet diameter is not enough to change the continuum approximation for the droplet fluid. It is apparent from these best fit curves that larger diameter droplets take longer to undergo the full vaporization process and reach zero interface velocity. From empirical observation, the rough shape of the interface velocity curve consists of a rapid velocity rise from zero to a velocity maximum, here termed phase I, then a rapid decline to a nearly-constant velocity segment during the completion of the droplet boiling process, phase II. Once the droplet has been fully evaporated, the vapor bubble interface continues to expand outward against the host liquid, during which the interface velocity decays to zero, phase III. This decay to zero can be seen clearly in the diameter data in Fig. 3.9 and Fig. 3.11. This rough interface velocity curve can be seen for an approximate D_0 = 2.5 mm droplet best fit in Fig. 3.27. Additionally, this same best fit can be seen with only raw data of similar initial droplet diameter with the rough range of these aforementioned phases in Fig. 3.28. A velocity curve of similar magnitude was seen by McCann in a more limited fashion as he could only collect five data points per trial [22]. Additionally, general shape, but not magnitude, of the velocity curve in Fig. 3.28 is reflected in past theoretical models such as the dubbed “classical model” by Prosperetti & Plesset and the Thornton Research Centre (TRC) model by Nguyen *et al.* [12, 16]. Both of these models rapidly peak at an interface velocity of around 50 m/s before decreasing, shown in Appx. 6.

There does not appear to be a strong correlation between initial droplet diameter and the peak evaporating interface velocity during phase I, nor does there appear to be a strong correlation between droplet diameter and steady-state velocity during phase II. Rather, it appears that the velocity of the interface as it propagates across the droplet appears to be more or less uniform, with a slight decrease from the initial nucleation velocity experienced in the first 50 μs, with smaller droplets peaking more quickly and larger droplets taking longer to peak. The initial droplet diameter does appear to have a correlation to the vaporization temporal duration as the evaporation front interface velocity is independent of initial droplet diameter, evaporation takes longer to propagate across a larger diameter droplet. Pressure has a strong impact on peak interface velocities, with an elevated pressure correlating to a lower peak interface velocity. By doubling the ambient pressure from 1 bar absolute to 2 bar absolute, the average peak interface velocity decreases by approximately 30-35%. Average peak interface velocities at 1 bar pressure are in the 20 m/s range, with outliers approaching 40 m/s. In comparison, for 2 bar pressure,

average peak interface velocities are around 14 m/s, with outliers around 25 m/s, both significantly lower than 1 bar pressure.

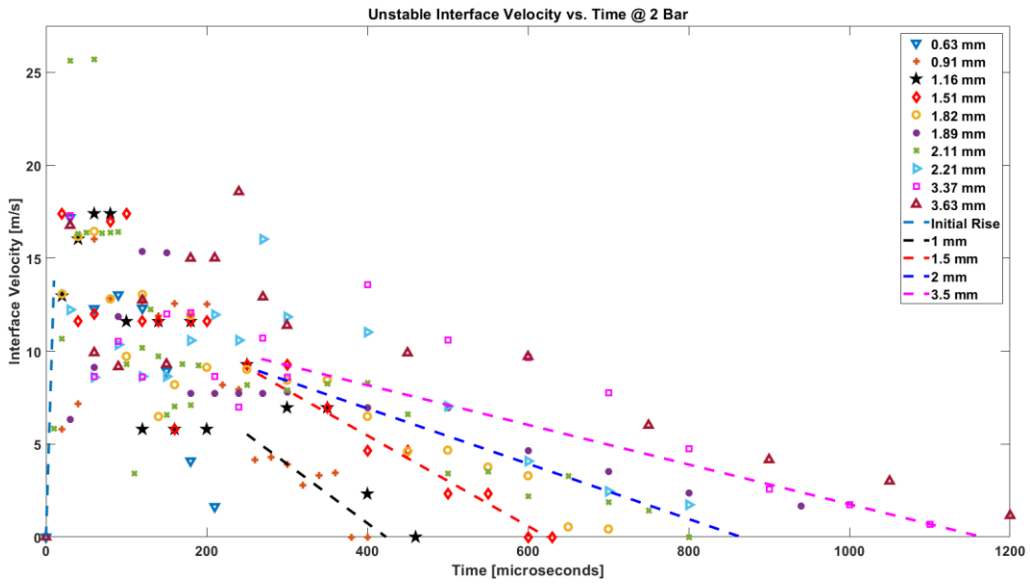

Fig. 3.30 – Interface velocity vs. time at 2 bar pressure for unstable explosive boiling. Empirical curve fits for droplets with initial diameter $D_0 \approx$ 1 mm, 1.5 mm, 2 mm, and 3.5 mm are shown.

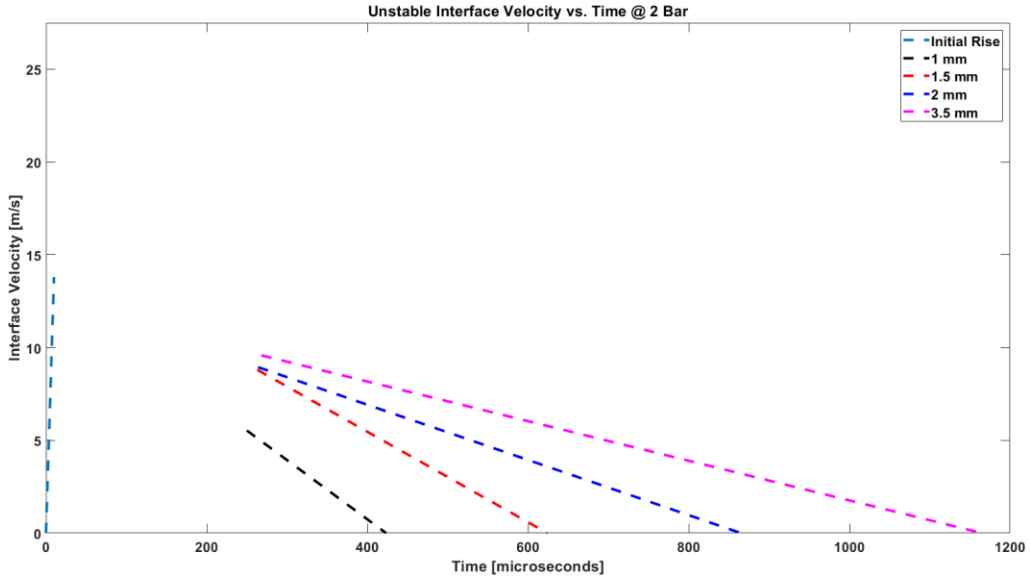

Fig. 3.31 – Empirical curve fits for interface velocity vs. time at 1 bar pressure for unstable explosive boiling. Initial diameter $D_0 \approx$ 1 mm, 1.5 mm, 2 mm, and 3.5 mm are shown.

Unstable averaged bubble interface velocity vs. time during vaporization for selected trials at 1 bar and 2 bar absolute ambient pressures are shown in Fig. 3.32. The data are only measured during vaporization, measurements ceasing when the vapor bubble has fully

evaporated the droplet. The data are measured in a different way as before leading to the averaged distinction. This velocity data was calculated by differentiating the diameter growth data then dividing by two to account for the diameter growth data being a diameter not a radius, or in other words, representing both "sides" of the growing vapor bubble not just one side or one interface. As a result of both sides of the bubble being differentiated to attain this velocity data and then averaged together, it has the averaged distinction, as opposed to the previous velocity data, in Fig. 3.25 and Fig. 3.30, being close to maximum vapor bubble velocity. This results in the averaged interface velocity data presented in Fig. 3.32 to be approximately 20% lower than the velocity data presented in Fig. 3.25 and Fig. 3.30. This is done for two reasons, the first is to measure the velocity via multiple methodologies to ensure ballpark consistency and to try to provide an envelope for the data. The second is to provide a bubble interface velocity averaged around the whole bubble for mass flux and mass flow rate calculations that will be presented later on.

Fig. 3.33 shows the unstable averaged bubble evaporation velocity vs. time for selected trials at 1 bar and 2 bar absolute ambient pressures. Similarly to the averaged bubble interface velocity, the evaporation velocity is also averaged around the whole vapor bubble. The evaporation velocity is the relative velocity of the bubble evaporation interface in relation to the exterior liquid droplet growth. As the bubble consumes the droplet, the bubble grows, not just from the bubble interface propagating across the droplet evaporating it, but also from the expansion of liquid into vapor. The evaporation velocity attempts to account for this vapor expansion by taking into account the movement of the droplet interface, assuming that if there was no vapor expansion at all, the droplet would not expand as the bubble consumed it. The total evaporation velocity, v_e, is calculated using, $v_e = v_b - v_d$, where v_b is the total vapor bubble interface velocity used in Fig. 3.32, and v_d is the total liquid droplet interface velocity. These total velocities account for the bubble and droplet expanding in both directions. To calculate a single interface velocity, these total velocities must be divided by two in order to average them as they are currently the sum of both opposite interfaces. Therefore, the plotted evaporation velocity in Fig. 3.33, called the averaged bubble evaporation velocity, $\bar{v}_e$, is calculated using, $\bar{v}_e = \frac{v_b - v_d}{2} = \frac{v_e}{2}$.

The evaporation velocity gives a good representation of how quickly the unstable interface actually propagates across the droplet as well as the evaporation front speed of explosive boiling. Since the relative vaporization interface velocity is taken into account, the unstable averaged evaporation velocity is approximately 60% slower than the unstable averaged bubble interface velocity that does not account for vapor expansion. However, both display the same trends in varying ambient pressure and initial droplet diameter. There does not appear to be a correlation between initial droplet diameter and either interface velocity or evaporation velocity. There does appear to be a strong correlation between ambient pressure and both velocities with an increase in ambient pressure decreasing both velocities. Interestingly, for the interface velocity, the decrease from 1 bar to 2 bar, approximately 30%, is larger than the

decrease for evaporation velocity from 1 bar to 2 bar, 20%. This makes sense, however, since the interface velocity does not account for the vapor expansion, therefore is impacted it, and pressure has an impact on vapor expansion as well, increasing the pressure will disproportionally affect the interface velocity more than the evaporation velocity, which does account for the vapor expansion. Best fit curves are plotted on Fig. 3.32 and Fig. 3.33 for individual trials. There is no strong correlation in the data with time, further reinforcing that the interface velocity during active vaporization is fixed. The flat line segment of the best fit curves is the average of the data. Initial rapid rise is also included in the best fit. Notably lacking from this data is the initial velocity maxima, phase I, as shown in Fig. 3.27 and Fig. 3.28. This is believed to be because the averaged nature of this data may artificially conceal this maximum.

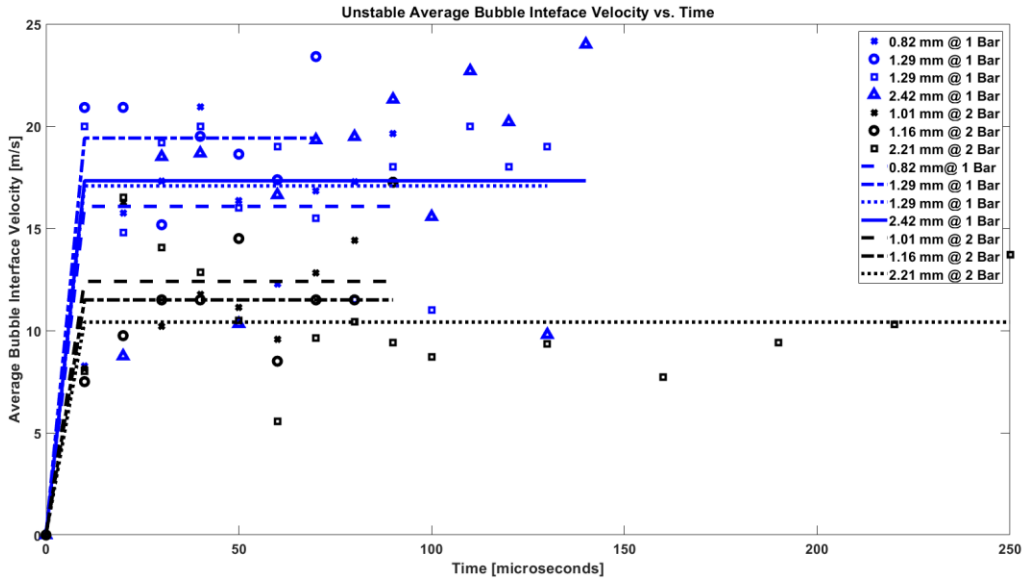

Fig. 3.32 – Averaged bubble interface velocity during vaporization vs. time for select trials at 1 bar and 2 bar pressure for unstable explosive boiling. Empirical curve fits for each trial are shown.

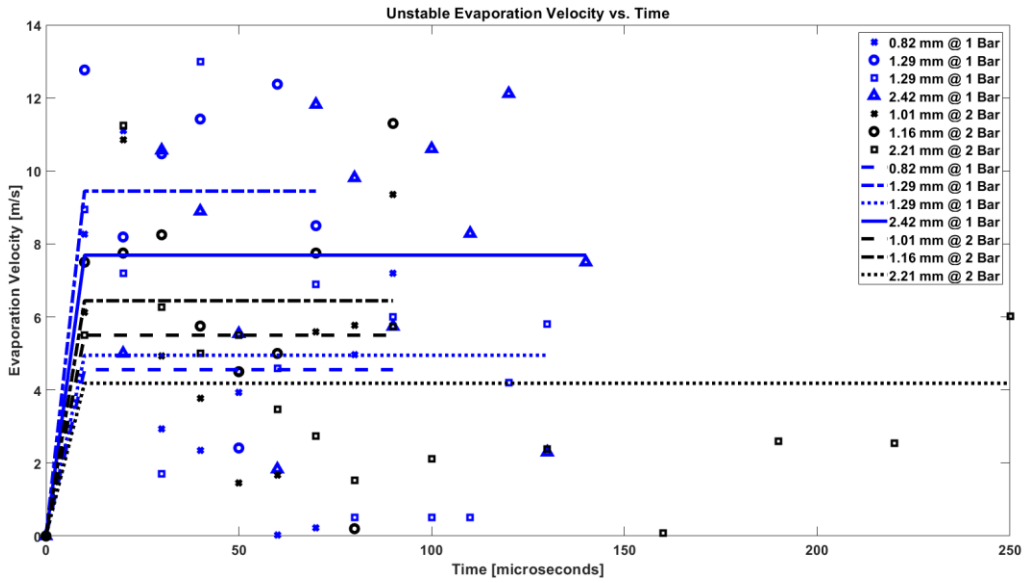

Fig. 3.33 – Averaged bubble evaporation velocity during vaporization vs. time for select trials at 1 bar and 2 bar pressure for unstable explosive boiling. Empirical curve fits for each trial are shown.

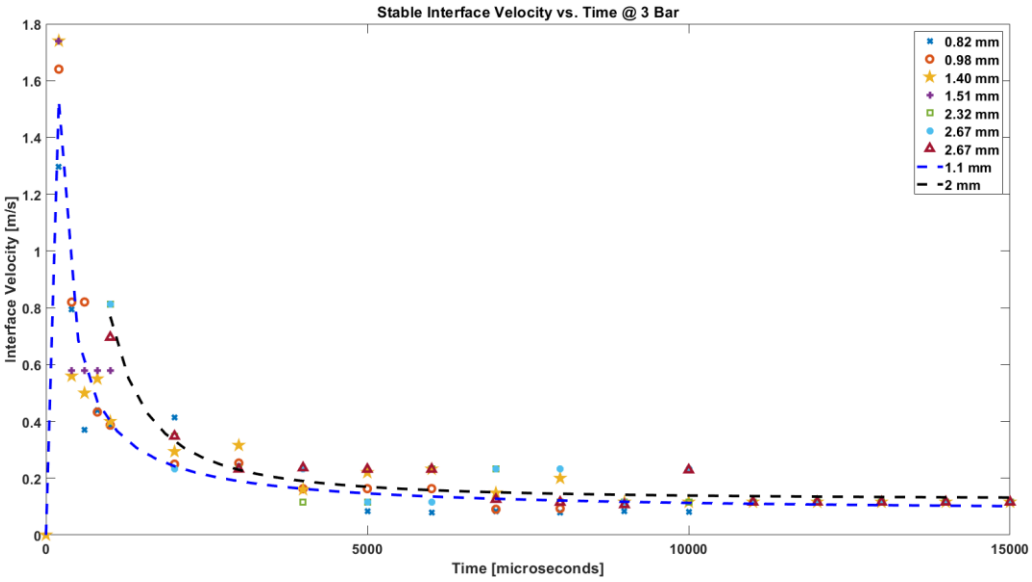

Fig. 3.34 – Interface velocity vs. time at 3 bar pressure for stable boiling. Empirical curve fits for droplets with initial diameter $D_0 \approx 1.1$ mm and 2 mm are shown. Initial rise of the $D_0 \approx 2$ mm curve purposely omitted.

At higher pressures, unstable explosive boiling appears to be suppressed, resulting in a smoother liquid-vapor interface, slower interface velocities, longer vaporization durations, and smaller peak normalized diameter growth. This suppression point for unstable boiling for diethyl

ether immersed in glycerol appears to be around 2.5 – 3 bar absolute pressure. The stable boiling interface velocity with respect to time is shown in Fig. 3.34 and Fig. 3.35 for 3 bar and 5 bar pressure absolute, respectively. The interface velocity data was captured and calculated in the same way as the interface velocity for the unstable boiling trials was in Fig. 3.25 and Fig. 3.30. The nucleation point was used as the origin and distances that were later differentiated to attain velocities were measured from there. Notably, the buoyant movement of the liquid droplet and vapor bubble played a larger role in impacting the measurements of the stable boiling trials with measurements consisting over a temporal range of 2 ms being affected and measurements over 4 ms being significantly affected. Actions were taken to negate these buoyancy effects such as measuring the distance the liquid droplet or vapor bubble moved vertically upwards due to buoyancy and taking it into account when measuring the distance the interface has traveled. The overall shape and trends of these stable interface velocity curves roughly resemble the unstable interface velocity curves, albeit with some caveats. In these stable interface velocity curves, upon nucleation the interface velocity rises quickly to a velocity maxima, similar to the unstable boiling cases, but at a lower magnitude. The interface velocity then decreases exponentially to a zero interface velocity asymptote. The interface velocity eventually approaches zero during off figure long-scale behavior between 25 ms to 40 ms after the beginning of nucleation. Similar to unstable boiling, a higher ambient pressure within the stable boiling regime correlates to a lower interface velocity. An increase from 3 bar to 5 bar pressure decreases peak interface velocity around 50% on average with long term interface velocity decreasing around 30%. Peak stable interface velocities, 3 – 5 bar, are over an order of magnitude slower than peak unstable interface velocities, 1 – 2 bar. Additionally, similar to unstable trials, initial diameter, D_0, does not appear to have an impact on interface velocity or vaporization duration. Best fit curves are provided for characteristic initial droplet diameters to better show the interface velocity development with time.

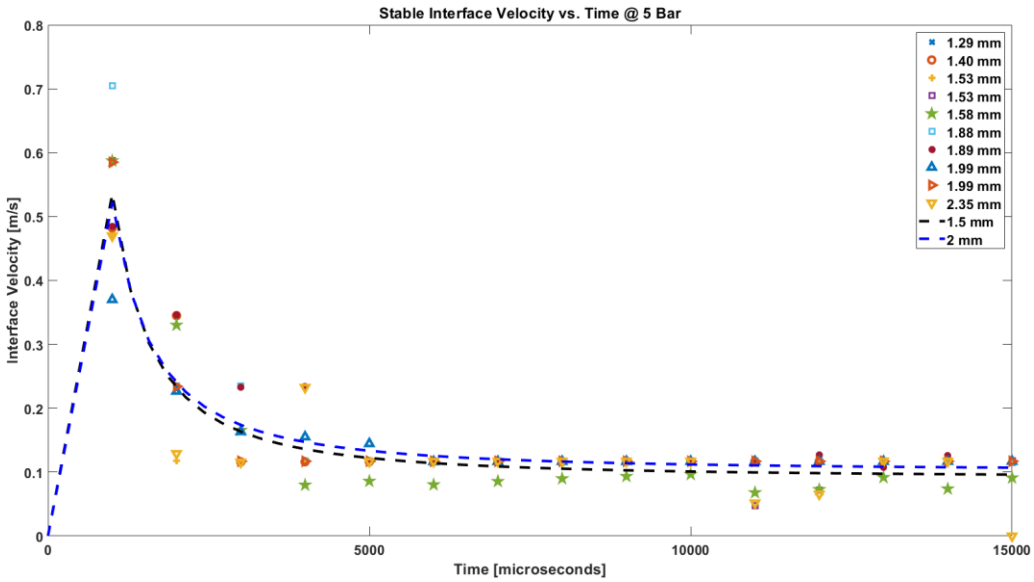

Fig. 3.35 – Interface velocity vs. time at 5 bar pressure for stable boiling. Empirical curve fits for droplets with initial diameter $D_0 \approx 1.5$ mm and 2 mm are shown.

The stable averaged bubble interface velocities vs. time during vaporization for selected trials at 3 bar and 5 bar absolute ambient pressures are shown in Fig. 3.36. The data are only measured during active vaporization but do not show the whole vaporization like previous unstable interface velocity plot shown in Fig. 3.32. Instead it only shows vaporization until buoyancy movement becomes significant, the first 4 ms. Similarly to the unstable averaged interface velocity, this stable averaged velocity is measured differently than the previously measured stable interface velocity presented above. These averaged interface velocity results are found from differentiating the diameter of the vapor bubble then dividing by two to average both directions of growth. Stable averaged bubble evaporation velocity vs. time during vaporization for selected trials at 3 bar and 5 bar absolute ambient pressures are shown in Fig. 3.37. Similarly to the unstable averaged evaporation velocity in Fig. 3.33, the stable evaporation velocity here takes into account and negates the growth of the bubble interface due to vapor expansion, allowing an examination of the relative velocity the evaporation interface consumes the droplet at. Best fit curves for the data at similar initial droplet diameters are plotted to allow better visualization of velocity trends. The interface velocity trends here reinforce what has been seen before. There does not appear to be a correlation between initial droplet diameter and interface velocity or evaporation velocity. However, there does appear to be a strong negative correlation between ambient pressure and interface velocity and evaporation velocity. From 3 bar to 5 bar for interface velocity, there appears to be an approximate 60% decrease in peak interface velocity and a 50% decrease in long term interface velocity. From 3 bar to 5 bar for evaporation velocity, there appears to be an approximate 55% decrease in peak evaporation velocity, but no decrease in long term evaporation velocity. Similarly for the unstable cases in Fig. 3.32 and Fig. 3.33, there is less decrease going from 3 bar to 5 bar in the evaporation velocity

than the interface velocity since the evaporation velocity controls for the vapor expansion in the vapor bubble which is affected by a pressure increase.

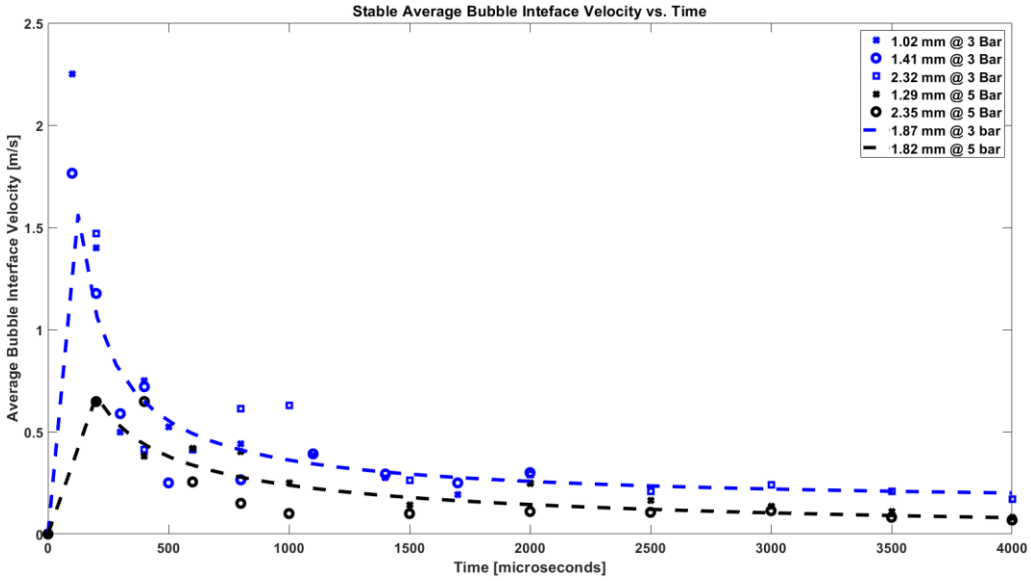

Fig. 3.36 – Averaged bubble interface velocity during vaporization vs. time for select trials at 3 bar and 5 bar pressure for stable boiling. Empirical curve fits for droplets with initial diameter $D_0 \approx$ 1.87 mm at 3 bar and 1.82 mm at 5 bar are shown.

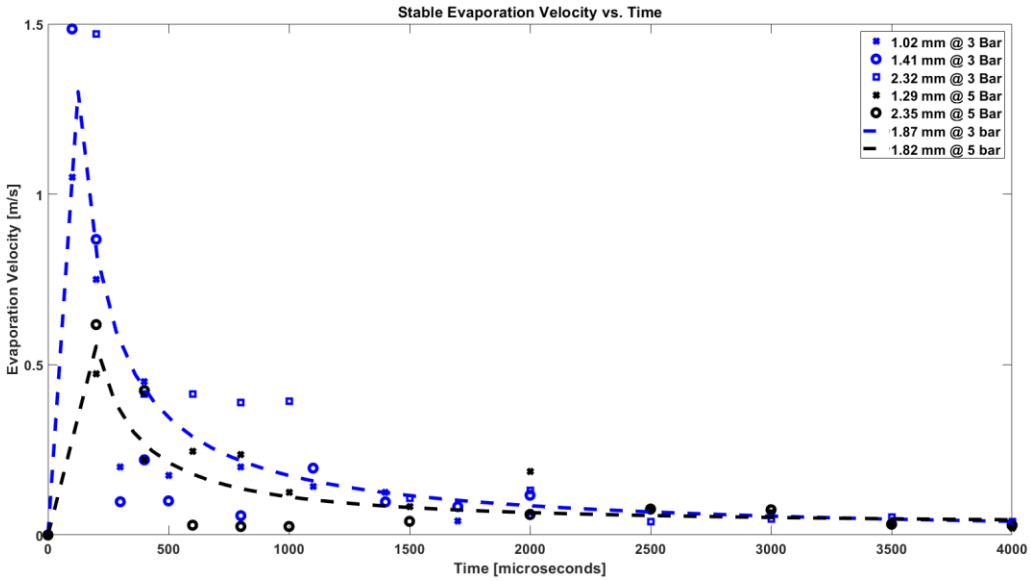

Fig. 3.37 – Averaged bubble evaporation velocity during vaporization vs. time for select trials at 3 bar and 5 bar pressure for stable boiling. Empirical curve fits for droplets with initial diameter D_0 ≈ 1.87 mm at 3 bar and 1.82 mm at 5 bar are shown.

The interfacial velocity with respect to time at constant initial diameter and varying pressure is shown in Fig. 3.38 for all experiment pressures. As stated previously, and shown again here, a higher ambient pressure correlates to lower interface velocity. Around 2.5 bar ambient pressure, the phenomenon shifts regimes from, at lower pressure, unstable explosive vaporization to, at higher pressures, stable vaporization. When pressure is increased past this transition point and boiling regime changes, the interface velocity drops significantly. Additionally, in the stable boiling regime, the interface velocity does not drop to zero as quickly as it does in the unstable explosive boiling regime, rather it asymptotes to a minimal baseline velocity before finally reaching zero off figure. From this figure a good sense of the discrepancy between unstable interface velocity, 1 bar and 2 bar, and stable interface velocity, 3 bar and 5 bar, can be attained. Fig. 3.39 is the same as Fig. 3.38, only plotted on log-log axes which allows better reading of the stratified data. Fig. 3.40 and Fig. 3.41 break up Fig. 3.38 for better readability as well. Fig. 3.40 consist of the unstable boiling interface velocities with two similar initial droplet diameter best fit curves for 1 bar and 2 bar. Notably here, phase II of the vaporization process is estimated using a simple nearly-linear fit as opposed to the rough estimate fit shown in Fig. 3.27 and Fig. 3.28 for simplicity. Fig. 3.41 consists of the stable boiling interface velocity data from Fig. 3.38 with two similar initial droplet diameter best fit curves for 3 bar and 5 bar.

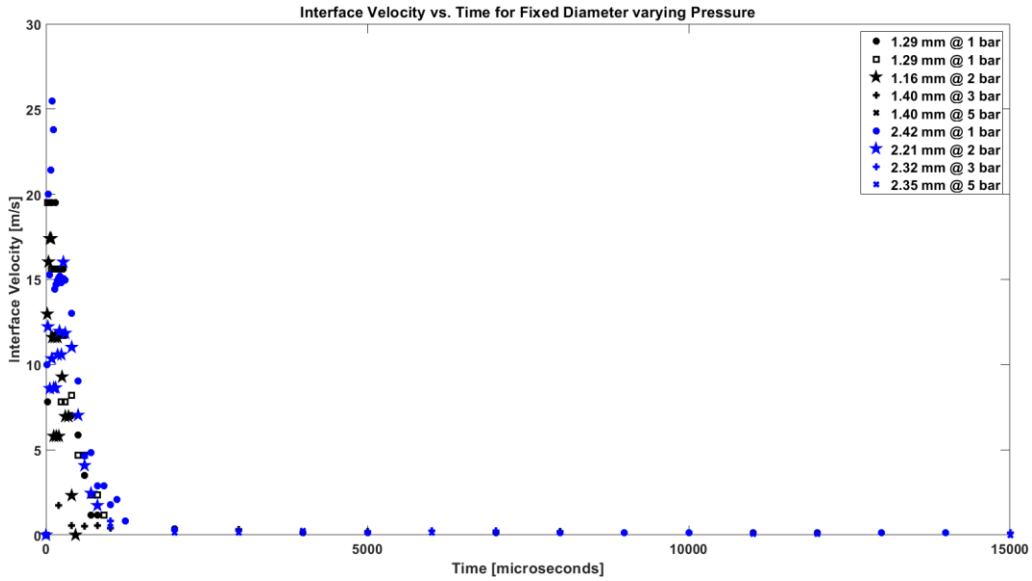

Fig. 3.38 – Interface velocity vs. time for D_0 = 1.25 mm and D_0 = 2.3 mm initial droplet size at 1, 2, 3, and 5 bar pressures.

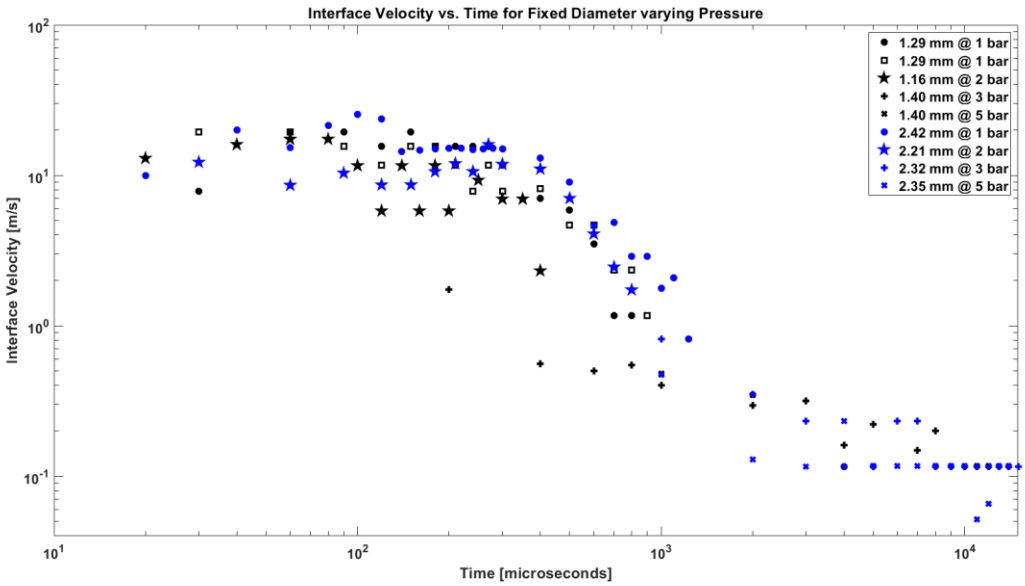

Fig. 3.39 – Interface velocity vs. time for D_0 = 1.25 mm and D_0 = 2.3 mm initial droplet size at 1, 2, 3, and 5 bar pressures. Log axes to compress data to allow better comparison.

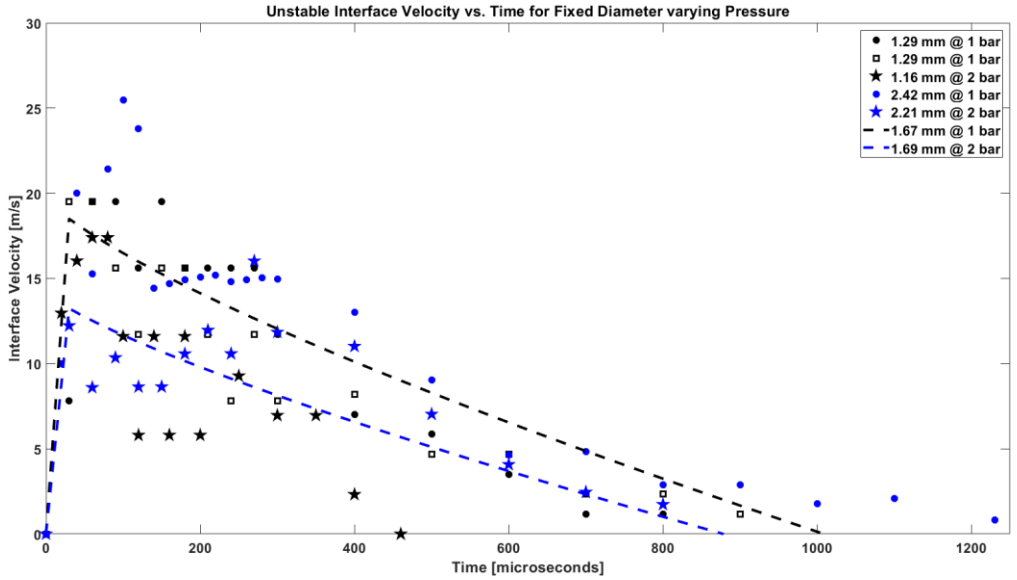

Fig. 3.40 – Unstable interface velocity vs. time for D_0 = 1.25 mm and D_0 = 2.3 mm initial droplet size at 1 and 2 bar pressures. Empirical curve fits for droplets with initial diameter $D_0 \approx$ 1.67 mm at 1 bar and 1.69 mm at 2 bar are shown.

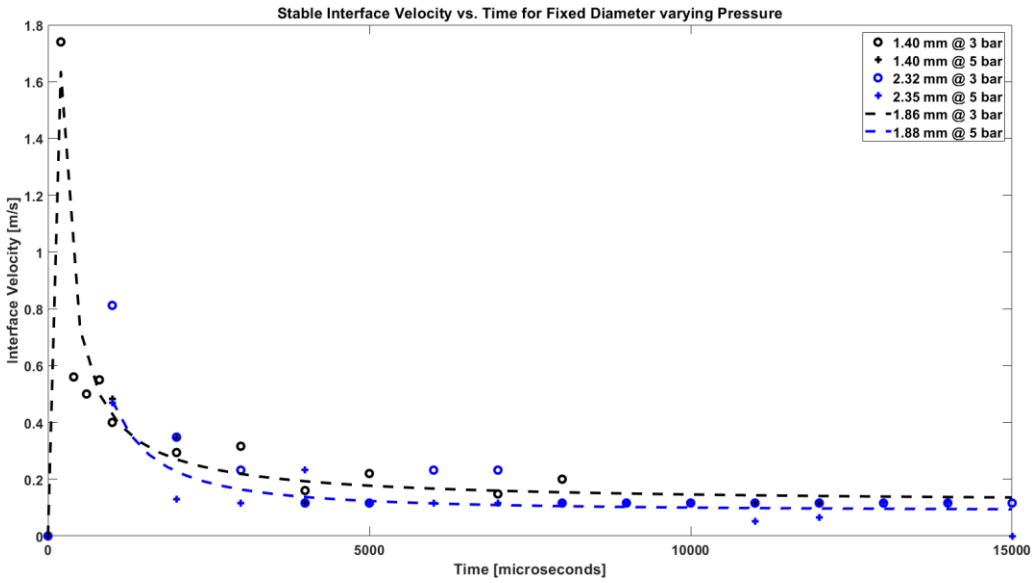

Fig. 3.41 – Stable interface velocity vs. time for D_0 = 1.25 mm and D_0 = 2.3 mm initial droplet size at 1, 2, 3, and 5 bar pressures. Empirical curve fits for droplets with initial diameter $D_0 \approx$ 1.67 mm at 1 bar and 1.69 mm at 2 bar are shown. Initial rise of the $D_0 \approx$ 1.88 mm curve at 5 bar pressure purposely omitted.

The averaged bubble interface velocity during vaporization vs initial droplet diameter is shown in Fig. 3.42 for both unstable and stable trials. Here, for each trial in Fig. 3.32 and Fig. 3.36, the interface velocity was averaged together and plotted. A linear regression line was then fitted to the data. The interface velocity axis is on a log scale due to the stratification of unstable and stable velocities, as a result the linear fits appear somewhat curved. By examining the slope of the best fit curves, how interface velocity changes with respect to initial droplet diameter can be deterimed. From the data there does not appear to be a strong correlation between interface velocity and initial droplet diameter, further supporting the findings above. Averaged bubble evaporation velocity during vaporization vs initial droplet diameter is plotted in Fig. 3.43. The data is averaged for each trial from Fig. 3.33 and Fig. 3.37. Similarly to Fig. 3.42, linear regression lines are fitted to the data. From these we can see that there is no correleation between initial droplet diameter and evapoation velocity, which also supports the findings earlier regarding evaporation velocity and initial droplet diameter.

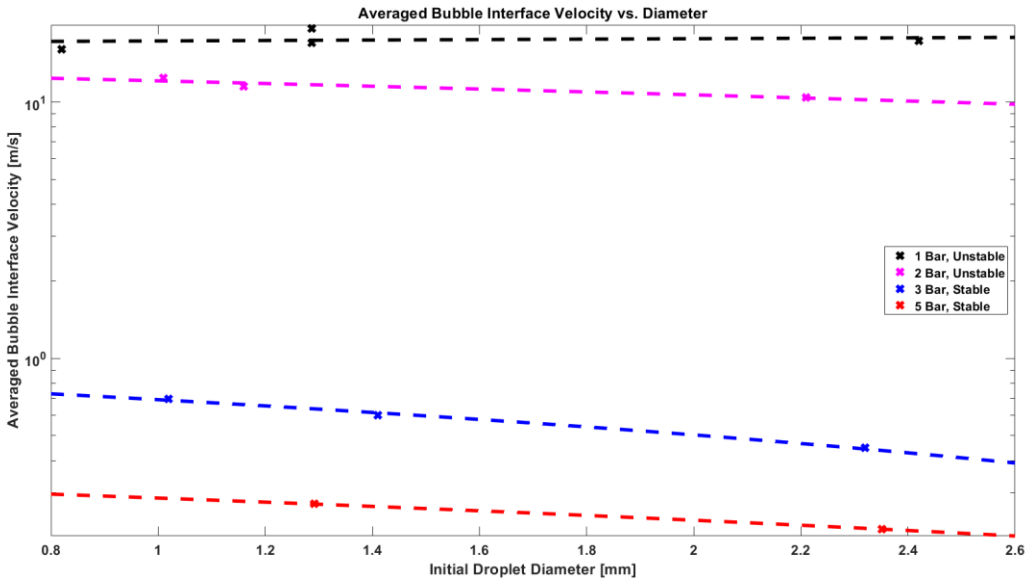

Fig. 3.42 – Averaged bubble interface velocity during vaporization vs. initial droplet diameter for select trials at 1, 2, 3, and 5 bar pressure.

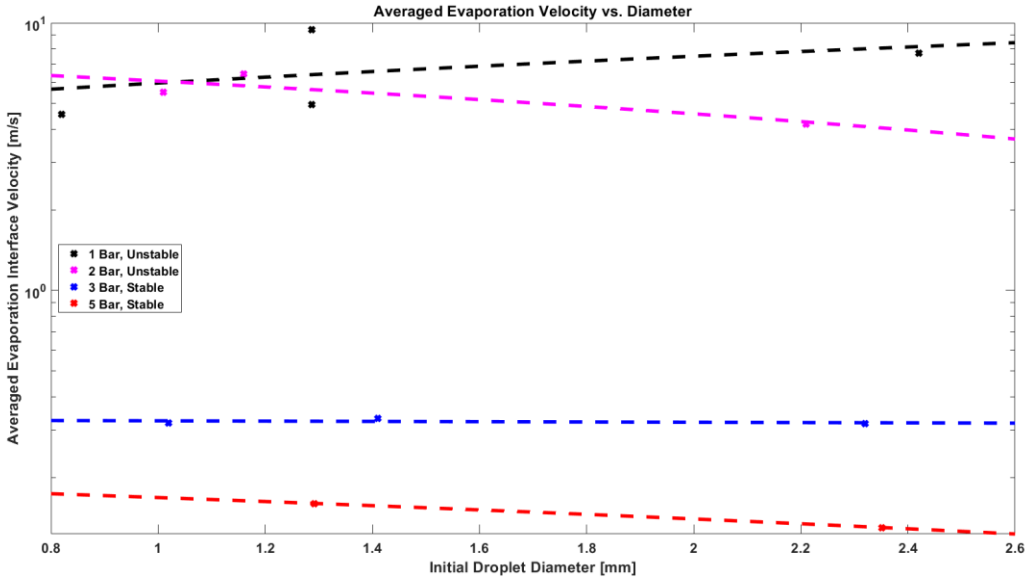

Fig. 3.43 – Averaged bubble evaporation velocity during vaporization vs. initial droplet diameter for select trials at 1, 2, 3, and 5 bar pressure.

3.4 Bubble Mass Transfer

3.4.1 Bubble Mass Flux

Mass flux and mass flow rate are closely related and give an idea of how much mass is being evaporated from liquid to vapor. In other words, mass flux and mass flow rate give an idea of how much mass is being transferred across the vapor bubble interface, or how much mass is flowing from the liquid droplet to the vapor bubble over a period of time. The mass flow rate is the total mass flow from the liquid droplet into the vapor bubble across the whole bubble surface per unit of time, whereas mass flux is the mass flow rate per unit area. Mass flux results will be discussed in this section, and mass flow rate in the following, but both with be defined here as one can be derived from the other and vice-versa, depending on the methodology.

Two separate methodologies were employed to calculate both mass flux and mass flow rate. This was done for two reasons. The first is to allow comparison with previous experimental results. The second is to provide upper and lower bounds for the results. The first methodology, method A, does not account for vapor expansion as the liquid evaporates into vapor when moving across the bubble interface and is therefore a more simplistic, less accurate estimation than method B. This leads to a higher estimation of the mass flux and mass flow rate making the method A calculations the upper bound of the results envelope. To find the mass flux of method A, first he mass flow rate must be found. Mass flow rate for method A, Q_A, is calculated using, $Q_A = \frac{V_{i+1}-V_i}{t_{i+1}-t_i}\rho_l$ where V_i is the vapor bubble volume at time t_i, and ρ_l is the density of the liquid diethyl ether droplet. From this mass flow rate equation, the mass flux for method A, q_A, can be found using, $q_A = \frac{Q_A}{(A_{s,i}+A_{s,i+1})/2} = \frac{Q_A}{\bar{A}_{s,i\to i+1}}$ where $A_{s,i}$ is the vapor bubble surface area at t_i, and $\bar{A}_{s,i\to i+1}$ is the average vapor bubble surface area of $A_{s,i}$ and $A_{s,i+1}$. The second methodology, method B, does account for vapor expansion and is believed to be a more accurate model for the mass flux and mass flow rate during evaporation. Method B acts as the lower bound of the results envelope. Mass flux rate for method B, q_B, can be calculated using, $q_B = \frac{(v_b-v_d)}{2}\rho_l = \frac{v_e}{2}\rho_l = \bar{v}_e\rho_l$, where v_b is the total vapor bubble interface velocity, v_d is the total liquid droplet interface velocity, v_e is the total vapor bubble evaporation velocity, and $\bar{v}_e$ is the averaged vapor bubble evaporation velocity. From this mass flux equation, the mass flow rate for method B, Q_B, can be found using, $Q_B = q_B\frac{A_{s,i}+A_{s,i+1}}{2} = q_B\bar{A}_{s,i\to i+1}$. Since the mass flux in method A and method B utilize variables like total bubble surface area, bubble volume, and total bubble and droplet interface velocity, the mass fluxes presented here are the average mass flux across the whole bubble surface. Peak mass fluxes in local areas of the bubble interface may exceed these mass fluxes, especially in the conservative case of method B. The unstable mass flux rates are accurate to ±1250 kg/s.m^2 and stable mass flux rates are accurate to ±125 kg/s.m^2.

The vapor bubble mass flux during vaporization for method A is shown in Fig. 3.44 and for method B in Fig. 3.45 for selected unstable boiling trials at 1 bar and 2 bar pressure absolute. There does not appear to be a strong correlation between mass flux in method A or method B

and time, and knowing that mass flux is based off interface and evaporation velocities, a similar reasoning for the best fit lines for each trial can be used – an initial rapid rise followed by a flat line at the average reflecting that interface velocity is mostly constant during unstable vaporization. As a result, similar trends are seen in the mass flux plots for method A and method B as the plots for averaged interface velocity and averaged evaporation velocity for unstable boiling during vaporization in Fig. 3.32 and Fig. 3.33. There does not appear to be a strong correlation between unstable mass flux for method A or method B and initial droplet diameter. There does appear to be a strong correlation between unstable mass flux for method A and method B and ambient pressure, with an increase in pressure causing a decrease in mass flux. This correlation appears less pronounced in the mass flux for method B, which is a similar trend in the averaged evaporation velocity in Fig. 3.33. By accounting for vapor expansion, pressure correlates less strongly with mass flux for a similar reasoning given for Fig. 3.33. Average mass flux rates for method A appear significantly higher than method B due to not accounting for vapor expansion. For 1 bar, method A, mass flux is approximately 130% greater than method B. For 2 bar, mass flux is approximately 100% greater than method B. This significant variance can be attributed to not accounting for vapor expansion in method A, which plays a large role in vapor bubble growth. In comparison to past research, for a test fluid of butane – not diethyl ether – at atmospheric pressure, Shepard and Sturtevant found an average unstable mass flux of around 4000 kg/s.m^2 and a peak of 5000 kg/s.m^2 [3, 20]. Similarly, Frost estimated a jet mass flux during stable-to-unstable explosive boiling of 3500 kg/s.m^2, a slightly different phenomenon, but similar order of magnitude result [4, 21]. This reinforces the belief that method B provides the more accurate estimation of the mass flux.

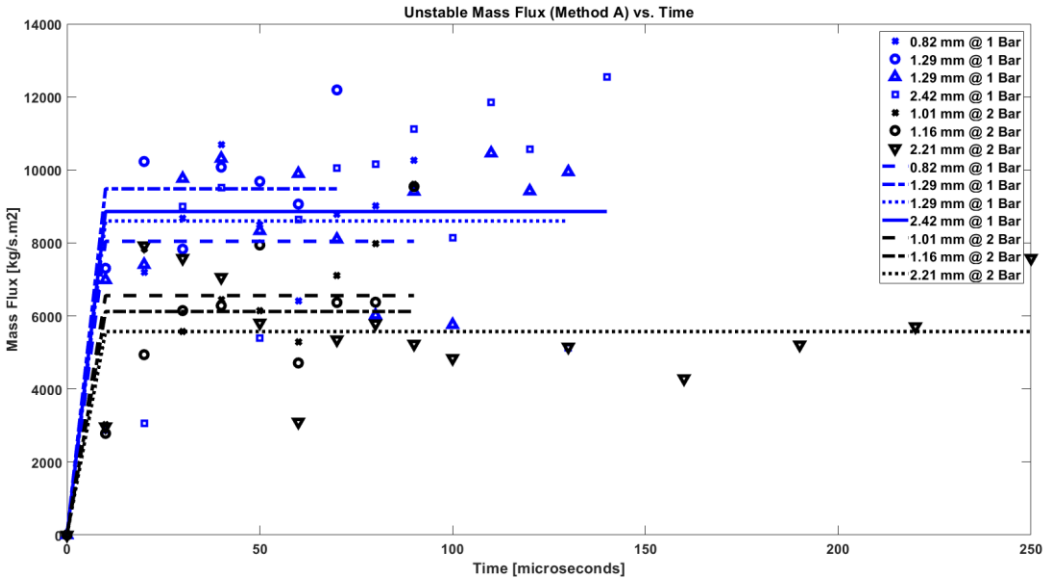

Fig. 3.44 – Vapor bubble mass flux (method A – upper bound) during vaporization vs. time for select trials at 1 bar and 2 bar pressure for unstable explosive boiling. Empirical curve fits for each trial are shown.

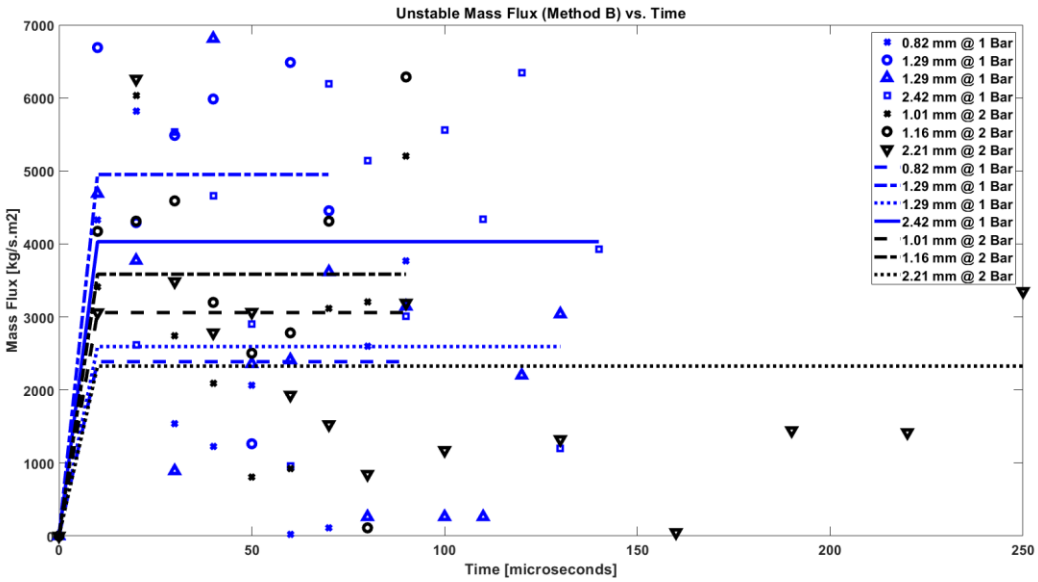

Fig. 3.45 – Bubble mass flux (method B – lower bound) during vaporization vs. time for select trials at 1 bar and 2 bar pressure for unstable explosive boiling. Empirical curve fits for each trial are shown.

The vapor bubble mass flux during vaporization for method A is shown in Fig. 3.46 and for method B in Fig. 3.47 for stable boiling at 3 bar and 5 bar pressure absolute. As previously stated, trends in the mass flux reflect trends in the stable averaged interface velocity and stable averaged evaporation velocity during vaporization shown in Fig. 3.36 and Fig. 3.37, respectively. Upon nucleation, the mass flux rises rapidly, similar to the unstable case, but when the unstable case then reaches a steady state, in the stable case, the mass flux quickly decreases exponentially, slowly moving towards what appears to be a linear decrease before finally reach zero off plot when vaporization completes. There does not appear to be a correlation between initial droplet diameter and mass flux rate in either method A or method B for either 3 bar or 5 bar pressure. There does appear to be a correlation to ambient pressure, as seen before, with an increase in pressure from 3 bar to 5 bar corresponding to a drop in mass flux, although, in method B, long term mass flux behavior seems unaffected by the pressure – similar to averaged stable evaporation velocity in Fig. 3.37 – and due to the same reasoning that when vapor expansion is accounted for, pressure plays a less significant role in vapor bubble growth. Interestingly, there is not as strong of a difference between method A and method B in the stable results as the unstable results, and for some parameters, method B is actually produces larger results. At 3 bar, method A peak mass flux is approximately 10% less than the method B peak mass flux, counter to previous results. However, for long term mass flux at 3 bar, method A is approximately 260% larger than method B, significantly higher. Accounting for the vapor expansion appears to have more impact on long term behavior, which seems to make sense since at long term, the bubble has had more time to expand and decompress, causing vapor expansion to play a larger role here. At 5 bar, method A peak mass flux is approximately 14% lower than the method B peak mass flux,

similar to the 3 bar case. At 5 bar, method A long term mass flux is 67% higher than the method B long term mass flux. Comparing unstable to stable results by method, for method A, peak stable mass flux is approximately 93% lower than average unstable mass flux. For long term stable mass flux for method A, mass flux is approximately 99% lower than average unstable mass flux, significantly lower. For method B, peak stable mass flux is approximately 83% lower than average unstable mass flux. For long term stable mass flux for method B, mass flux is approximately 99% lower than average unstable mass flux, similar to method A.

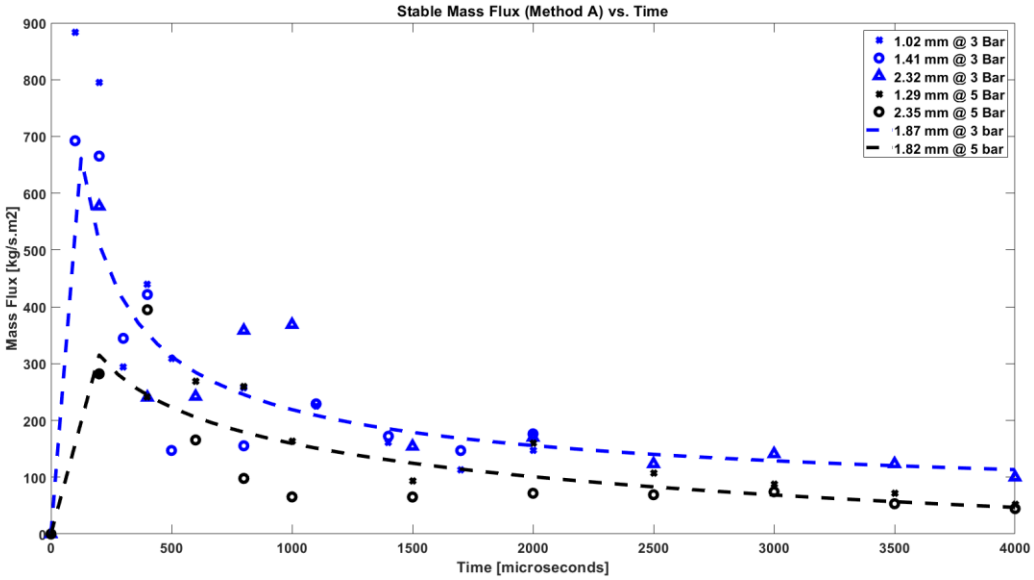

Fig. 3.46 – Bubble mass flux (method A – upper bound) during vaporization vs. time for select trials at 3 bar and 5 bar pressure for stable boiling. Empirical curve fits for droplets with initial diameter $D_0 \approx 1.87$ mm at 3 bar and 1.82 mm at 5 bar are shown.

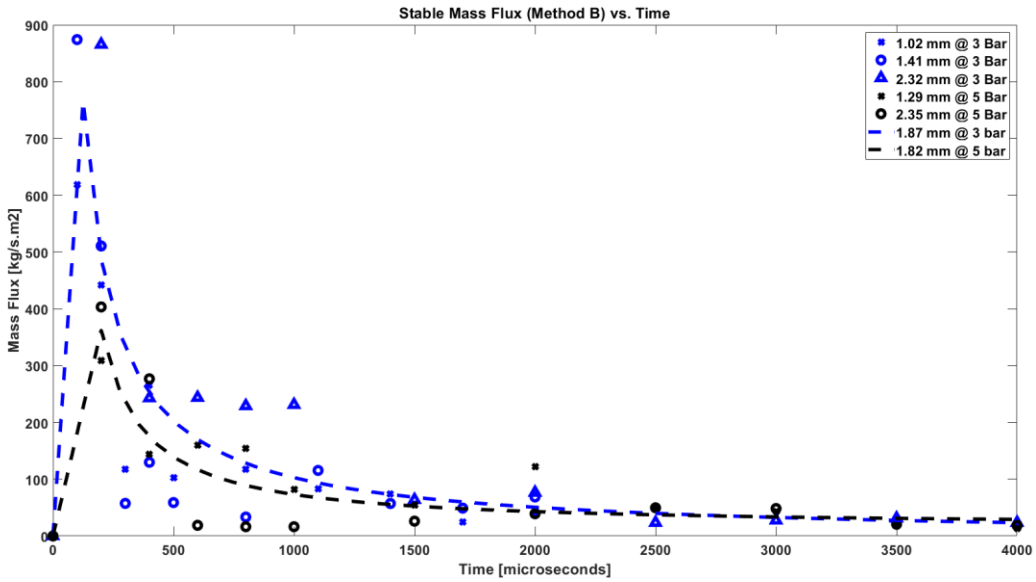

Fig. 3.47 – Bubble mass flux (method B – lower bound) during vaporization vs. time for select trials at 3 bar and 5 bar pressure for stable boiling. Empirical curve fits for droplets with initial diameter $D_0 \approx 1.87$ mm at 3 bar and 1.82 mm at 5 bar are shown.

The averaged bubble mass flux during vaporization vs initial droplet diameter is shown in Fig. 3.48 for method A and shown in Fig. 3.49 for method B for both unstable and stable trials. Similar to the averaged interface velocity and evaporation velocity plots in Fig. 3.42 and Fig. 3.43, the mass flux was averaged together for each trial and then plotted based on that trial's initial droplet diameter, grouped by ambient pressure, in an attempt to examine in detail if initial droplet diameter plays a role on average mass flux. Also, similarly to the averaged interface and evaporation velocity plots, a linear best fit line was fitted to each pressure, but appears curved due to the mass flux being plotted on a log scale. From these figures, there does not appear to be a strong correlation between initial droplet diameter and averaged mass flux for either method A or method B. However, there does appear to be a correlation between ambient pressure and averaged mass flux, reinforcing what has been seen before, that an increase in ambient pressure corresponds to a decrease in averaged mass flux for either method A or method B.

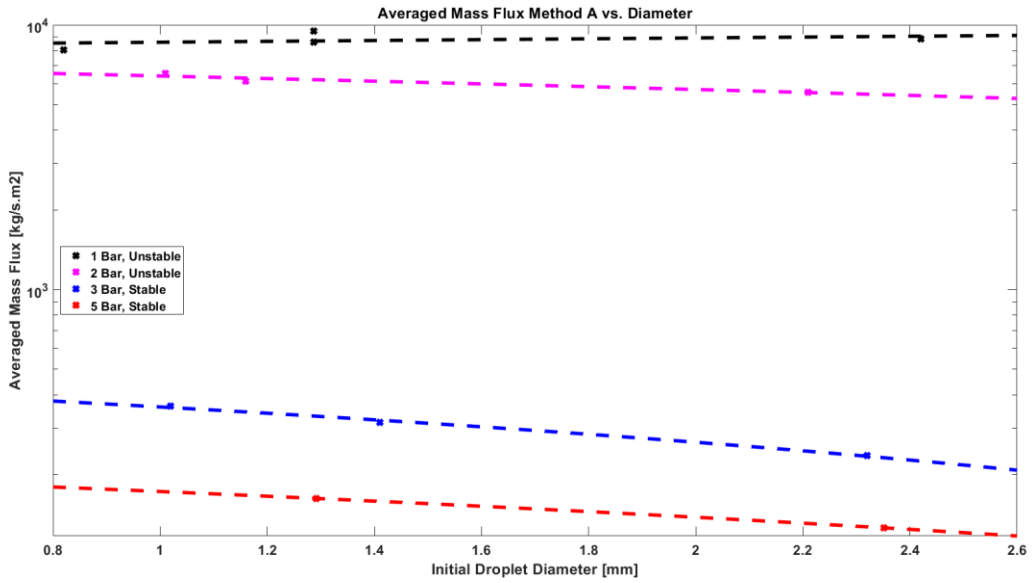

Fig. 3.48 – Averaged bubble mass flux (method A – upper bound) during vaporization vs. initial droplet diameter for select trials at 1, 2, 3, and 5 bar pressure.

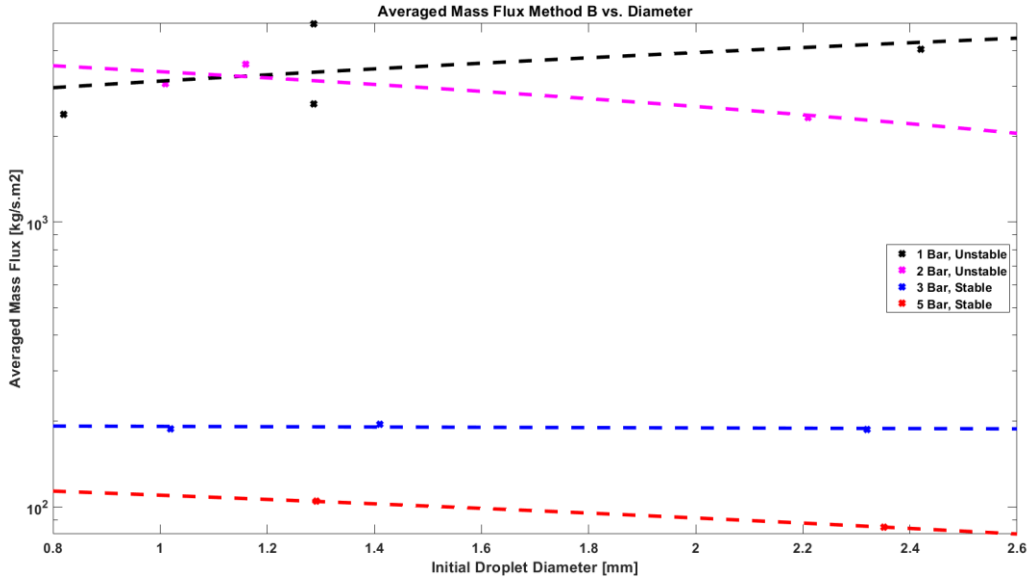

Fig. 3.49 – Averaged bubble mass flux (method B – lower bound) during vaporization vs. initial droplet diameter for select trials at 1, 2, 3, and 5 bar pressure.

3.4.2 Bubble Mass Flow Rate

The unstable mass flow rate during vaporization for method A and for method B for selected trials at 1 bar and 2 bar are shown in Fig. 3.50 and Fig. 3.51, respectively. The unstable mass flow rates are accurate to ±0.002 kg/s and stable mass flow rates are accurate to ±0.0002

kg/s. Two best fit curves have been plotted on Fig. 3.51 where the data trend is less clear. As vaporization progresses, the vapor bubble gets larger, during which the bubble interface surface area increases. This increased interface surface area can in turn allow a larger mass flow rate to the vapor bubble as the mass flux is roughly fixed and dependent of surface area. As the vapor bubble gets larger, a larger mass flow rate can pass to the bubble, this is proportional to the volume of the bubble, or proportional to the cube of the vapor bubble diameter, $Q \propto D^3$. The mass flow rate in Fig. 3.50 and Fig. 3.51 reflects this cubic relationship since the unstable diameter is linear during vaporization as seen in Fig. 3.13. There does not appear to be a strong relationship between initial droplet diameter and mass flow rate. However, there does appear to be a strong relationship between ambient pressure and mass flow rate with an increase in ambient pressure corresponding to a decrease in mass flow rate for both method A and method B. In addition, there is a general decrease in mass flow rate going from method A to method B due to not accounting for the vapor expansion in method A.

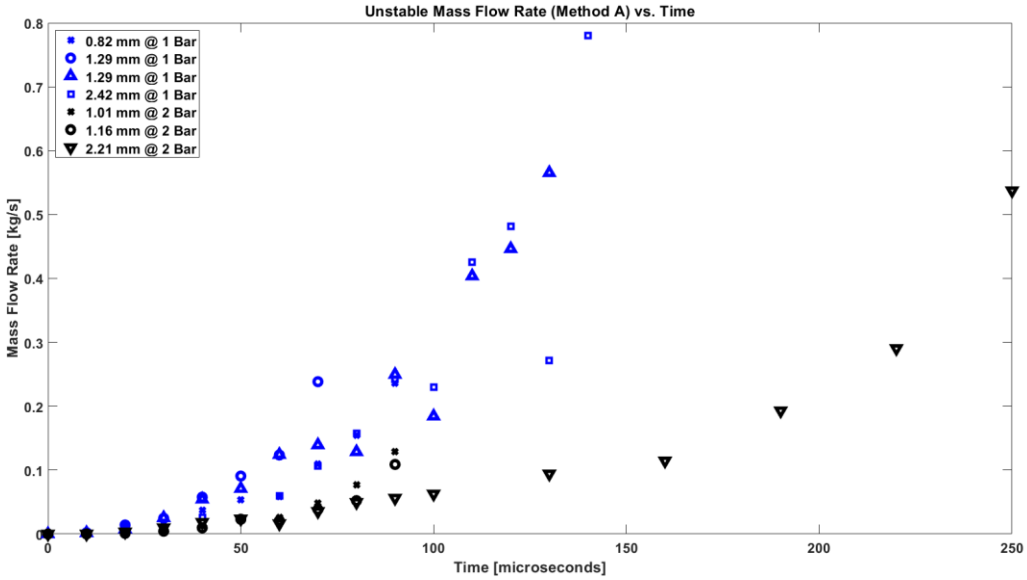

Fig. 3.50 – Bubble mass flow rate (method A – upper bound) during vaporization vs. time for select trials at 1 bar and 2 bar pressure for unstable explosive boiling.

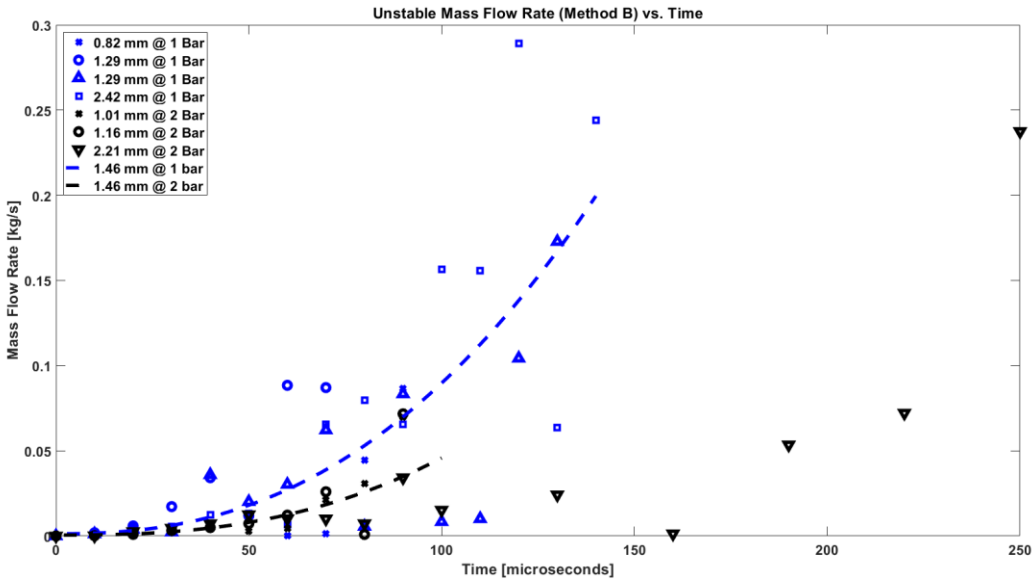

Fig. 3.51 – Bubble mass flow rate (method B – lower bound) during vaporization vs. time for select trials at 1 bar and 2 bar pressure for unstable explosive boiling. Empirical curve fits for droplets with initial diameter $D_0 \approx 1.46$ mm at 1 bar and 1.46 mm at 2 bar are shown.

The stable mass flow rate during vaporization for method A and method B at 3 bar and 5 bar pressure absolute is shown in Fig. 3.52 and Fig. 3.53. The behavior of the stable mass flow rate as vaporization progresses is quite different than the shape of the unstable mass flow rate due to the nature of the vapor bubble diameter growth. Unstable boiling bubble diameter grows linearly, whereas stable bubble diameter grows as a power function, $y = ax^b$, with the exponent, b, between 0 and 1. The behavior of the vapor bubble growth propagates to the mass flow rate as shown by the equations shown before. The behavior of the stable mass flow rate resembles a power function with an exponent between 0 and 1 for both method A and method B. As stated before, the main difference in the methodology between method A and method B is that method B accounts for the vapor expansion of droplet liquid boiling to vapor in the growth of the vapor bubble. By not accounting for this vapor expansion, the method A mass flow rates are approximately 250% of the method B mass flow rates in the 3 bar trials and 200% in the 5 bar trials. Additionally, there is a propensity for the final few points in the 2.32 mm 3 bar mass flow rate data for method A to be over inflated due to not accounting for the vapor expansion. As stated before, as the vapor bubble diameter increases, the effects of the vapor expansion become more pronounced, as well as for lower pressures, these vapor expansion effects are stronger. When the vapor expansion is not controlled for, the final points in this trial in question, which is also at the lower range of pressures displayed in this figure, become inflated disproportionately to the rest of the data in the trial. Trends in the stable mass flow rate appear in line with the previously seen trends. There does not appear to be a strong correlation between initial droplet diameter and mass flow rate. There does appear to be strong a negative correlation

between pressure and mass flow rate, with those effects being less pronounced in the method B mass flow rate in Fig. 3.53 due to reasons mentioned earlier.

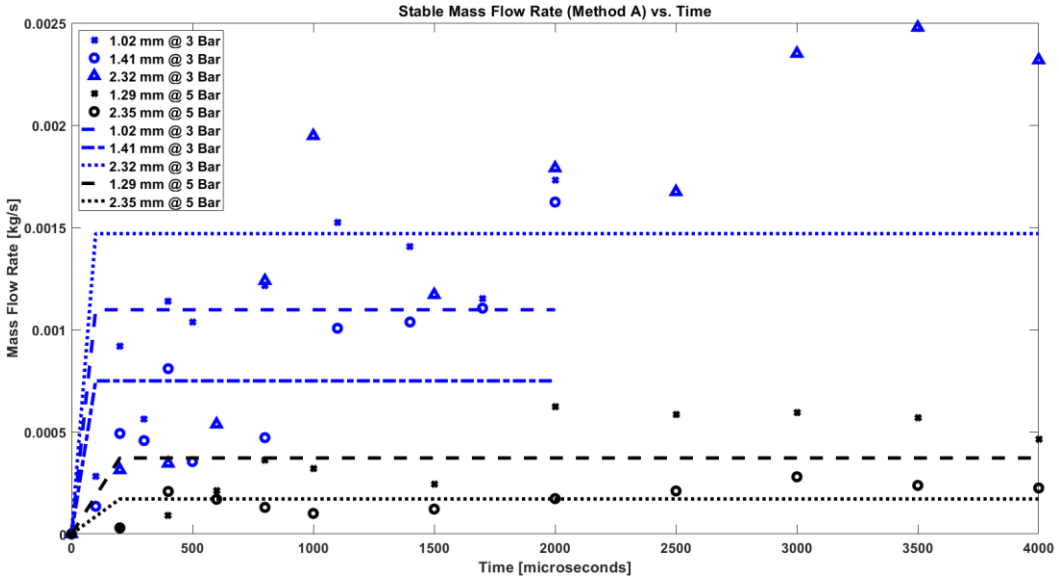

Fig. 3.52 – Bubble mass flow rate (method A – upper bound) during vaporization vs. time for select trials at 3 bar and 5 bar pressure for stable boiling. Empirical averages for each trial are shown.

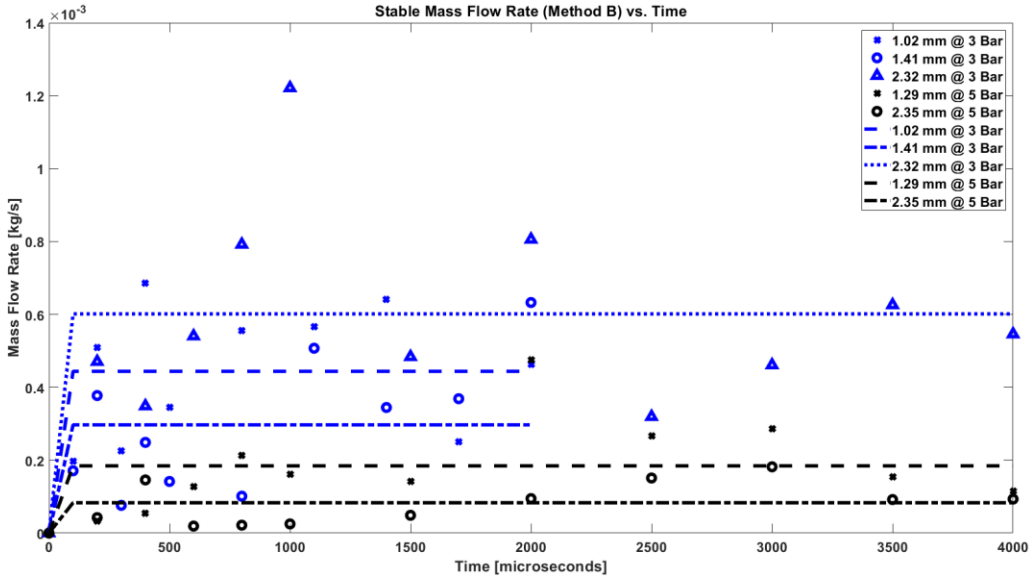

Fig. 3.53 – Bubble mass flow rate (method B – lower bound) during vaporization vs. time for select trials at 3 bar and 5 bar pressure for stable boiling. Empirical curve fits for each trial are shown.

The averaged bubble mass flow rate during vaporization vs the initial droplet diameter is shown in Fig. 3.54 for method A and shown in Fig. 3.55 for method B for both unstable and stable trials. To attain these plots all the mass flow rates are averaged together for each individual trial,

plotted based on their initial droplet diameter, and grouped by ambient pressure. Linear regression lines are plotted for each pressure group to examine if there is a correlation between initial droplet diameter and mass flow rate, however there does not appear to be a strong correlation for either method A or method B, which supports previous findings. There does appear to be a strong inverse correlation between ambient pressure and averaged mass flow rate for both method A and method B, which reinforces what was found earlier. Additionally, these figures support method A being a higher estimate for the mass flow rate than method B. Plotting 1 bar, 2 bar, 3 bar, and 5 bar trials together on the same plot gives a good sense of the vast difference between unstable and stable boiling mass flow rates, as well as how increasing the pressure while maintaining the same boiling regime influences the mass flux in relation to this difference. Averaged mass flow rate was plotted on a log axis due to the order of magnitude disparity between the unstable and stable trials. Due to this, the linear regression lines appear curved.

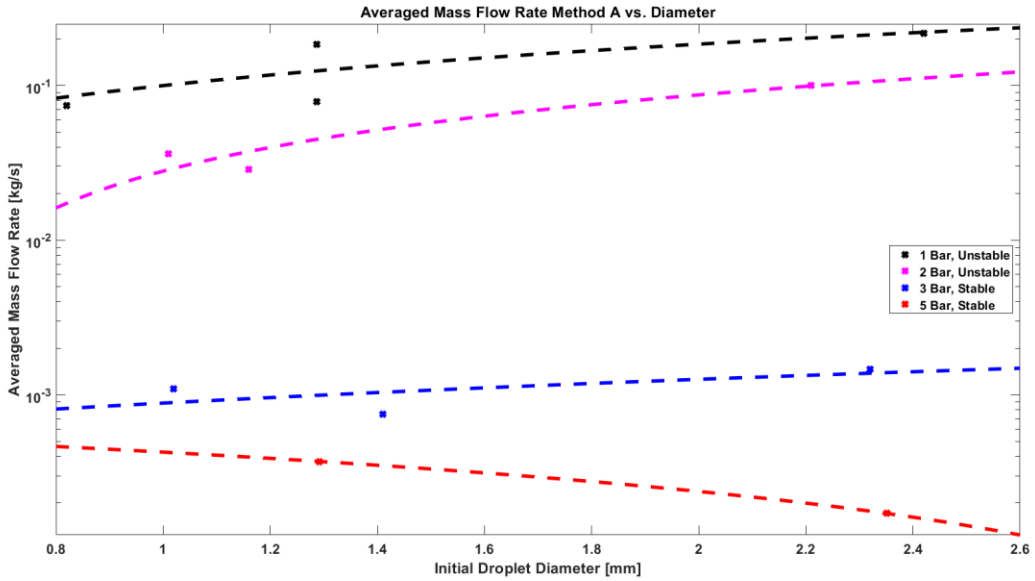

Fig. 3.54 – Averaged bubble mass flow rate (method A – upper bound) during vaporization vs. initial droplet diameter for select trials at 1, 2, 3, and 5 bar pressure.

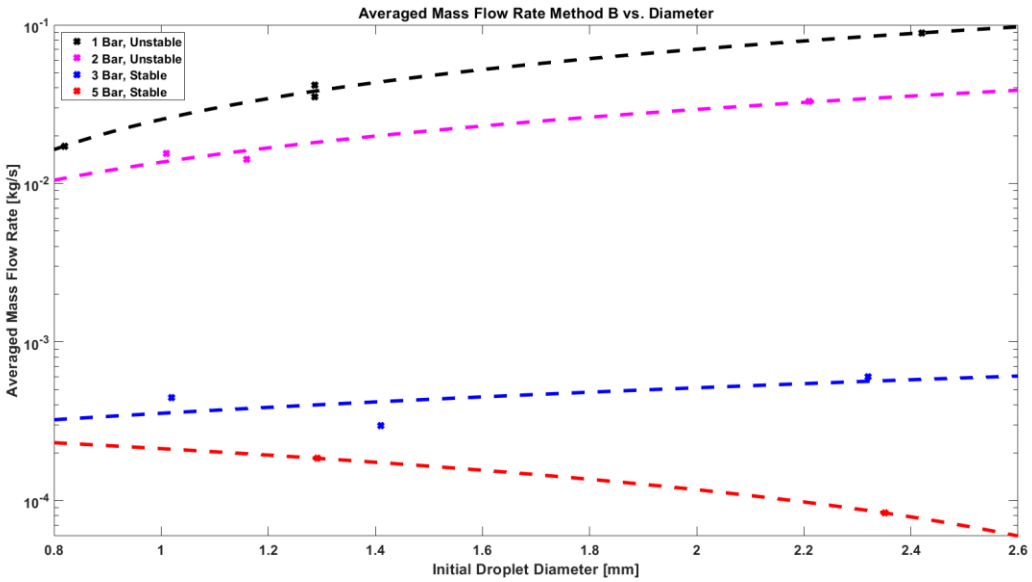

Fig. 3.55 – Averaged bubble mass flow rate (method B – lower bound) during vaporization vs. initial droplet diameter for select trials at 1, 2, 3, and 5 bar pressure.

3.5 Bubble Interface Instability Wavelength

After the liquid droplet is completely consumed by the unstable explosive boiling process, the resulting bubble is observed to oscillate at a high frequency before dampening out. This does not occur for stable boiling. During these oscillations, Rayleigh-Taylor instabilities form on the bubble surface, increasing in number with subsequent oscillations before recombining and flattening out as the oscillations dampen out. These instabilities can be quantified with a mean wavelength which equates to the average instability size. The evolution of this mean instability wavelength at the vapor-liquid interface at fixed ambient pressure and varying initial droplet diameter for unstable explosive boiling is shown in Fig. 3.57 and Fig. 3.58. All wavelength measured here are measured when the bubble is at the maximum diameter for the oscillation. For instance, at oscillation number 3, the wavelengths were measured at the third bubble maximum during oscillations.

These Rayleigh-Taylor instabilities manifest on the interface as a macro-scale protrusions that that can be observed visually. These are not to be confused with the Landau-Darrieus-like micro-scale surface roughness on the evaporating interface discussed before and shown in Fig. 3.3. These large-scale surface instabilities can be quantified by measuring their average wavelength, or the average number of wave crests taken over the visual circumference of the bubble. This average wavelength is approximated here by dividing the visual circumference of the bubble by the number of protrusions along that circumference as shown in Fig. 3.56. The circumference of the bubble in the focal plane is approximated using a best fit ellipse calculated from the vapor bubble height and width. This is one assumption made that can lead to error, as

the oscillating bubble at maximum is oftentimes not a perfect ellipse, especially at later oscillations. The wavelength is estimated to be accurate to ±0.25 mm.

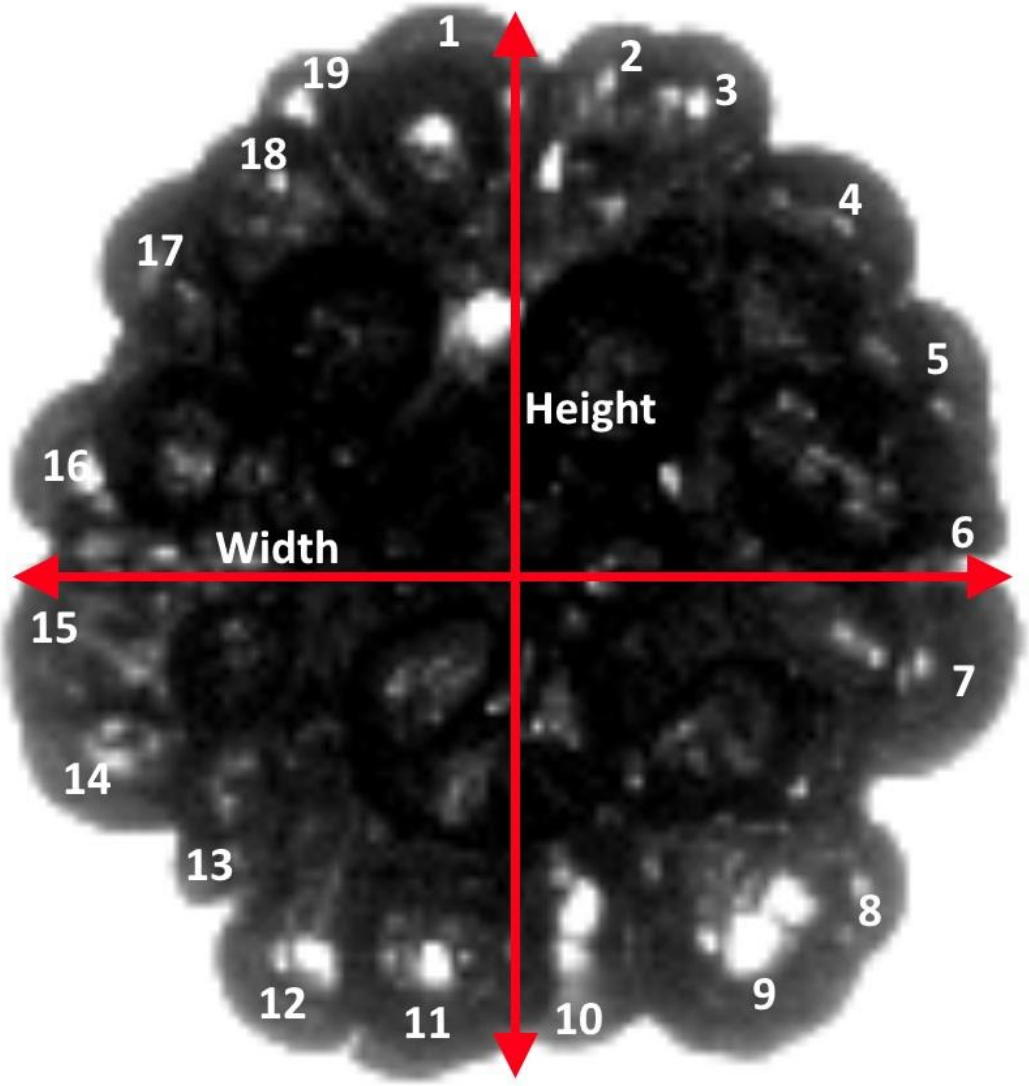

Fig. 3.56 – Average Rayleigh-Taylor wavelength measurement. The Rayleigh-Taylor instability protrusions are numbered and counted. The number of instabilities are then divided by the vapor bubble circumference which is approximated from a best fit ellipse calculated from the height and width of the vapor bubble to attain the average wavelength.

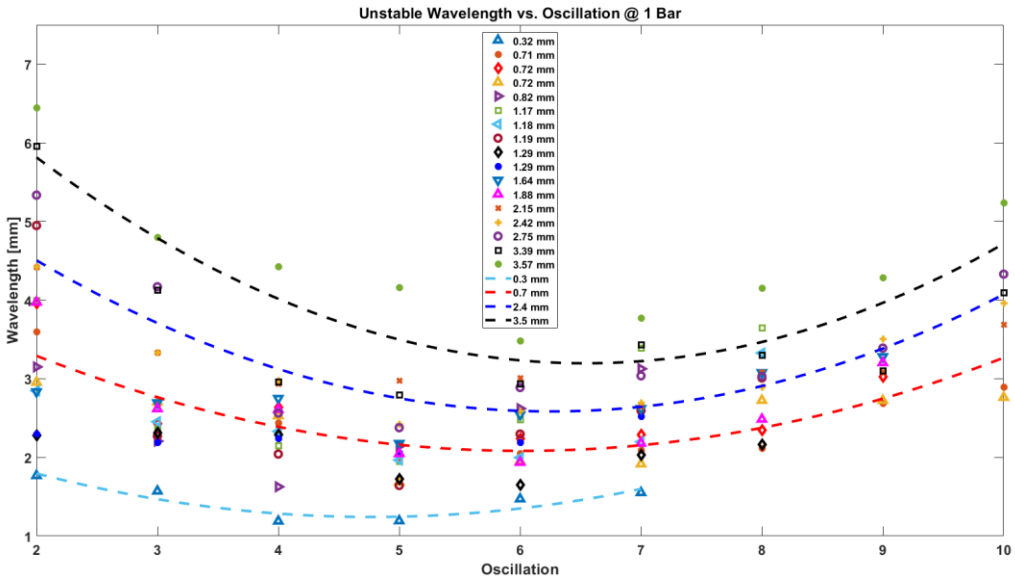

Fig. 3.57 – Wavelength vs. time at 1 bar pressure for unstable explosive boiling. Empirical curve fits for droplets with initial diameter $D_0 \approx$ 0.3 mm, 0.7 mm, 2.4 mm, and 3.5 mm shown.

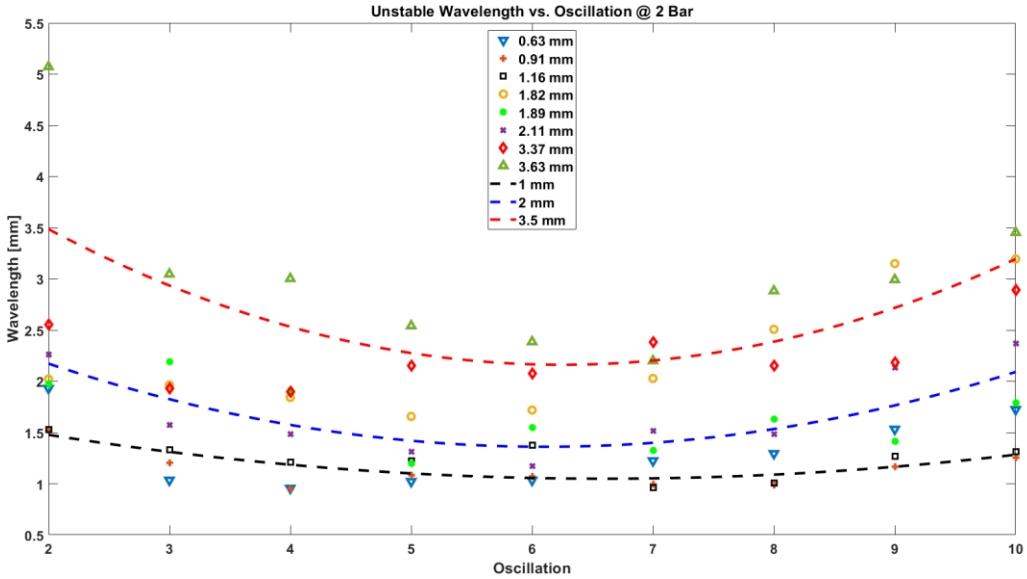

Fig. 3.58 – Wavelength vs. time at 2 bar pressure for unstable explosive boiling. Empirical curve fits for droplets with initial diameter $D_0 \approx$ 1 mm, 2 mm, and 3.5 mm shown.

During unstable, explosive vaporization of the droplet, thermal energy is converted to kinetic energy within the droplet as the interface gains velocity and momentum. This interface gains kinetic energy due to propagating across the liquid droplet as the droplet is vaporized, but also due to the vapor expansion of the liquid being boiled into vapor. After the droplet is completely vaporized by the vapor bubble, the bubble interface is carried past the natural equilibrium diameter of the bubble where the internal bubble pressure and the ambient pressure

host fluid pressure are equal. Due to the pressure imbalance, the bubble growth and interface velocity soon slows, before coming to a halt at the maximum bubble diameter. The bubble then start to contract, gaining kinetic energy from the pressure imbalance, and again moves past the equilibrium diameter until the internal bubble pressure gain due to compression slows and stops the interface movement before reversing it again. This oscillation repeats until energy is lost due to thermal, viscous, and acoustic radiation damping, at which point the bubble interface settles at the equilibrium diameter [3, 28]. For stable boiling, oscillations do not occur as the interface velocity does not appear to be large enough to overshoot the equilibrium point.

The first oscillation is the time from nucleation, to the first maximum diameter, to the first minimum diameter, then back to the equilibrium diameter. During the first oscillation, Rayleigh-Taylor instabilities at the liquid-vapor bubble interface do not normally become prevalent until the first minimum diameter is reached. The interface at the maximum diameter during the first oscillation typically is quite smooth, with the interfacial instabilities first appearing at the subsequent minimum bubble diameter contraction, or trough in the oscillation cycle. This is why oscillation 1 is not shown in Figs. 3.57, 3.58 and 3.59, there are no instabilities at the maximum diameter of the first oscillation. These Rayleigh-Taylor instabilities are caused by a less-dense fluid, in this case diethyl ether vapor, pushing against a more dense fluid, in this case the glycerol host liquid as well as large vapor bubble interfacial accelerations. During subsequent oscillations, the Rayleigh-Taylor instabilities become more dominant as the instabilities compound upon each other. Instabilities become most evident after an oscillation maximum or minimum diameter when the bubble interface movement direction flips due to peak accelerations occurring here [28]. At a maximum diameter, right as the vapor bubble starts to contract, Rayleigh-Taylor instabilities become most pronounced. At a minimum bubble diameter, Rayleigh-Taylor instabilities form at the highest rate right as the bubble starts to grow due to the less dense bubble vapor pushing the denser host liquid. These instabilities form the most at these parts of the oscillations because right when the bubble interface directions flip, accelerations on the interface are the largest which leads to Rayleigh-Taylor instability generation, accelerations estimated up to 10^4g by Shepherd & Sturtevant [3, 4, 20].

As subsequent oscillations progress, the number of protrusions increase as Rayleigh-Taylor become more dominant, driving the average wavelength down. As ensuing oscillations occur, energy is lost due to thermal, viscous, and acoustic radiation damping, the oscillation amplitude decreases, the interface velocity decreases, and the Rayleigh-Taylor instabilities are reinforced at a diminishing rate [3, 28]. The existing wavelengths converge and the interface starts to smooth, leading to an average increase in wavelength at later oscillations. This increase then decrease in number of instabilities is consistent with the parabolic shaped curves shown in Fig. 3.57 and Fig. 3.58 and number of instabilities and wavelength are roughly inversely related. The wavelength is dependent on the initial droplet diameter, with a larger initial diameter correlating to a larger average wavelength. The wavelength evolution for fixed initial droplet diameter and varying ambient pressure is shown in Fig. 3.59. The plotted curves in this figure are 2nd degree polynomial best fit curves for D_0 = 2 mm at 1 bar and 2 bar ambient pressure. These

curve fits serve simply to group the data and show overall trends. There is no quantified physical basis for these curves fits to be 2nd degree polynomials. This result suggest that the wavelength is dependent on ambient pressure, with an increase in ambient pressure correlating to a decrease in wavelength. This percent decrease from 1 bar to 2 bar for D_0 = 2 mm is shown in Fig. 3.60. The percent decrease is mostly constant throughout the oscillations, varying only a few percent, but the percent decrease is the most at the early oscillations and at the later oscillations, appearing nearly symmetrical.

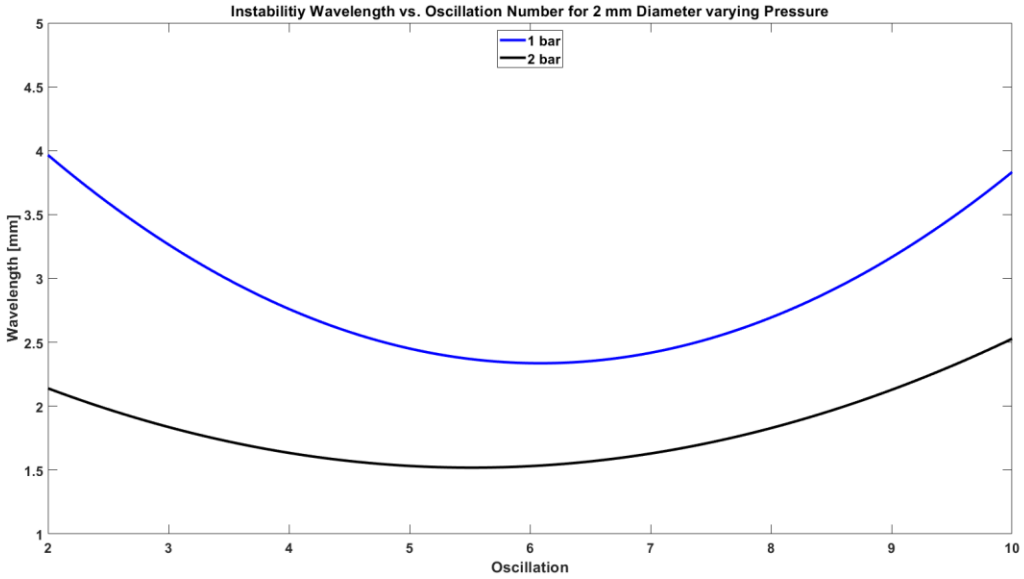

Fig. 3.59 – Wavelength vs. time for D_0 = 2 mm initial droplet size at 1 and 2 bar pressures.

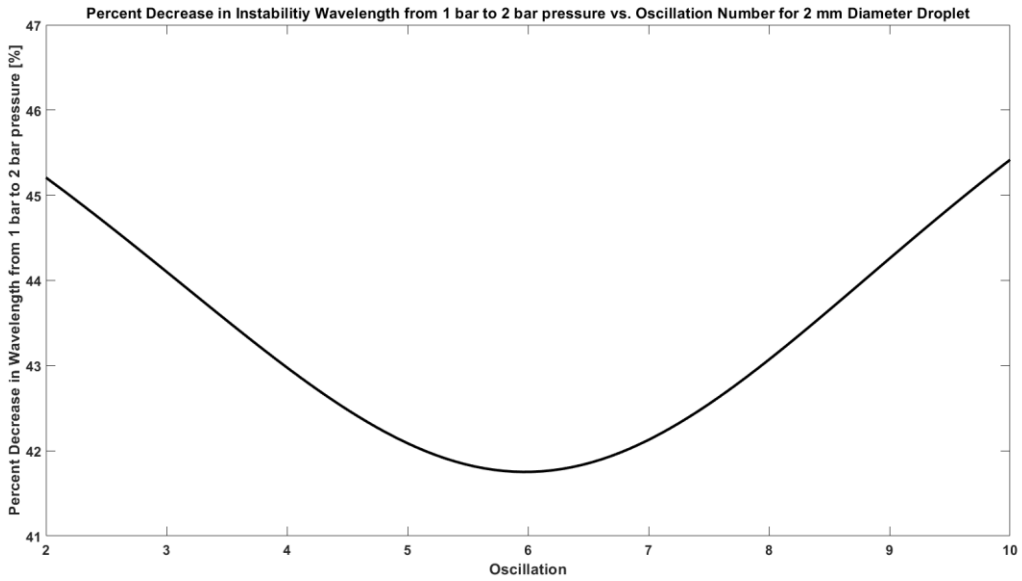

Fig. 3.60 – Percentage decrease in instability wavelength from 1 bar to 2 bar pressure vs. oscillation number for D_0 = 2 mm initial droplet diameter.

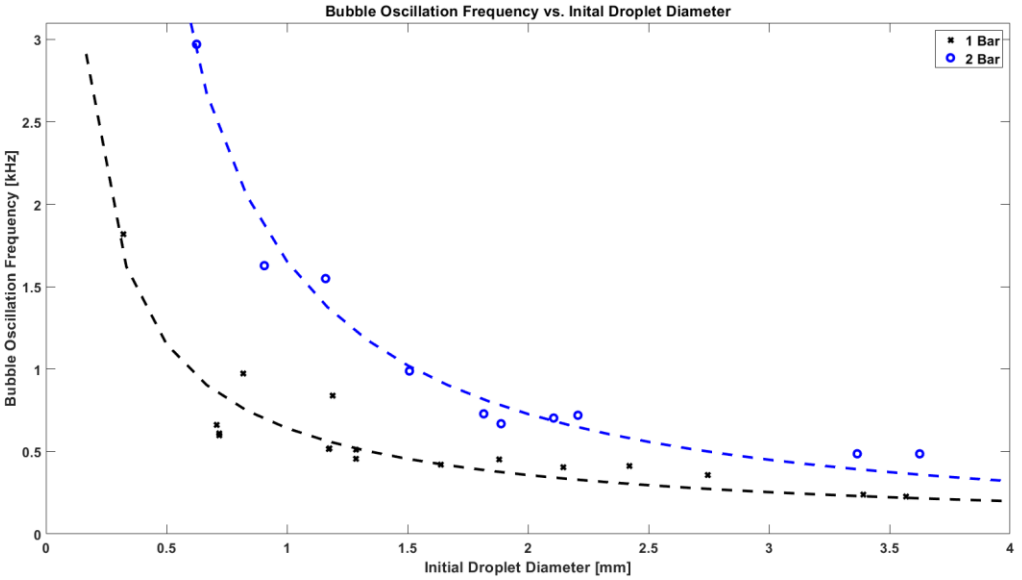

Fig. 3.61 – Bubble oscillation frequency vs. diameter at 1 bar and 2 bar pressure absolute.

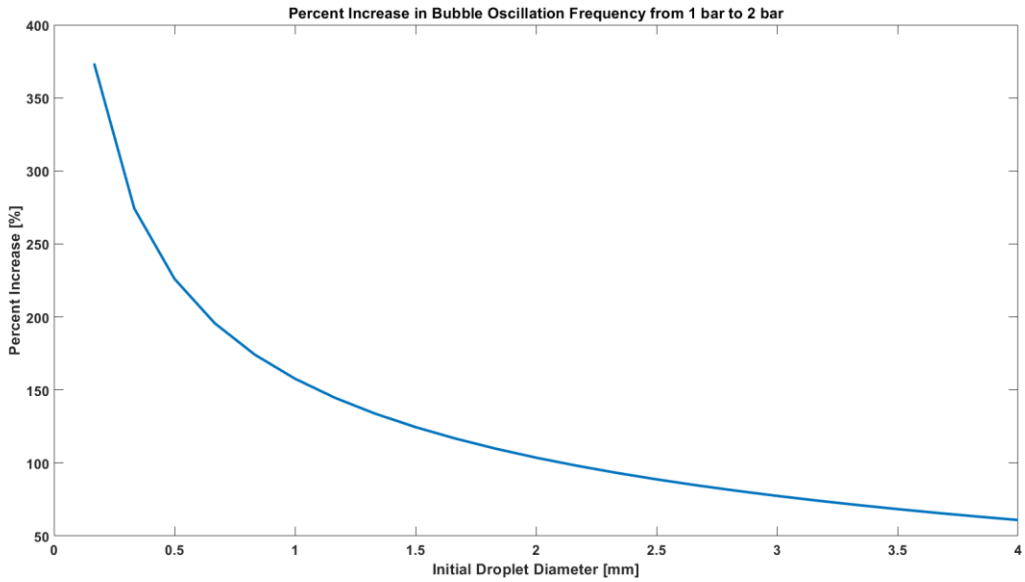

Fig. 3.62 – Percentage increase in bubble oscillation frequency from 1 bar to 2 bar pressure absolute vs. diameter.

After explosive droplet vaporization is complete, the resulting vapor bubble oscillates at a high frequency before dampening out after 8 to 20 oscillation cycles. The bubble oscillation frequency in relation to initial droplet diameter and ambient pressure is shown in Fig. 3.61. The bubble oscillation frequency is accurate to ±0.05 kHz. As the initial droplet diameter increases, the bubble oscillation frequency decreases, causing the oscillations to occur slower. In contrast, as the ambient pressure increases, the oscillation frequency increases, causing the bubble to oscillate more rapidly. Both of these findings, as well as the overall shape of the oscillation frequency curves in Fig. 3.61 are consistent with the following bubble natural frequency equation $\omega = \left\{\frac{3k(P_0 - P_v)}{\rho_l {R_e}^2} + \frac{2(3k-1)S}{\rho_l {R_e}^3} + \frac{8{v_l}^2}{{R_e}^4}\right\}^{\frac{1}{2}}$, where ω is the bubble oscillation frequency, R_e is the bubble equilibrium radius at pressure, analogous to initial droplet diameter, ρ is the density of the host liquid, and P_0 is the ambient pressure in the host liquid [29]. The vapor bubble oscillation frequency can also be found from a simplified version of the previous equation. The bubble oscillation resonance frequency is given by $\omega_r = \sqrt{\frac{3\gamma P_0}{\rho_l R_e^2}}$, where ω_r is the bubble resonance frequency and γ is the ratio of specific heats of vapor [28, 30]. For these bubble oscillation frequency equations, the oscillation frequency scales with the square root of the ambient pressure and the inverse of the bubble radius. Taking initial droplet diameter to be proportional to bubble radius, this trend is consistent with the results shown in Fig. 3.61, with both pressure best fits scaling roughly with the inverse of the initial droplet diameter.

The number of oscillations a vapor bubble undergoes before dampening out appears dependent on both initial droplet diameter and ambient pressure from experimental observation

and is supported by the literature. The behavior of the oscillating vapor bubble is comparable to bubble oscillation behavior during acoustic cavitation, where a bubble grows and collapses under the influence of a driven ultrasound pressure field. Thus the damping effects on an acoustic cavitation bubble can be applied to an oscillating vapor bubble after explosive boiling. As mentioned briefly previously, there are three sources of damping on the oscillating vapor bubble, thermal damping δ_T, viscous damping δ_V, and acoustic radiation damping δ_r. Thus the total damping constant on the oscillating droplet is, $\delta = \delta_T + \delta_V + \delta_r$. Thermal damping is characterized as the conduction in heat from the vapor bubble to the host liquid. The thermal damping constant is quantified as $\delta_T = \frac{3(\gamma-1)}{2\alpha}$, where $\alpha = \frac{R_e}{L_g}$, where L_g is the thermal diffusion length in vapor and is defined as $L_g = \sqrt{\frac{2D_g}{\omega_r}}$, where D_g is the thermal diffusivity in gas and is given by $D_g = \frac{K}{\rho_v C_p}$, where K is the thermal conductivity in gas, ρ is the density of vapor, and C_p is specific heat of gas at constant pressure [28, 31]. Viscous damping is due to the viscous stresses exerted on the liquid by the expanding and contracting vapor bubble. The viscous damping constant is quantified as $\delta_V = \frac{4v_l}{\omega_r R_e^2}$, where v_l is the kinematic viscosity of the host fluid [28, 31]. Acoustic radiation damping occurs because the bubble radiates pressure waves as it oscillates, expending energy. The acoustic radiation damping constant can be quantified as $\delta_r = \frac{\omega_r R_e}{c_l}$, where c is the speed of sound in the host liquid [28, 31]. The typical bubble resonance frequency range, ω_r, encountered here is 0.5 – 3 kHz. Appx. 8 shows the theoretical thermal, viscous, acoustic radiation, and total damping for resonant air bubbles in water vs. bubble resonance frequency [31]. Appx. 9 shows the theoretical thermal, viscous, acoustic radiation, and total damping for resonant air bubbles in water vs. bubble equilibrium radius [29]. While these figures are not representative for diethyl ether vapor bubbles in glycerol, at the resonance frequencies encountered here, 0.5 – 3 kHz, and the equilibrium radii encountered here, 10^{-2} m, thermal and acoustic radiation damping dominate viscous damping. Additionally, at these low frequency ranges, the vapor bubble displays isothermal thermodynamic behavior because the thermal diffusion is so efficient [28].

The percent increase in oscillation frequency from 1 bar to 2 bar ambient pressure vs initial droplet diameter is shown in Fig. 3.62. As the droplet diameter increases the oscillation frequencies for 1 bar and 2 bar converge, suggesting ambient pressure has less of an effect on oscillation frequency at larger droplet diameters – liquid droplet diameters which turn into larger vapor bubble diameters once vaporized.

3.6 Unstable Boiling Far-Field Pressure Measurements

3.6.1 Pressure Plots

A number of representative pressure traces are shown in Figs. 3.63 – 3.65. These illustrate how the far-field pressure varies with time during unstable explosive boiling of a droplet and resulting bubble oscillation behavior. The general shape of the pressure trace resembles a sine wave, with a short ramp up period at the beginning. The pressure trace oscillates with roughly equal positive and negative pressure amplitudes, typically around 1 to 2 psi. As the vapor bubble oscillates, energy is lost to thermal, viscous, and acoustic radiation damping effects and the oscillations slowly diminish in amplitude before stopping [3]. This is reflected in the pressure trace oscillations. As time passes, the peak-to-peak amplitude of the pressure oscillations slowly decreases before finally decaying completely.

Two potential error sources are the irregularities in the pressure trace, visible in both Fig. 3.64 and Fig. 3.65, and the low amplitude first oscillation peak, visible in Fig. 3.65, Fig. 3.67, and Fig. 3.68. The irregularities are characterized as deviations from the smooth curve and a more complicated waveform. Curiously, the irregularities also often appear repetitively, often affecting the same segment of the pressure trace cycle for two or three oscillations in a row, as seen in Fig. 3.64 with the third and fourth pressure maxima and Fig. 3.67 with the second though fifth pressure maxima. It is unclear what causes the low amplitude first oscillation peak, though this same low amplitude first peak has been observed by past research as well [3, 23].

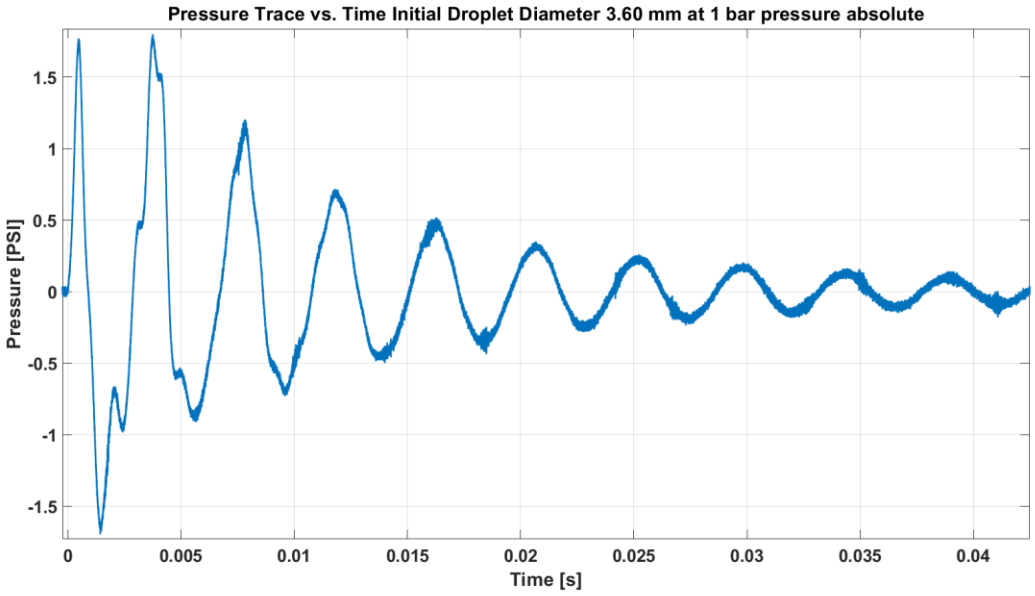

Fig. 3.63 – Selected pressure trace vs. time example. Initial droplet diameter D_0 = 3.60 mm at 1 bar pressure.

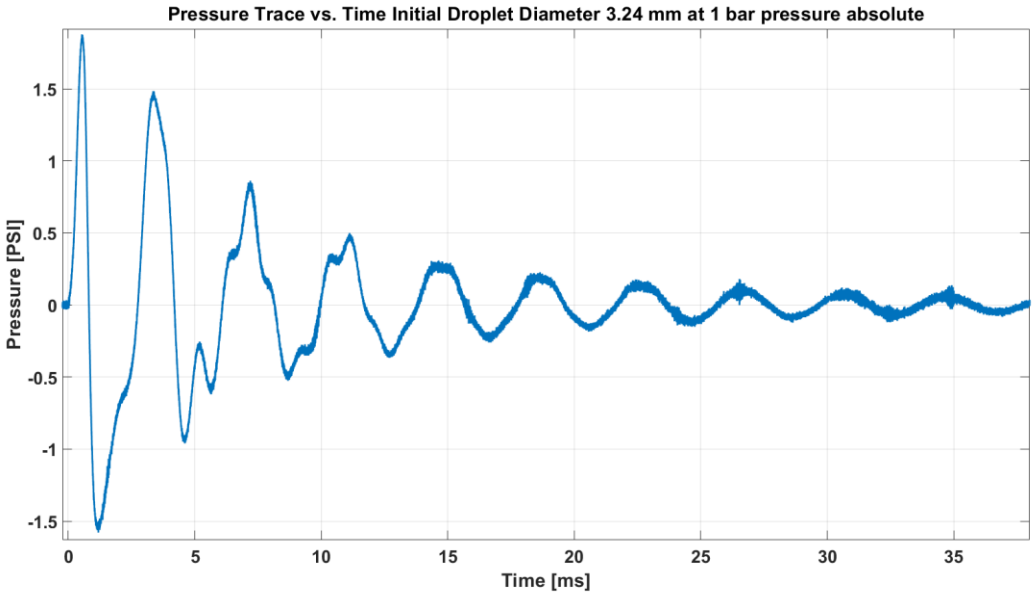

Fig. 3.64 – Selected pressure trace vs. time example. Initial droplet diameter D_0 = 3.24 mm at 1 bar pressure.

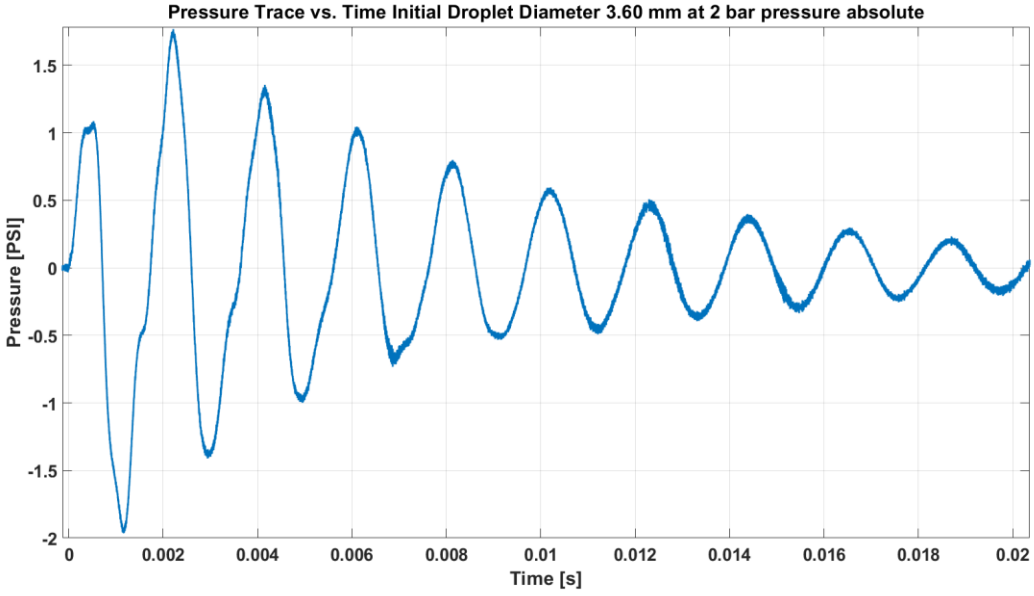

Fig. 3.65 – Selected pressure trace vs. time example. Initial droplet diameter D_0 = 3.60 mm at 2 bar pressure.

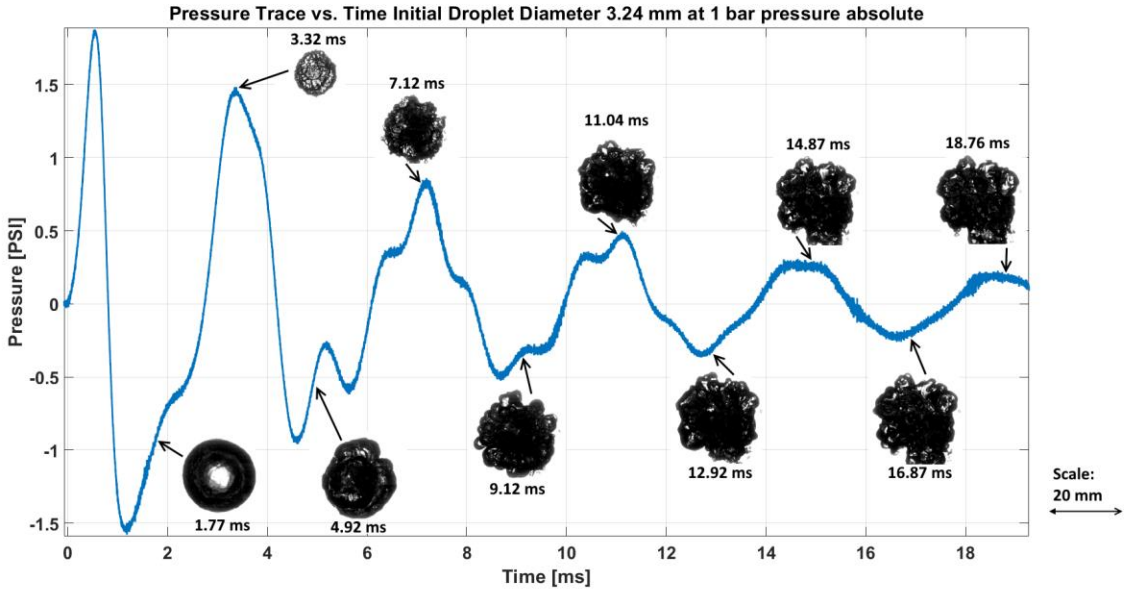

Fig. 3.66 – Pressure trace vs. time for initial droplet diameter D_0 = 3.24 mm at 1 bar ambient pressure with correlating high-speed video stills for maximum and minimum oscillation diameters during first five oscillations. The first bubble image is a maximum, the second is a minimum, then alternating as such, chronologically. Time stamp since initial nucleation each still is taken at listed along with arrow showing location on pressure trace.

Oscillation Number	High-Speed Video, $\Delta t = t_{i+1} - t_i$ [µs]	Pressure Transducer, $\Delta t = t_{i+1} - t_i$ [µs]
1 (Max. Diameter)	0	0
1 (Min. Diameter)	1550	1220
2 (Max. Diameter)	1600	1593
2 (Min. Diameter)	2200	1627
3 (Max. Diameter)	2000	2045
3 (Min. Diameter)	1920	1975
4 (Max. Diameter)	1880	1725
4 (Min. Diameter)	1950	1975
5 (Max. Diameter)	2000	1960
5 (Min. Diameter)	1890	1960
Average:	1888	1787
Average Difference:		**5.5%**

Table 3.1 – High-speed video oscillation period vs. pressure transducer oscillation period for initial droplet diameter D_0 = 3.24 mm at 1 bar ambient pressure, pressure trace with correlating high-speed video stills shown in Fig. 3.66.

The irregularities in the pressure trace may be due to vapor bubble surface disturbances, most notably, Rayleigh-Taylor instabilities. The irregularities appear with much greater incidence

for the case of 1 bar than for 2 bar pressure trials. This is due to higher ambient pressures suppressing vapor bubble interface Rayleigh-Taylor instabilities, demonstrated by the decrease in instability wavelength with an increase in ambient pressure in Fig. 3.59. Since these Rayleigh-Taylor instabilities are repressed to a greater extent at higher pressures, a less noisy pressure trace is typically recorded, especially prominent in Fig. 3.70, Fig. 3.71, and Fig. 3.72. These pressure trace irregularities also occur with greater incidence after the first pressure oscillation maximum, typically first becoming prevalent during or after the first pressure trace minimum which coincides with the first vapor bubble diameter maximum. Typically, this vapor bubble is relatively smooth, but as it starts to contract, Rayleigh-Taylor instabilities begin to form due to the rapid bubble interfacial acceleration from changing direction from growing to contracting.

As demonstrated in Fig. 3.57 and Fig. 3.58, as the vapor bubble oscillation from the second oscillation onward for the next few oscillations, Rayleigh-Taylor instabilities compound and become increasingly prevalent on subsequent oscillations. Over time with increased oscillations beyond half a dozen, the vapor bubble begins to dampen out, slowing down, leading to weaker accelerations on the bubble interface and diminishing Rayleigh-Taylor instabilities and a longer average instability wavelength. This behavior is reflected in the pressure trace trends with the pressure trace irregularities being analogous to the Rayleigh-Taylor instabilities. After the smooth first pressure maxima, irregularities in the pressure trace form and intensify at the same time as Rayleigh-Taylor instabilities on the vapor bubble surface. As Rayleigh-Taylor instabilities start to diminish, so do these irregularities, with the pressure trace becoming stabilized and smoother as the number of oscillations moves past half a dozen. The correlation between the timing of the pressure trace irregularities and the onset of Rayleigh-Taylor instabilities on the vapor bubble interface suggest that these irregularities are a result of the Rayleigh-Taylor instabilities. Additionally, the periodic nature of these irregularities, seen in Fig. 3.64 and Fig. 3.67, suggest the presence of multiple harmonic oscillation frequencies on the surface of the vapor bubble other than the overall vapor bubble oscillation, though quantifying these frequencies has not been attempted. This is supported by cavitation literature, where bubble oscillation behavior is similar, with Neppiras stating that large bubbles above the resonant size, which applies to the bubble diameters in this research, will oscillate in a stable non-linear manner [32].

Another possible source of these pressure trace irregularities is the reflection of pressure waves off of the walls of the test chamber into the pressure transducer. The piezoelectric pressure transducer used to record all pressure trace curves is flush mounted within the side wall of the test chamber where all explosive boiling occurs. The transducer is directly in-line and level with the nominal nucleation point for droplets. The distance the droplet explosion target is from the pressure transducer is 50.8 mm. For glycerol, the host fluid, when heated to the superheat limit temperature of 147˚C, the pressure wave takes 22.8 μs to reach the pressure transducer. The first reflection, off the far wall of the test chamber, reaches the pressure transducer 68.4 μs after nucleation, or in other words, 45.6 μs after the pressure trace has registered and started recording. After these first two waves, subsequent reflections occur every 45.6 μs. From examining the pressure data in Fig. 3.63 – Fig. 3.72, it can be seen that the pressure wave

reflection period, which is on a microsecond scale, is much smaller than the period for the pressure trace irregularities, which are on a millisecond scale. The calculated pressure wave reflections do not show up on the pressure trace data, therefore pressure wave reflections can be determined to not be a notable source of error as well as not a source of the pressure trace irregularities. Another possible source of error is the background noise on the pressure trace plots which is found to have an amplitude less than 0.05 psi mostly, with maximum amplitudes of less than 0.1 psi. Due to the low amplitude of the background noise when compared to the irregularities it can be ruled out at a possible source of error for this phenomenon.

A pressure trace for initial droplet diameter of 3.24 mm at 1 bar ambient pressure with correlating high-speed video stills for maximum and minimum oscillation diameters during the first five bubble oscillations is shown in Fig. 3.66. These high-speed camera stills are taken from the same trial as the pressure trace that is displayed here. The images corresponding to the maximum and minimum bubble diameters are displayed with their corresponding point on the pressure trace curve, for the first five bubble oscillations to directly give a sense of what is physically occurring at these main points of the vapor bubble oscillation. Perhaps counter-intuitively, the maxima of the pressure trace do not correlate with maxima diameters of the vapor bubble oscillations nor do the minima correspond with the respective minima. Instead, roughly the opposite is the case, with the maxima of the pressure trace corresponding roughly to the minima of the vapor bubble oscillation diameter and the minima of the pressure trace corresponding roughly to the maxima of the vapor bubble oscillation dimeter. The only exception occurring at the first pressure trace maximum, which appears to correspond roughly to the completion of the liquid droplet vaporization. This trend was seen by Frost as well [4, 21]. The difference in time between a maxima and the following minima or a minima and the following maxima is called the half period. This applies for either vapor bubble oscillation diameters or pressure trace maximums and minimums. The half period is shown for the first five cycles for Fig. 3.66 for both the vapor bubble oscillation and the resulting pressure trace in Table 3.1. These half periods are averaged and the average difference between the two is found to be 5.5%, confirming that these two forms of measurement are in agreement and accurate representations of each other. A degree of observational error can be assumed due to the pressure trace not being completely regular as well as the time at which the vapor bubble reaches maximum or minimum being somewhat undefined, leading to a small about of human judgement. For example, the visual difference between 4.92 ms and 4.93 ms for the second maximum vapor bubble diameter in Fig. 3.66 is extremely small. The 5.5% error can be attributed to this observational error. An extended version of Table 3.1 with raw high-speed video times and raw pressure transducer times can be found in Appx. 5.

Pressure traces for fixed initial diameter and varying ambient pressure are shown in Fig. 3.67 – Fig. 3.69 and Fig. 3.70 – Fig. 3.72, where the first two figures show the pressure traces individually and last overlaps them for better comparison. The frequency of the bubble oscillations is dependent on ambient pressure, with the frequency increasing with an increase in pressure. When moving from 1 bar ambient pressure to 2 bar ambient pressure for an initial

droplet diameter of D_0 = 3.60 mm, the frequency appears to increase by approximately 60%. This pressure trace data estimate is congruent with visually measured bubble oscillation frequency changes with pressure reported earlier in Fig. 3.61 and Fig. 3.62 and with analytical formulation presented above. Additionally, the number of irregularities that occur appear to be correlated positively to pressure, as demonstrated by Fig. 3.70 – Fig. 3.72 and discussed earlier. There does not appear to be a strong correlation between number of pressure oscillations and pressure. Furthermore, the pressure trace amplitude does appear to be correlated to ambient pressure, with an increase in pressure associating with a decrease in pressure trace amplitude, as seen in Fig. 3.69 and Fig. 3.72. Intuitively, this makes sense because higher pressure corresponds to lower interface boiling velocity, making a less violent explosion and a lower resulting overpressure.

The relationship between pressure trace amplitude and pressure, as well as the relationship between initial droplet diameter and pressure trace amplitude are examined in more detail in Fig. 3.73. For Fig. 3.73, the largest pressure amplitude, either maximum or minimum, from each pressure trace is plotted against the initial droplet diameter of that trial. Linear regression lines are plotted on Fig. 3.73 for the 1 bar and 2 bar data sets as well. From these linear regression lines, it is clear that there is a higher pressure amplitude for 1 bar than for 2 bar pressure. In addition, maximum pressure appears to increase linearly with an increase in initial droplet diameter. For 1 bar, a coefficient of correlation of 0.93 and a coefficient of determination of 0.87 were found. For 2 bar, a coefficient of correlation of 0.95 and a coefficient of determination of 0.90 were found. These values suggest a strong positive linear correlation between initial droplet diameter and maximum pressure amplitude. This intuitively makes sense since larger droplets release more energy when vaporized. Lastly, when increasing ambient pressure from 1 bar to 2 bar absolute, the percentage decrease in maximum pressure amplitude is dependent on the initial droplet diameter, with larger droplets having a greater drop in maximum pressure amplitude, as shown in Fig. 3.74.

There is one caveat regarding the pressure trace amplitudes. The amplitude of the pressure trace is determined heavily by the distance the pressure transducer is located from the droplet vaporization. The pressure transducer in this experiment is located 50.8 mm away from the location of the droplet explosion and receives a far field pressure. Compared to past research, this distance from the droplet explosion to the pressure transducer is on the longer end. As a result, the maximum pressure amplitudes reported here, 1 – 2 psi, are on the lower end of the spectrum. While past researchers mostly tested other test fluids than diethyl ether, so a direct comparison is more difficult to make, rough pressure can be compared. Shepherd and Sturtevant, using liquid butane as a test fluid with a pressure transducer located 25 mm away, found peak pressure amplitudes of about 4.8 psi [3]. McCann, also examining butane with a pressure transducer distance of between 2 and 10 mm, a found initial peak pressure amplitude of around 10 psi [22]. Frost, using diethyl ether for a test fluid and a pressure transducer distance of 4 – 9 mm, observed a first peak pressure amplitude of 11.6 psi [4, 21]. Lastly, Park examined cyclohexane as well as a 60% hexane 40% benzene mixture at a far-field pressure transducer distance of around 50 mm and found both to peak in pressure amplitude between 4 psi and 6.5

psi [23]. These pressure amplitudes are mostly comparable to the amplitudes reported here when the distance from the droplet vaporization to the pressure transducer is taken into account.

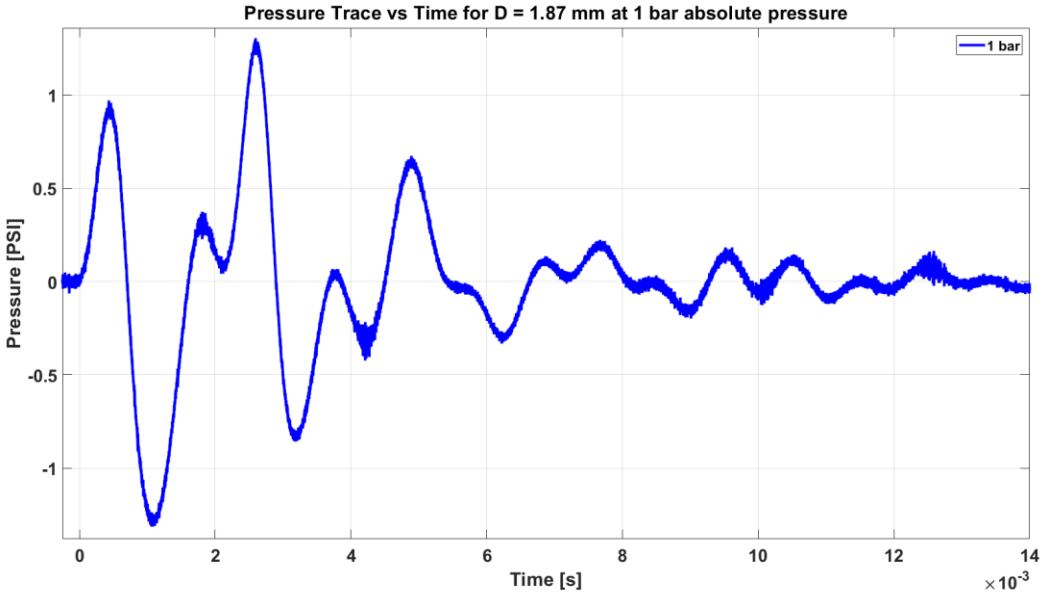

Fig. 3.67 – Pressure trace vs. time. Initial droplet diameter D_0 = 1.87 mm at 1 bar pressure.

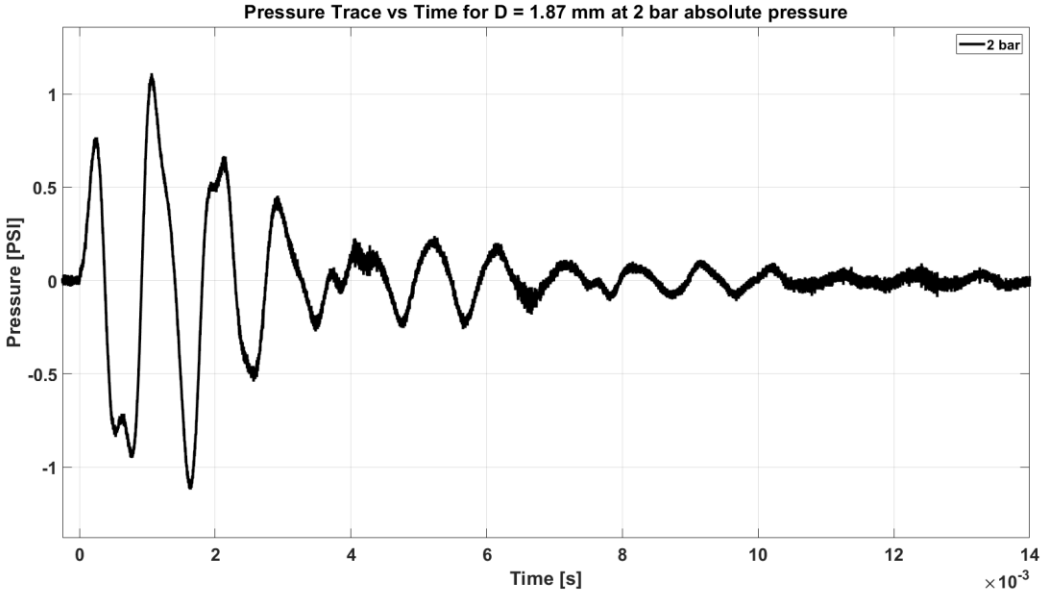

Fig. 3.68 – Pressure trace vs. time. Initial droplet diameter D_0 = 1.87 mm at 2 bar pressure.

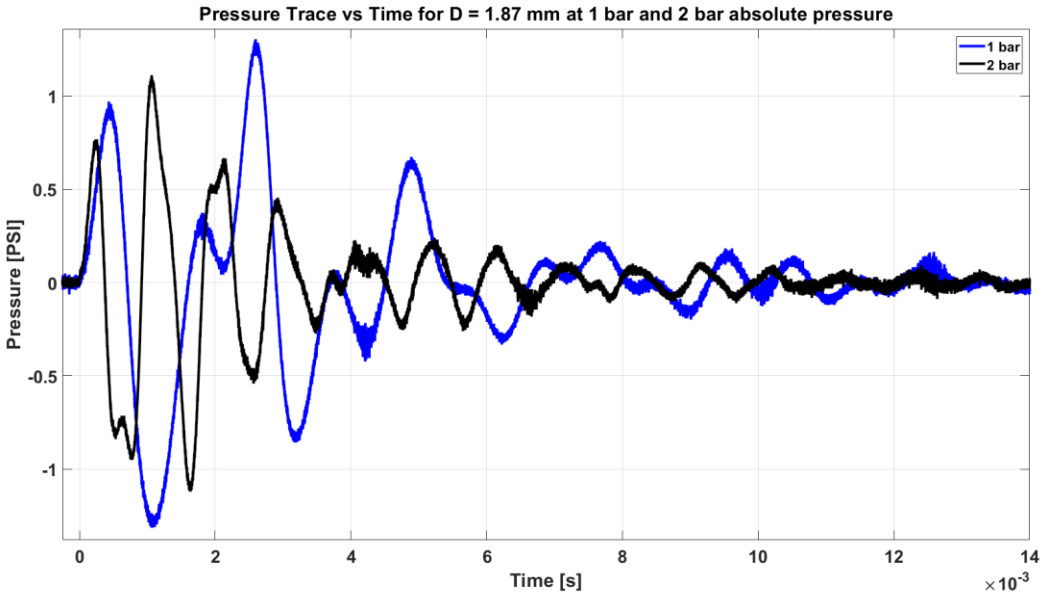

Fig. 3.69 – Pressure trace vs. time. Initial droplet diameter D_0 = 1.87 mm at 1 bar and 2 bar pressures.

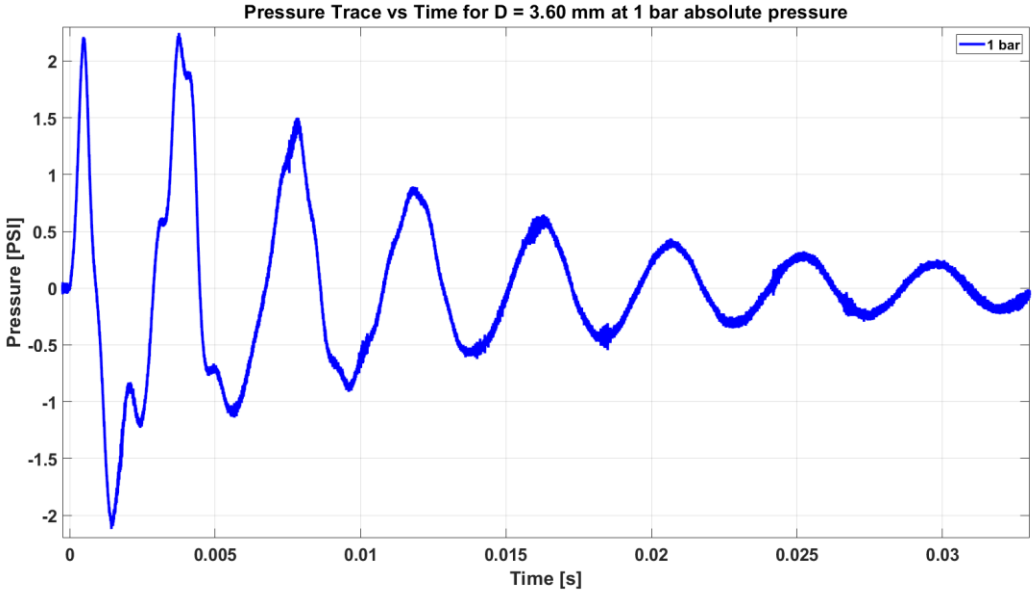

Fig. 3.70 – Pressure trace vs. time. Initial droplet diameter D_0 = 3.60 mm at 1 bar pressure.

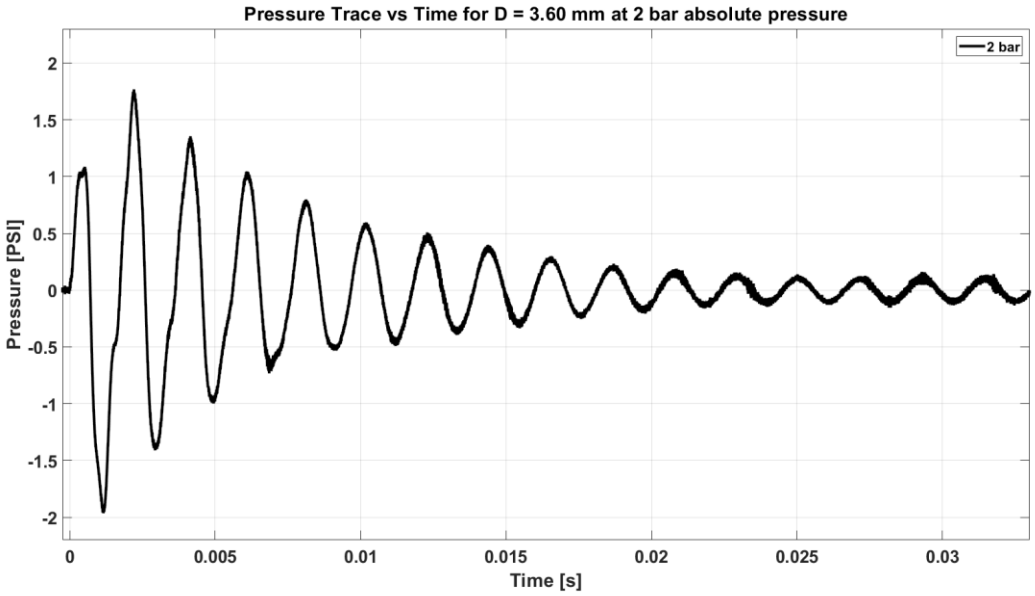

Fig. 3.71 – Pressure trace vs. time. Initial droplet diameter D_0 = 3.60 mm at 2 bar pressure.

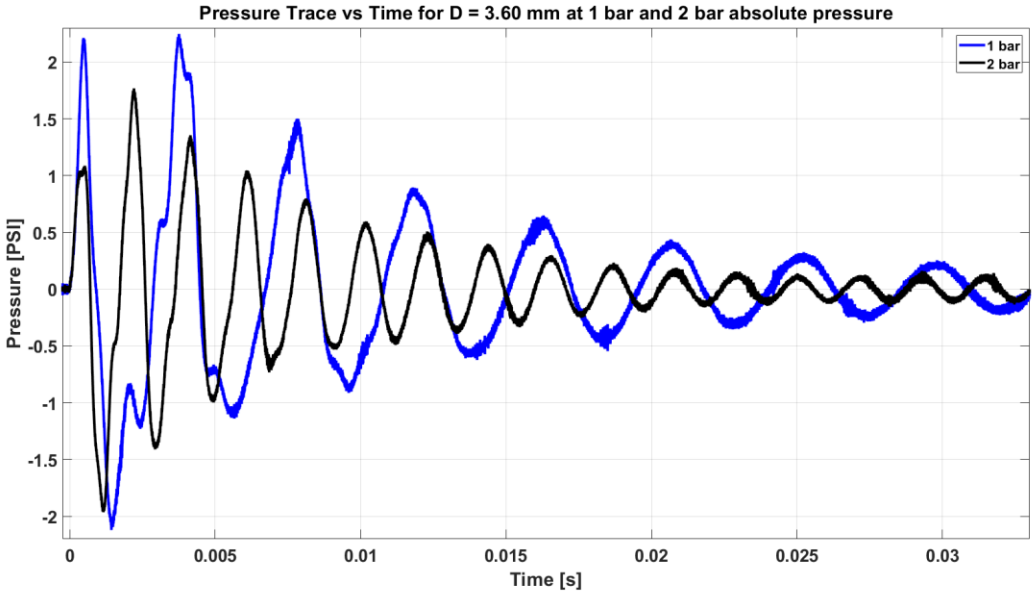

Fig. 3.72 – Pressure trace vs. time. Initial droplet diameter D_0 = 3.60 mm at 1 bar and 2 bar pressures.

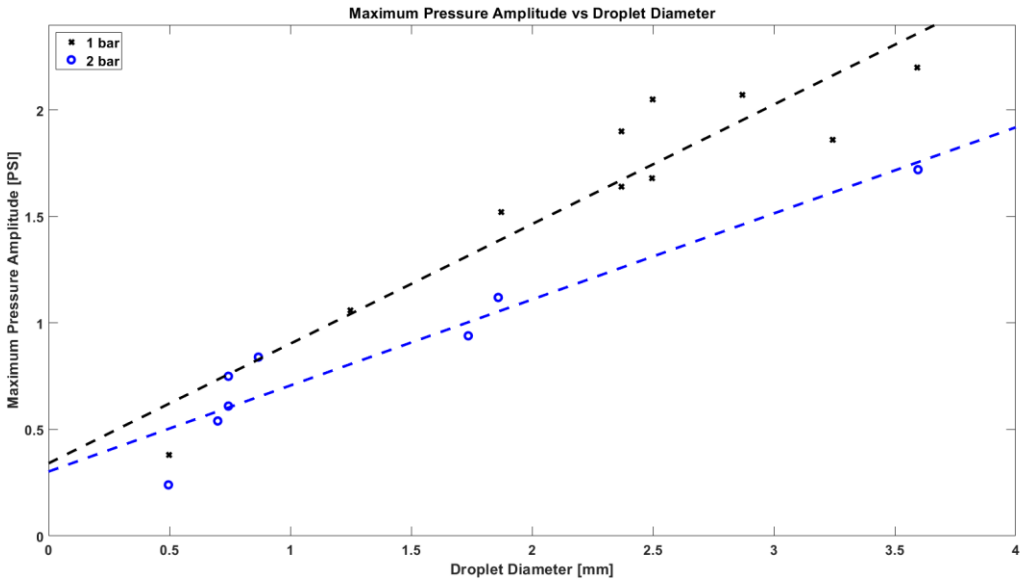

Fig. 3.73 – Maximum pressure (amplitude) vs. diameter at 1 bar and 2 bar pressure with linear regression lines.

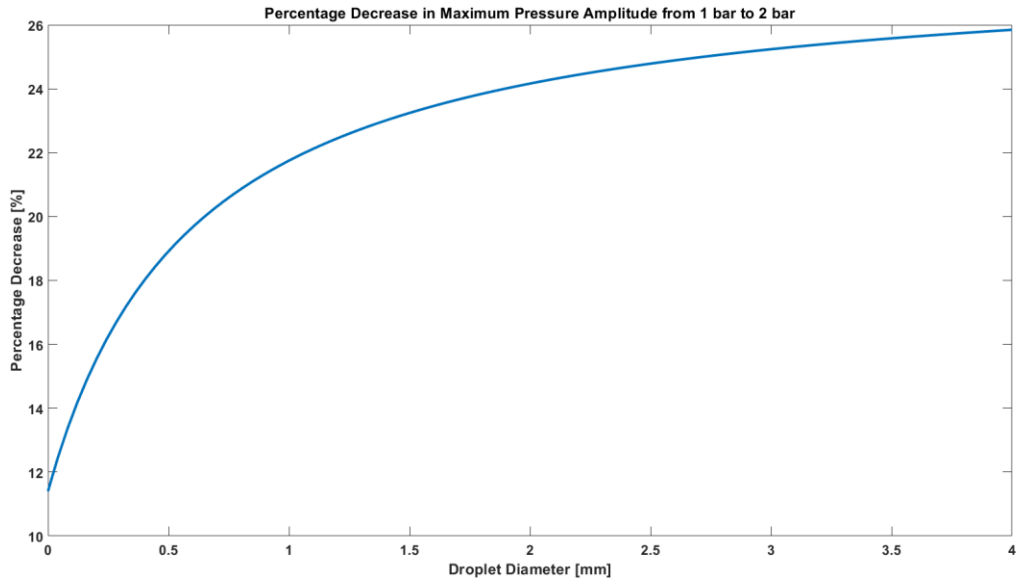

Fig. 3.74 – Percentage decrease in maximum pressure (amplitude) when increasing the ambient pressure from 1 bar to 2 bar vs. droplet diameter.

3.6.2 Jakob Number

The Jakob number is a dimensionless number that represents the ratio of sensible heat during vaporization to the latent heat required during vaporization. At saturated conditions, the Jakob number is defined as $a = \frac{C_p(T_{sat})(T_{SL}-T_{sat})}{L(T_{sat})}$, where $C_p(T_{sat})$ is the specific heat at the saturation point, T_{SL} is the temperature at the superheat limit, and $L(T_{sat})$ is the latent heat of vaporization at the saturation point [4]. The Jakob number is a measure of the thermal energy available during vaporization. A larger Jakob number means there is more energy available during boiling and correlates to a more violent vaporization process [4]. As ambient pressure is increased, the saturation temperature, T_{sat}, increases while the superheat limit temperature, T_{SL}, remains largely unchanged for the pressures considered in this work. As a result, as pressure increases, the Jakob number decreases, with both the changes in the specific heat and latent heat term being dominated by the change in the temperature difference. How the Jakob number changes for diethyl ether as ambient pressure is varied is shown in Table 3.2 and Fig. 3.75.

With an increase in ambient pressure, the average overpressure and the average interface velocity decrease. These decreases with increased pressure may result not only from the smaller difference between the superheat limit and the saturation temperature and as a result less energy available for vaporization, quantified by the Jakob number, but also from the unique Darrieus-Landau-like interface instabilities causing two-phase mass flux. First, considering the overall pressure range measured, 1 bar to 5 bar, the Jakob number decreases nearly linearly across this whole range. However, looking at how the average interface velocity changes over this range in Fig. 3.39 and Fig. 3.42, it can be clearly seen that the interface velocity does not decrease roughly linearly over this pressure range, but rather disjointedly when changing from unstable to stable boiling regimes. This suggests that the decreased energy available for vaporization at elevated pressures due to the increased saturation point is not the only driving factor behind a decreased interface velocity at elevated pressures. Looking specifically at the increase in ambient pressure from 1 bar to 2 bar absolute, the Jakob number decreases from 0.705 to 0.640, a percentage decrease of 9%. Examining Fig. 3.25 and Fig. 3.30, it can be seen that the average interface velocity from 1 bar to 2 bar decreases from around 20 m/s to around 14 m/s, a percentage decrease of about 30%, suggesting that the decreased specific heat available for vaporization is not the sole factor for this interface velocity drop. Additionally, examining the average overpressure decrease from 1 bar to 2 bar in Fig. 3.74, the percentage decrease over the 0.5 mm to 3.5 mm droplet diameter range is around 23%, much larger than the 9% percentage decrease in the Jakob number. This reinforces the suggestion that the decrease in the sensible heat available during vaporization as ambient pressure increases is not the only factor responsible for the decrease in overpressure and interface velocity as pressure increases, suggesting that is this decrease in vaporization violence is also due to a decrease in the Darrieus-Landau-like instability.

Ambient Pressure Absolute (bar)	Jakob Number
1.0	0.705
2.0	0.640
3.0	0.590
4.0	0.545
5.0	0.505

Table 3.2 – Jakob number for diethyl ether vs ambient pressure.

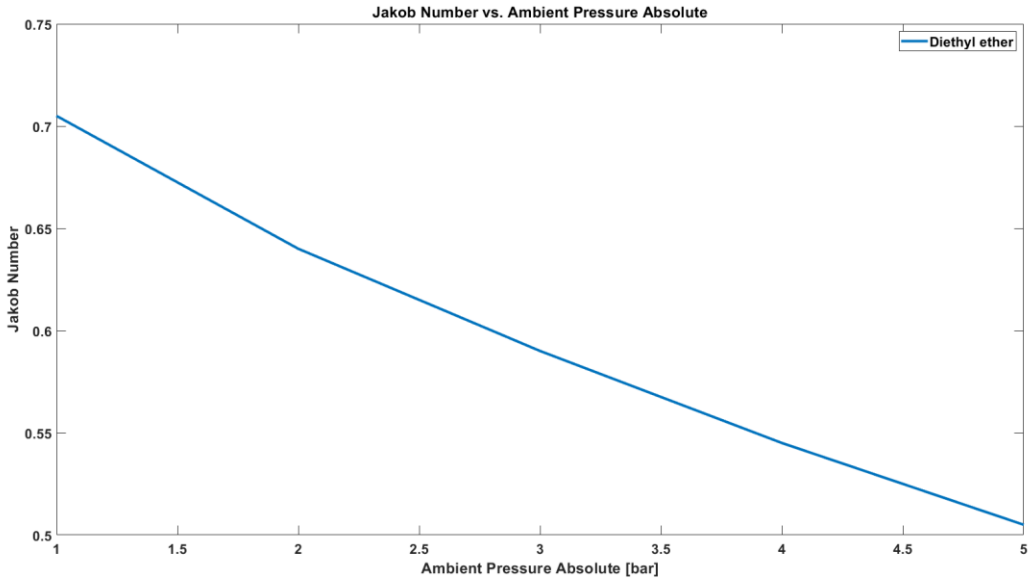

Fig. 3.75 –Jakob number for diethyl ether vs ambient pressure absolute.

4.0 Conclusions

Immersed diethyl ether droplets, sized 0.5 to 3.5 mm in diameter, undergoing homogeneous nucleation, both unstable and stable, at the superheat limit, 147˚C, are examined experimentally. Ambient pressure and initial droplet diameter are studied to understand their influence on diameter and volumetric growth rate, vapor bubble interface and evaporation velocities, vapor bubble mass flux and mass flow rates, unstable boiling vapor bubble Rayleigh-Taylor wavelengths and oscillation frequency, and pressure data oscillation frequency and amplitude.

It is observed that vapor bubble growth during unstable nucleation is linear with constant interface velocity and mass flux rate. It is also shown that vapor bubble growth during stable nucleation vaporization appears roughly logarithmic with an interface velocity and mass flux that exponentially decays. For the case of unstable nucleation, the normalized diameter growth forms an S-shaped curve. However, for stable nucleation, the normalized diameter growth appears mostly linear. It is found that increasing ambient pressure decreases growth rate, interface velocity, and mass flux rate.

Conversely, increasing initial droplet diameter is shown not to have an impact on the vapor bubble growth rate, interface velocity, or mass flux rate. But, it is found that when normalized by initial droplet diameter, smaller initial diameter droplets grow to larger vapor bubble diameters than larger initial diameter droplets. It is seen that an increased ambient pressure correlates to a decreased Rayleigh-Taylor instability wavelength, a decreased overpressure amplitude, and an increased oscillation frequency. In comparison, an increase in initial droplet diameter has been shown to increase Rayleigh-Taylor instability wavelength, increase overpressure amplitude, and decrease vapor bubble oscillation frequency. The impetus of this research is to build on previous research, using present day technology, to better understand unstable and stable homogenous boiling. The principal objective in the present work is to film in detail unstable and stable homogeneous vaporization completely, from superheated liquid droplet before incipient nucleation, to initial vapor bubble formation, to the full evaporation of the liquid droplet by the vapor bubble, to vapor bubble oscillations, to buoyant effects becoming dominant. This goal was successful. Analysis and image processing of homogeneous boiling film yielded new correlations and further validated old ones.

Looking to the future, there are a few avenues and improvements that would be fascinating to pursue. The first, would be to improve spatial resolution of the high-speed videos. Filming the *full* explosive boiling event was successful with a minor caveat, the spatial resolution was sufficient to examine everything desired except the unstable surface instability. The hope here was to be able to quantify the unstable boiling interface behavior and instability length scale with a wavelength. While the temporal resolution at 10 μs was excellent, the spatial resolution – averaging 0.125 mm/pixel at a resolution of 256 x 256 pixels, excellent for all other measurements – unfortunately was not sufficient for this task. To improve the spatial resolution,

two routes may be pursued, either get a higher resolution camera or a better lens. The latter is the more feasible option if someone were to talk up this work at a new thesis from where I left off in the near future. Having high-speed film with better spatial resolution would allow a more detailed view of the unstable explosive boiling interface during nucleation. This would allow a better understanding of this phenomenon, believed to be the primary driving force behind the extremely rapid vaporization rate in explosive boiling.

To quantify the wavelengths on the unstable interface or how rapidly the interface perturbations form would be invaluable to understanding unstable nucleation as a whole by cutting right to the underlying cause. Alternative ways of attaining better spatial resolution would be to use a stronger backlighting source in conjunction with a light diffuser that approximates a Lambertian light source, like opal glass. This type of diffuser distributes light equally in all directions, ideally placed as close as possible to the exploding droplet, potentially inside the test chamber itself. The diffuser would minimize the refraction of both the spherical droplet and vapor bubble edges, and most importantly, the backlight refraction of the unstable interface instability, leading to better imaging.

Another solution would be to develop two separate testing criteria. Since the high-speed camera can trade temporal resolution for spatial resolution as explained before, a higher pixel resolution may be selected in exchange for a lower frame rate. Two testing criteria can be developed, one similar to the one presented before, chosen to maximize both temporal and spatial resolutions for filming the full nucleation process, and another emphasizing spatial resolution over temporal, giving, perhaps, double the pixel resolution at half the frame rate. At this higher spatial resolution, the temporal resolution would be 20 μs, sufficient to track the movement of the unstable interface, while also providing enough spatial resolution to measure the interface wavelengths. Additionally, by increasing the spatial resolution, computational image processing become more relevant. Plus, as resolution increases, measurement error decreases, leading to more accurate results. Combined with a computational image processing algorithm, also decreasing error as less assumptions are made, error will decrease and result accuracy will improve. Relating to computation image processing, another interesting avenue to pursue would be to examine both the visual oscillation data and the pressure data to try and qualify definitely the irregularities in the pressure trace with Rayleigh-Taylor instabilities on the oscillating bubble surface. In addition to this, examining these pressure trance irregularities and the Rayleigh-Taylor instabilities for possible frequencies other than the overall vapor bubble oscillation would be fascinating.

5.0 References

1. Abraham, F. (1974). *Homogeneous nucleation theory; the pretransition theory of vapor condensation* (Advances in theoretical chemistry. Supplement; 1). New York: Academic Press.
2. Baidakov, V. G., (2007). *Explosive boiling of superheated cryogenic liquids*. Wiley-VCH.
3. Shepherd, J. E. and Sturtevant, B., "Rapid evaporation at the superheat limit," *J. Fluid Mech.* **121**, 379-402, 1982.
4. Frost, D. L., "Effects of ambient pressure on the instability of a liquid boiling explosively at the superheat limit," California Institute of Technology, May 22, 1985.
5. Landau, L. D., "On the theory of slow combustion," *Acta Physiochimica, U.R.S.S.*, **19**, p. 77, 1944.
6. Berthoud, G. (2000). "Vapor Explosions." *Annual Review of Fluid Mechanics*, **32**(1), 573-611.
7. Rice, Doyle, "At least 23 injured as 'lava bomb' hits tour boat near Hawaii's Kilauea volcano," *USA Today*, July 17, 2018.
8. Chang, Reid, and Fay. (1983). "Boiling and spreading of liquid nitrogen and liquid methane on water." *International Communications in Heat and Mass Transfer*, **10**(3), 253-263.
9. Li, Peterson, and Cheng. (2008). "Dynamic characteristics of transient boiling on a square platinum microheater under millisecond pulsed heating." *International Journal of Heat and Mass Transfer*, **51**(1), 273-282.
10. Glod, Poulikakos, Zhao, and Yadigaroglu. (2002). "An investigation of microscale explosive vaporization of water on an ultrathin Pt wire." *International Journal of Heat and Mass Transfer*, **45**(2), 367-379.
11. Lin, L. P., and Pisano, A. (1994). "Thermal bubble powered microactuators." *Microsystem Technologies*, **1**(1), 51-58.
12. Prosperetti, A., and Plesset, M.S., "Vapour-bubble growth in a superheated liquid," *J. Fluid Mech.* Vol. **85** (2), 349-368, 1978.
13. Blander, M., and Katz, J. (1975). "Bubble nucleation in liquids." *AIChE Journal*, **21**(5), 833-848.
14. Kwak, H., and Lee, S., (1991). "Homogeneous bubble nucleation predicted by a molecular interaction model." *Journal of Heat Transfer*, Series C), **113**(3), 714-721.
15. Kwak, Oh, & Park. (1995). "Bubble dynamics on the evolving bubble formed from the droplet at the superheat limit." *International Journal of Heat and Mass Transfer*, **38**(9), 1709-1718.
16. Nguyen, V. T., Furzeland, R. M., and Ijpelaar, M. J. M., "Rapid evaporation at the superheat limit," *Int. J. Heat Mass Transfer* **31**, 1687, 1988.
17. Dergarabedian, P. (1960). "Observations on bubble growths in various superheated liquids." *Journal of Fluid Mechanics*, **9**(1), 39-48.

18. Kosky, P. (1968). “Bubble growth measurements in uniformly superheated liquids.” *Chemical Engineering Science*, **23**(7), 695-706.
19. Abdelmessih, Hooper, & Nangia. (1972). “Flow effects on bubble growth and collapse in surface boiling.” *International Journal of Heat and Mass Transfer*, **15**(1), 115,IN3,119-118,IN4,125.
20. Sturtevant, B. and Shepherd, J. E., “Evaporative instability at the superheat limit,” *Applied Scientific Research* **38**, 85-97, 1982.
21. Frost, D.L., “Dynamics of explosive boiling of a droplet,” *Phys. Fluids* **31** (9), 2554-2561, 1988.
22. McCann, H., Clarke, L.J., and Masters, A.P., “An experimental study of vapour growth at the superheat limit temperature,” *Int. J. Heat Mass Transfer* **32** No. 6, 1077-1093, 1989.
23. Park, H.-C., Byun, K.-T., and Kwak, H.-Y., “Explosive boiling of liquid droplets at their superheat limits,” *Chemical Engineering Science* **60**, 190-1821, 2005.
24. Yaws, C. (1999). *Chemical properties handbook: Physical, thermodynamic, environmental, transport, safety, and health related properties for organic and inorganic chemicals* (McGraw-Hill handbooks). New York: McGraw-Hill.
25. Skripov, V. (1973). *Metastable liquids*. New York: J. Wiley.
26. Reid, R. (1976). “Superheated liquids.” *American Scientist*, **64**(2), 146-156.
27. Reid, Robert C. (1978). “Superheated Liquids a Laboratory Curiosity and, Possibly, an Industrial Curse. Part 2: Industrial Vapor Explosions.” *Chemical Engineering Education*, 108-11.
28. Young, F. (1999). *Cavitation*. London: Imperial College Press.
29. Brennen, Christopher E., *An internet book on fluid dynamics*, 2006. Retrieved from http://brennen.caltech.edu/fluidbook/multiphase/Bubblegrowthandcollapse/bubblenaturalfrequencies.pdf
30. Minnaert, M. (1933). XVI. “On musical air-bubbles and the sounds of running water.” *The London, Edinburgh, and Dublin Philosophical Magazine and Journal of Science*, **16**(104), 235-248.
31. Devin, C. (1959). “Survey of Thermal, Radiation, and Viscous Damping of Pulsating Air Bubbles in Water.” *The Journal of the Acoustical Society of America*, **31**(12), 1654-1667.
32. Neppiras, E. (1980). “Acoustic cavitation.” *Physics Reports*, **61**(3), 159-251.

6.0 Appendix

6.1 Stable-to-Unstable Boiling

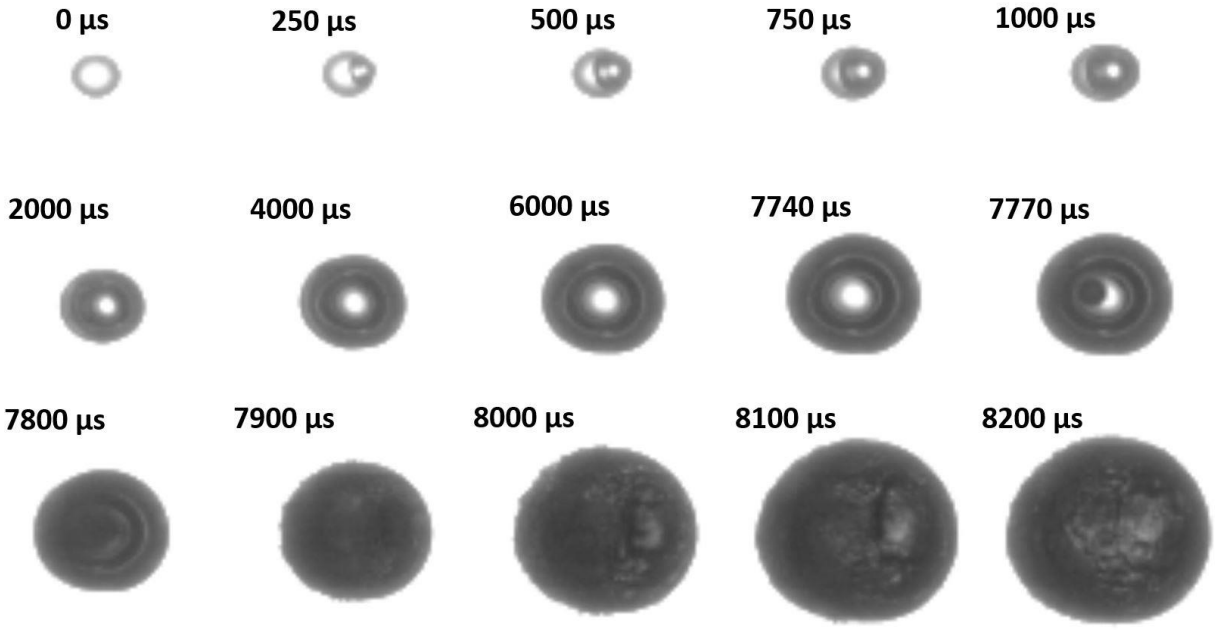

Appx. 1 – "Transition" stable-to-unstable explosive boiling in a diethyl ether droplet of diameter, D_0 = 1.75 mm, immersed in glycerol at 3 bar pressure. Initial nucleation is stable until explosive nucleation occurs 7740 µs later, quickly overwhelming the stable boiling process and rapidly vaporizing the droplet. The presence of interface instabilities are clearly apparent here. The stable boiling bubble is translucent in the middle, but is opaque on the outside due to the curvature of the bubble refracting the backlight. However, 30 µs after unstable nucleation begins, at 7770 µs, the unstable bubble is already opaque from the interface instabilities refracting the backlight.

While unstable homogenous boiling occurs at 1 bar to 2 bar absolute ambient pressure and stable boiling occurs at 3 bar to 5 bar absolute ambient pressure, occasionally "transition" stable-to-unstable boiling occurs between 2 bar and 4 bar absolute ambient pressure. This mode of homogenous boiling is observed to occur most commonly at 3 bar absolute ambient pressure, less commonly at 2 bar and 4 bar, and never at 1 bar and 5 bar. This stable-to-unstable homogenous boiling is shown in a high-speed video stills progression in Appx. 1. Stable-to-unstable boiling can be roughly characterized as stable homogenous boiling which has the occurrence of a second nucleation point leading to unstable boiling that rapidly consumes the droplet and results in vapor bubble oscillations. From this progression, it can be seen that two separate nucleation points occur. The first nucleation point results in stable boiling, which appears to vaporize the majority of the droplet. In the displayed trial this stable boiling lasts for 7740 µs. After 7740 µs, a new nucleation point occurs which results in unstable boiling which quickly propagates throughout the liquid droplet and vapor bubble. During this unstable process,

the surface becomes visibly disturbed and opaque, leading to the belief of the presence of an instability similar the Darrieus-Landau instability [3, 4, 5].

The behavior of stable-to-unstable boiling resembles concatenated stable and unstable boiling. The stable part of stable-to-unstable boiling resembles stable boiling in trends observed, and the unstable part resembles unstable boiling in trends observed. The normalized diameter vs time for stable-to-unstable boiling is shown in Appx. 2. The normalized diameter is calculated in the same way it was calculated for Fig. 3.9, Fig. 3.11, Fig. 3.16, and Fig. 3.17. The normalized diameter grows relatively slowly in the first, stable segment, before the onset of unstable boing at which point the normalized diameter grows rapidly before slowing to a halt at maximum diameter. The amount of time after the start of stable boiling for the onset of the unstable boiling is inexact. As stated before, the occurrence of a nucleation point is a probability measure, so there is a certain degree of randomness to when exactly the second nucleation point will occur. There appears to no correlation between the time after the stable nucleation point the unstable nucleation point occurs and ambient pressure or initial droplet diameter. Similar to previously observed trends, increasing the ambient pressure decreases the normalized diameter and normalized diameter growth rate. Additionally, increasing the initial droplet diameter decreases the normalized diameter and normalized diameter growth rate, with the one exception being 1.83 mm initial diameter droplet at 3 bar pressure. For this case, the unstable boiling onset occurs relatively quickly after stable nucleation. Since unstable boiling occurs quickly after, stable boiling has not vaporized much of the liquid droplet, leading to a large amount of liquid to be vaporized unstably. Due to a larger portion of liquid being vaporized unstably, the boiling process is more violent and the resulting vapor bubble grows to a larger diameter than if a smaller portion of the liquid droplet was boiled unstably.

The interface velocity of the vapor bubble vs time is shown in Appx. 3. There is an initial rise, peak, and fall in the interface velocity for the stable boiling, followed by a much larger rise, peak, and fall in the interface velocity for unstable boiling before finally reaching zero velocity at the vapor bubble diameter maximum. Interface velocity is measured here similarly to how it is measured in Fig. 3.25, Fig. 3.30, Fig. 3.34, and Fig. 3.35, except upon the onset of the second nucleation point, the fixed origin point velocity is measured from is shifted to this point. Similar to previous interface velocity trends, there appears to be a correlation between interface velocity and ambient pressure with an increase in ambient pressure resulting in a decrease in interface velocity. Additionally, there does not appear to be a correlation between interface velocity and initial droplet diameter. As explained before, the 1.83 mm initial diameter droplet at 3 bar pressure has a larger portion of liquid droplet being vaporized unstably, resulting in a more violent boiling process and a higher interface velocity.

After vaporization is complete, the vapor bubble, having been violently vaporized, oscillates and Rayleigh-Taylor instabilities form on the vapor bubble interface, as explained previously. These Rayleigh-Taylor instabilities are quantified by an average wavelength. The Rayleigh-Taylor wavelength vs oscillation number is shown in Appx. 4 for stable-to-unstable

boiling. These wavelengths are measured in the same way the wavelengths are measured in Fig. 3.57 and Fig. 3.58. Similar trends are shown in these stable-to-unstable trial as in the unstable trials shown before. As ambient pressure is increased average wavelength decreases. Additionally, as initial droplet diameter is increased, average wavelength is increased.

It is unsurprising that these stable-to-unstable trials reflect the same trends seen in previous stable and unstable trials, as the individual phenomena are unchanged, but simply linked together by occurring successively in the same droplet.

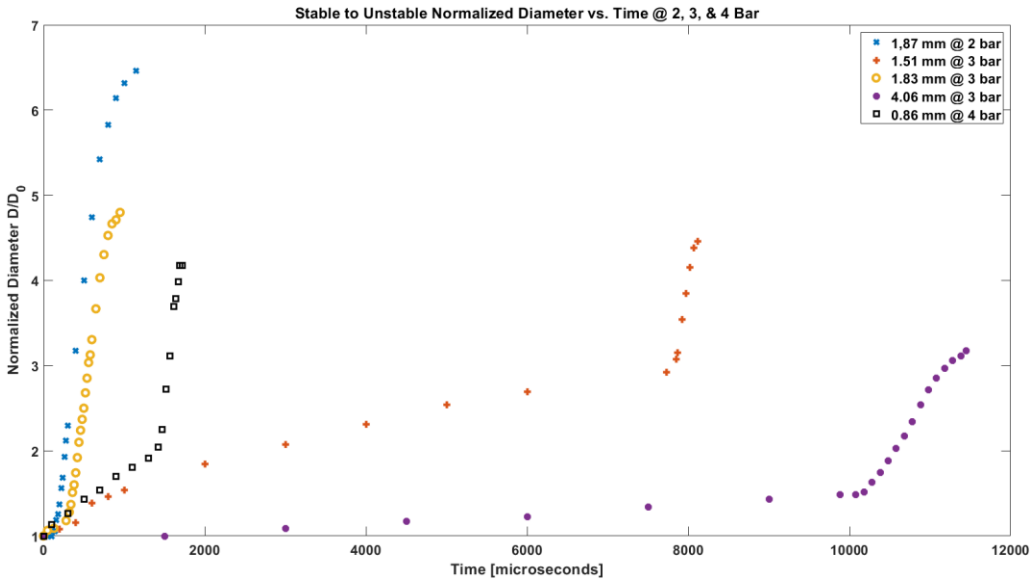

Appx. 2 – Normalized droplet and subsequent bubble diameter vs. time at 2, 3, and 4 bar pressure for stable-to-unstable explosive boiling.

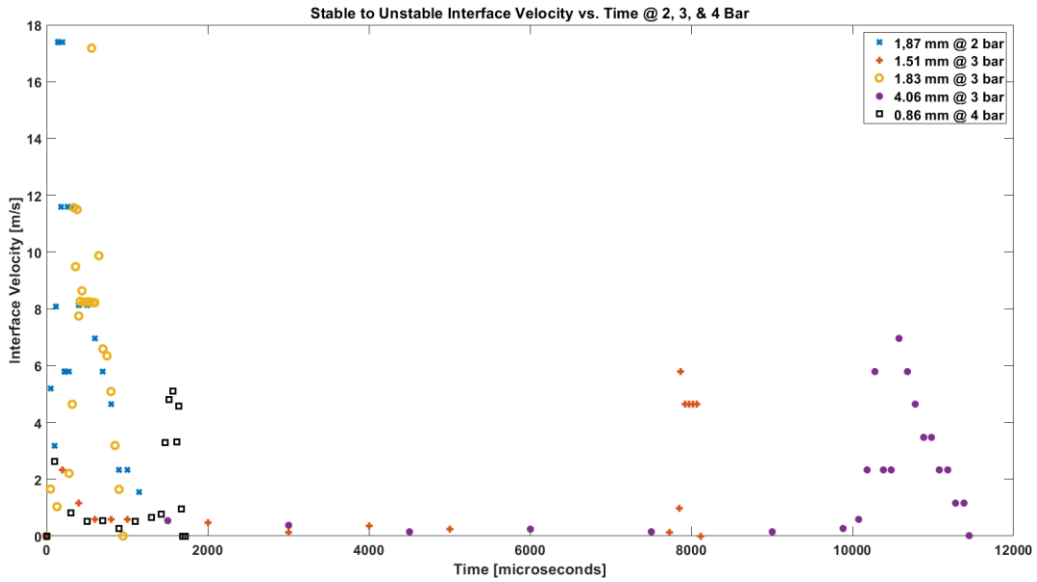

Appx. 3 – Interface velocity vs. time at 2, 3, and 4 bar pressure for stable-to-unstable explosive boiling.

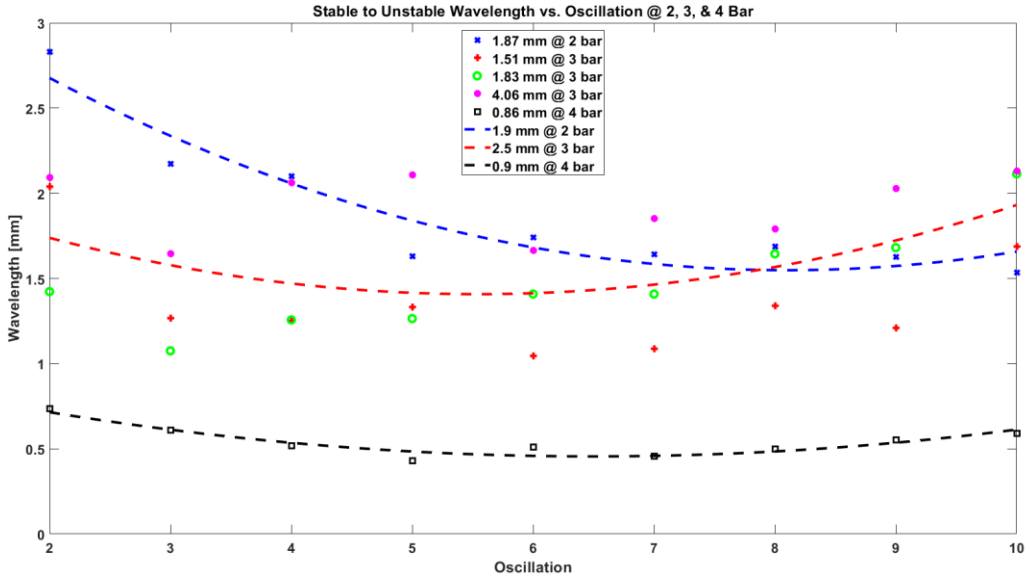

Appx. 4 – Wavelength vs. time at 2, 3, and 4 bar pressure for stable-to-unstable explosive boiling. Empirical curve fits for droplets with initial diameter $D_0 \approx$ 1.9 mm at 2 bar, 2.5 mm at 3 bar, and 0.9 mm at 4 bar shown.

5.2 Miscellaneous

Oscillation Number	High-Speed Video Time [μs]	$\Delta t = t_{i+1} - t_i$ [μs]	Pressure Transducer Time [s]	$\Delta t = t_{i+1} - t_i$ [μs]
1 (Max. Diameter)	1770	0	1.40864	0
1 (Min. Diameter)	3320	1550	1.40986	1220
2 (Max. Diameter)	4920	1600	1.411453	1593
2 (Min. Diameter)	7120	2200	1.41308	1627
3 (Max. Diameter)	9120	2000	1.415125	2045
3 (Min. Diameter)	11040	1920	1.4171	1975
4 (Max. Diameter)	12920	1880	1.418825	1725
4 (Min. Diameter)	14870	1950	1.4208	1975
5 (Max. Diameter)	16870	2000	1.42276	1960
5 (Min. Diameter)	18760	1890	1.42472	1960
	Average:	1888 μs	Average:	1787 μs
			Percent Difference:	**5.5%**

Appx. 5 – Full table of high-speed video oscillation period vs. pressure transducer oscillation period for initial droplet diameter D_0 = 3.24 mm at 1 bar ambient pressure, pressure trace with correlating high-speed video stills shown in Fig. 3.66.

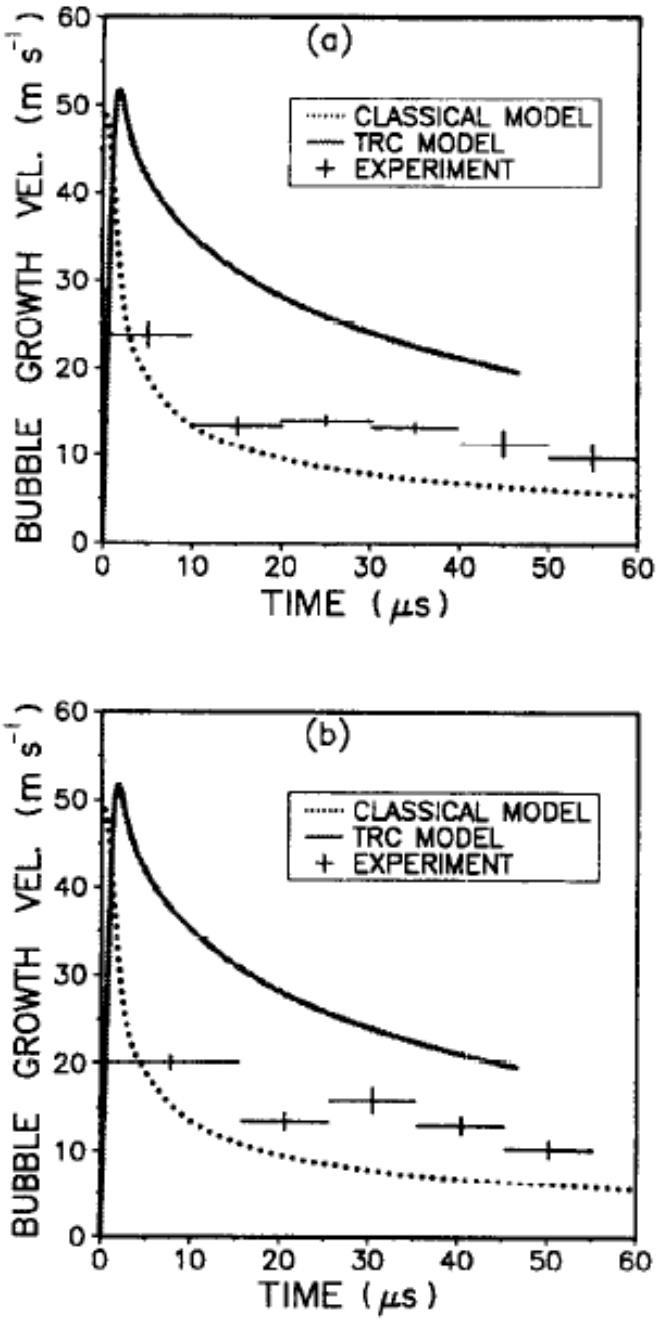

Appx. 6 – McCann reported vapor bubble growth velocities with the Prosperetti and Plesset "classical model" and the Thornton Research Centre (TRC) model by Nguyen [22].

Appx. 7 – A video repository has been set up on YouTube to host a select number of unstable and stable boiling videos. The videos are located on the YouTube channel "UWAA Explosive Boiling" or can be found via a YouTube search of the channel title.

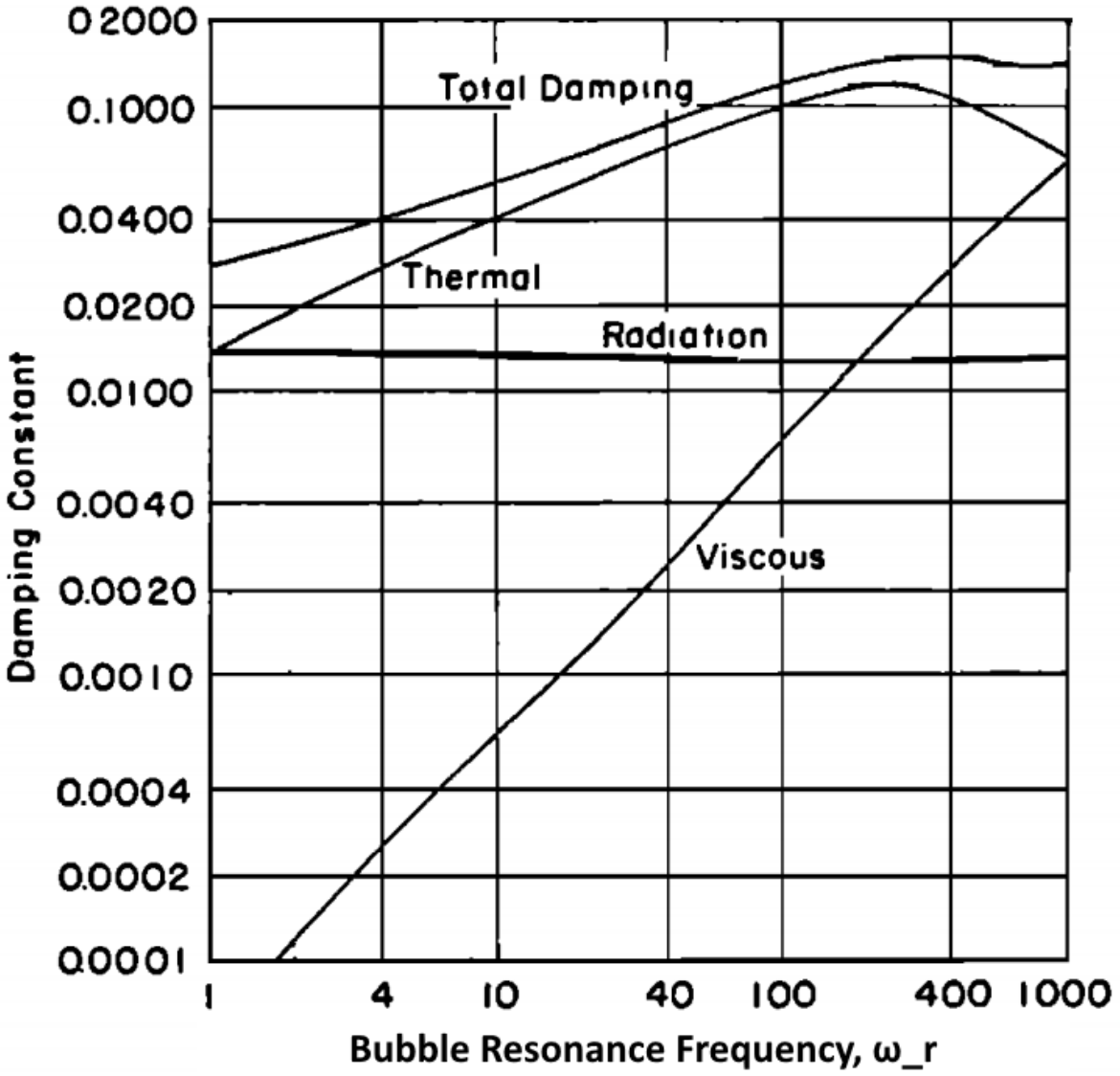

Appx. 8 – Theoretical thermal, viscous, acoustic radiation, and total damping constants for resonant air bubbles in water vs. bubble resonance frequency [31].

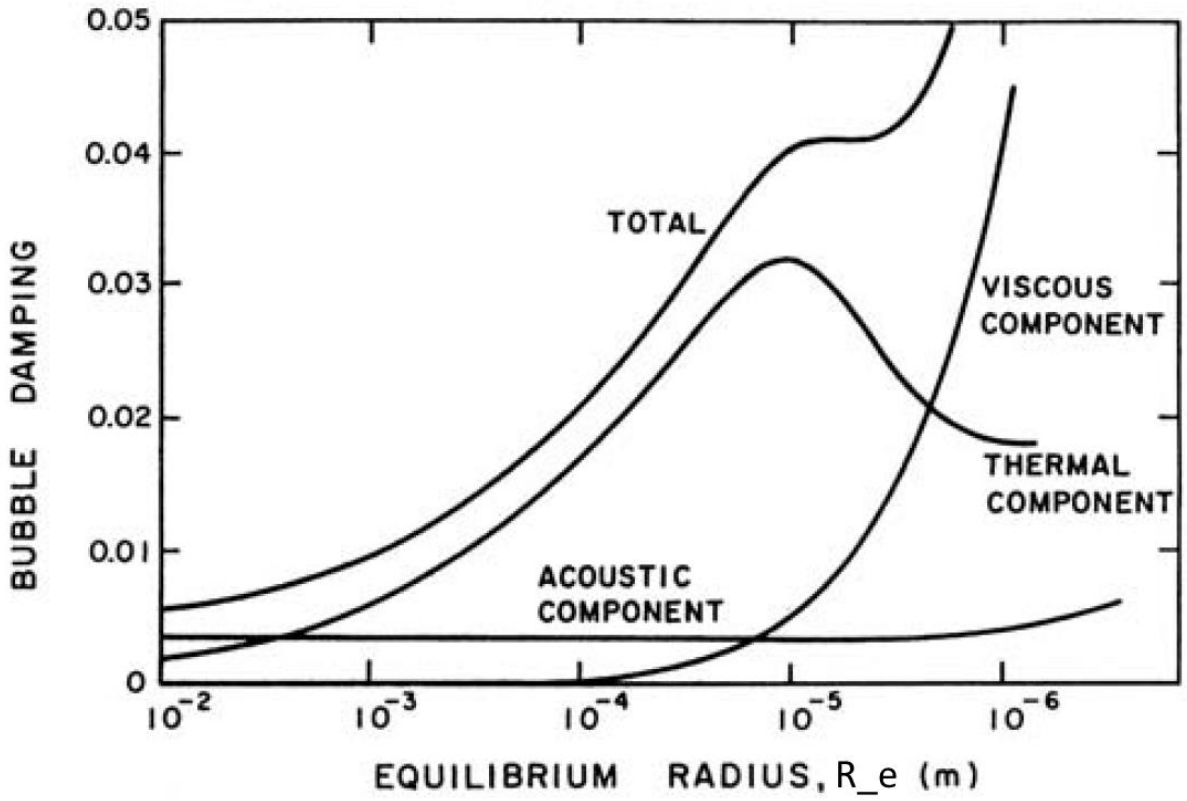

Appx. 9 – Theoretical thermal, viscous, acoustic radiation, and total damping constants for resonant air bubbles in water vs. bubble equilibrium radius [29].

Appx. 10 – Experimental Procedure, List Form

- Turn on ventilation hood, open lab door
- Confirm high-speed camera is setup with tripod, light cannon set up on tripod
- Turn on laptop, open PCC camera control application, turn on camera, and turn on light cannon
- Put on PPE: safety glasses and gloves
- Focus camera on 2 mm scale inside of test chamber. Ensure camera is at 128 x 128 resolution, 100,000 fps, and 10 µs exposure time. Take a 'Length Scale' video
- Flush out droplet injector with water
- Load droplet injector with diethyl ether
- Camera should already be focused from 'Length Scale' video so the water stream should be in focus as it rises though center of test section
- Turn off camera and light cannon
- Confirm top plate piping exhaust is open
- Turn on chiller pump, confirm set point is at 22˚C

- Turn on PID temperature controller, confirm input thermocouple is the top one, confirm set point is set to 156˚C, ensuring target explosion location is at 147˚C
- Let droplet column warm up to approximately 120˚C, should take about 1.5 hours
- Once droplet column is partially heated, vent high pressure nitrogen gas through droplet column, 30 seconds to 1 minute
- Dial nitrogen gas regulator to zero. Once regulator is at atmospheric pressure, close top plate piping vent and wait for droplet column to heat to testing conditions so that the target explosion location is at 147˚C
- Now that the droplet column is heated, it will be at an elevated pressure due to thermal expansion. If testing at atmospheric pressure, vent droplet column using the top plate piping exhaust. Repeat as needed until at set temperature then vent for last time before sealing.
- If testing at elevated pressure let droplet column reach set temperature. Then pressurize to desired pressure minus 10 psi. The addition of room temperature nitrogen gas will drop the temperature of the droplet column. As the droplet column warms again to the set temperature, the pressure will creep up as well. Wait for temperature to reach set point again and pressurize to desired pressure. If done correctly, the pressure will almost be the desired pressure and temperature should drop only minimally.
- Once at desired temperature and pressure, turn back on the camera and light cannon
- Turn on LEDs at base of droplet column
- Turn on pressure transducer signal amplifier
- Connect to the pressure transducer data acquisition unit (DAQ) via remote desktop, confirm it is set to 1.25 MHz and 3 second acquisition duration
- Confirm with digital temperature display hooked up to middle thermocouple probe that temperature is at the limit of superheat (remember due to offset TC reads 1˚C cooler, so 146˚C is target)
- Start recording with camera
- Inject 1-2 mm diameter diethyl ether droplets with glass syringe, using the scale mounted on the droplet injector to inject accurately
- When the droplet floats up to within view of the viewports hit record on the DAQ LabVIEW control (pre-trigger system)
- After the droplet explosively boils, hit the trigger on PCC application (post-trigger)
- Save video on hard drive, save DAQ pressure trace on hard drive under similar naming convention
- Repeat last four steps, capturing more trials until out of temperature range
- Wait until back in temperature range and continue testing
- Do not inject more than 0.5 mL during one testing day
- Upon completion, shut down power to temperature controller, shut down camera, shut down light cannon, shut down droplet injector LEDs, shut down pressure transducer signal amplifier.

- Let droplet column cool off for 30 minutes
- If at elevated pressure, ensure nitrogen compressed gas cylinder is closed
- Vent droplet column via the top plate exhaust, ensure PPE was not removed prior to this
- Turn off chiller pump
- Remove PPE
- Turn off ventilation hood, close lab door